Nanosecond Structural Dynamics of Ferroelectric Oxide Thin Films

by

Pice Chen

A dissertation in partial fulfillment of the requirements

for the degree of

Doctor of Philosophy

(Materials Science)

at the

University of Wisconsin-Madison

2013

Date of final oral examination: 10/25/13

The dissertation is approved by the following members of the Final Oral Committee:
Paul Evans, Professor, Materials Science and Engineering
Chang-Beom Eom, Professor, Materials Science and Engineering
Thomas Kuech, Professor, Chemical and Biological Engineering
Dane Morgan, Associate Professor, Materials Science and Engineering
Mark Rzchowski, Professor, Physics

Abstract

The functionalities of ferroelectric materials are closely related to the switchable spontaneous polarization and the polarization-structure coupling. A persistent effort has been made since the discovery of ferroelectricity to understand and manipulate the electronic and structural properties of ferroelectrics. Recently, studies of ferroelectrics have been focused on novel materials, including ferroelectric/dielectric superlattices and multiferroics that provide additional means to modify the functional properties. This thesis provides an in-depth study of the coupling of the polarization with other degrees of freedom, based on experimental measurements of the structural changes induced by electric fields and optical excitation.

We have studied the mechanism associated with the transformation from a nanoscale polarization domain state to uniform polarization in ferroelectric/dielectric $PbTiO_3/SrTiO_3$ superlattices. The switching process was probed using time-resolved x-ray microdiffraction, which allowed us to follow the domain dynamics at their characteristic nanosecond timescale. $PbTiO_3/SrTiO_3$ superlattices exhibit a weakly coupling between the polarizations of the component layers, and, as a result, the competition between the energy associated with the depolarization field and the energy of domain walls leads to the formation of stripe domains. The dielectric layers have a smaller polarization than the ferroelectric layers. The formation of stripe domains and the unequal distribution of the polarization have important consequences in the response of the superlattice to applied electric fields. We found that the switching of the stripe domains occurs heterogeneously at the submicron scale, with a timescale for switching

that depends on the magnitude of the applied electric field. Each component layer responds differently to applied electric fields. The dielectric $SrTiO_3$ layers are initially less polarized and thus exhibit a large distortion of domains before the transformation is complete. A significant piezoelectric expansion of the $SrTiO_3$ layers is found after the transformation to the uniform polarization state, which is consistent with the change in polarization due to the elimination of stripe domains.

The second component of this thesis focuses on the structural response of epitaxial multiferroic $BiFeO_3$ thin films to high electric fields and femtosecond laser excitation. We have found that the piezoelectricity of a $BiFeO_3$ thin film deviates from its low-field linear response in electric fields higher than 150 MV/m. The increase of the piezoelectricity as well as a simultaneously observed increase in the diffuse scattering is consistent with the softening of the lattice in the proximity of an electric-field-induced phase transition. The sub-nanosecond structural dynamics of $BiFeO_3$ thin films were also probed with time-resolved x-ray scattering following above-bandgap femtosecond laser excitation. A photoinduced strain on the order of 0.5% develops within 100 ps after a lase pulse with a 3.1 eV photon energy and a transmitted fluence of 6 mJ/cm^2. Two potential mechanisms are discussed for this expansion: a piezoelectric response to the screening of the depolarization field in the presence of photoinduced carriers, and a mechanical response to the large induced population of excited carriers. The relaxation of the strain can be interpreted as a carrier recombination process, which is on the order of one nanosecond depending on the film thickness. The widths of Bragg reflections increase under large laser fluence, an effect that can be attributed to strain inhomogeneity.

Acknowledgement

To begin with, I would like to gratefully thank my advisor Prof. Paul Evans. His passion for science has constantly inspired me to solve scientific and technological challenges by learning the associated fundamental aspects. I am fortunate to have his advice and encouragement throughout my PhD program.

My PhD projects cannot be successful without the hard work of our collaborators. Prof. Chang-Beom Eom, Prof. Matthew Dawber and Prof. Darrel Schlom have provided both essential samples and invaluable input. Beamline scientists Dr. Eric Dufresne and Dr. Osami Sakata are most resourceful and have delivered excellent synchrotron diffraction setup. Collaboration with Dr. Haidan Wen and Dr. Yuelin Li has been very productive in terms of both scientific outputs and technical development.

I would also like to thank all the group members. Prof Ji Young Jo, a former postdoc in our group, and Dr. Rebecca Sichel-Tissot have helped teach me the essential experimental skills. Together with Margaret Cosgriff and Dr. Qingteng Zhang, they are my strong allies to fight through the obstacles during countless experiment weeks at synchrotron facilities and to finish my projects with a strong ending.

PhD program is long, particularly for a foreigner including me studying aboard at the opposite side of the earth. My parents have been most considerate and supported me for no reason. My best time in my personal life is to meet my wife, Fengyuan Shi, here in Madison. The unconditional support from my family is the reason that a seemingly stressful five years can be full of wonderful memories.

Table of Contents

1 Introduction

The emergence of novel ferroelectrics promises to provide new ways to modify the electric polarization, crystallographic symmetry and local structural distortion of electronic materials. The fundamental interplay between different degrees of freedom gives rise to a range of new phenomena, including nanoscale polarization domain patterns [1], improper ferroelectricity [2], field-induced phase transitions [3] and bulk photovoltaic effects [4]. A large number of studies have focused on the properties under steady-state conditions or near equilibrium with relatively small external perturbations. The dynamics of ferroelectrics in large applied fields or with large concentrations of excited charge carriers, however, are much less well known. Theoretical calculations in the far-from-equilibrium regime provide predictions of dynamical phenomena in polarization domain switching [5] and ultrafast structural modifications [6]. This thesis describes studies of the structural dynamics of ferroelectric/dielectric superlattices and multiferroics at sub-nanosecond to nanosecond timescales based on time-resolved x-ray microdiffraction.

Superlattices consisting of alternating ferroelectric and dielectric layers exhibit ferroelectric properties that are distinct from the bulk forms of their chemical components. In these superlattices, the spontaneous polarization of the ferroelectric layer extends into the dielectric layers, with a magnitude that depends on the strength of the coupling between the component layers [7]. In the weakly-coupled regime, the polarization in the dielectric layers is smaller than in the ferroelectric layers [8]. In this case, the polarization self-organizes into nanoscale stripe domain to minimize the total

electrostatic energy. Understanding the dynamics of these nanoscale domains is the key to understanding the complex interplay of electronic and structural properties at the interfaces within the superlattice. Chapters 3 and 4 describe the mechanism through which an applied electric field causes these weakly coupled superlattices to transform to a uniform polarization state and also discuss the role of the unequal distribution of polarization between layers during the transformation [9, 10].

Multiferroics exhibit both ferroelectric polarization and spin ordering. Bismuth ferrite, $BiFeO_3$, is a prototype multiferroic, with ferroelectric electrical polarization and antiferromagnetic magnetic order at room temperature. It is critically important to understand the crystallographic structure of $BiFeO_3$ in response to external stimuli, in order to achieve an eventual control of multiferroicity. Chapter 5 discusses an enhancement of the piezoelectric coefficient in epitaxial $BiFeO_3$ thin film in large electric fields [11]. Chapter 6 shows that a large strain can be induced by femtosecond laser pulses and that this strain subsequently relaxes on a nanosecond timescale [12].

Chapter 1 begins with an introduction of the basic concepts of ferroelectric materials: polarization hysteresis, the relationship between atomic structure and ferroelectric polarization, the formation of polarization domains, and piezoelectricity. A brief overview of two classes of novel ferroelectric materials, ferroelectric/dielectric superlattices and multiferroics, follows. Opportunities and challenges in understanding the new ferroelectric properties will be discussed in two example systems, $PbTiO_3/SrTiO_3$ superlattices and $BiFeO_3$.

1.1 Ferroelectrics Oxides

The origin of ferroelectricity is closely linked to the polar displacement of ions with respect to a centrosymmetric structure. The ferroelectric phase can be viewed as a low-symmetry polar phase referred to a high-symmetry nonpolar structure. A spontaneous ferroelectric polarization can thus only exist in noncentrosymmetric crystallographic structures. Perovskite oxides are a family of ferroelectric with a chemical formula ABO_3. In the unit cell representation, the A-site and B-site cations and oxygen anions occupy the corners, body centers and face centers, respectively. The atoms are displaced away from their centrosymmetric positions so that the unit cell exhibits a dipole moment. In Fig. 1.1, the B-site atomic displacement is exaggerated to show the polarization-up and polarization-down states. In more realistic structures than the one shown in Fig. 1.1, however, both A-site and B-site atomic displacements relative to the oxygen octahedra can contribute to ferroelectricity. For example, the A-site atomic displacement of Pb atoms in $PbTiO_3$ is substantial due to the hybridization of Pb 6*s* and oxygen 2*p* states, and is the main contribution to the spontaneous polarization [13]. Understanding the atomic origins of ferroelectricity is crucial to design new ferroelectric systems including multiferroics.

The macroscopic symmetry breaking associated with the transition from the high-temperature structure to the low-temperature ferroelectric phase is the result of the atomic-scale coupling of the spontaneous polarization and atomic polar displacement. The ferroelectric phase can be induced by varying temperature [14], hydrostatic pressure [15], and epitaxial strain [16]. These phase transitions can be described by a Laudau theory with the spontaneous polarization as the order parameter [14]. The transformation

between phases has important influence on structural and electronic properties. For example, a divergence of dielectric constant occurs near the ferroelectric-to-paraelectric transition at Curie temperature, as described by the Curie-Weiss law [14]. The effects of phase transitions on lattice structure and polarization domains will be discussed more extensively in the following chapters.

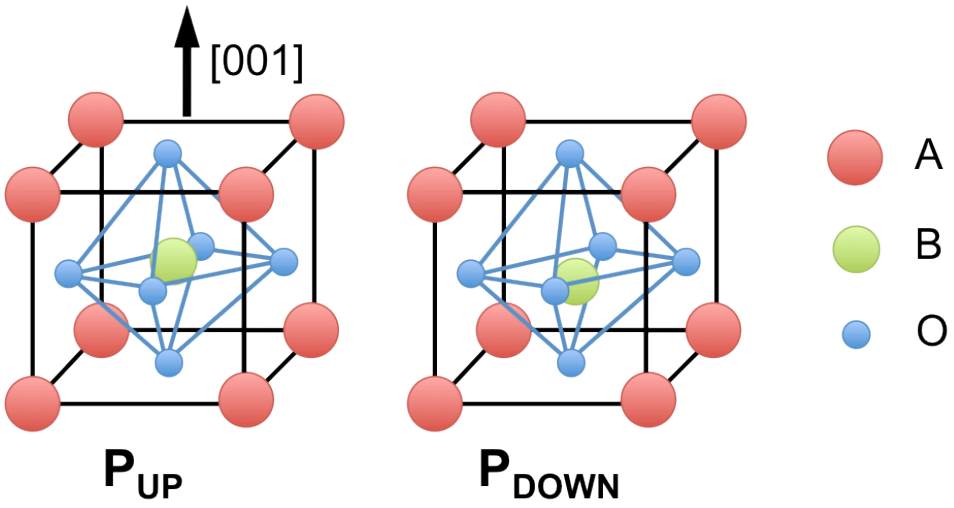

Figure 1.1 Unit cell representations for polarization-up and polarization-down states in a perovskite ferroelectric.

The characteristic experimental feature of a ferroelectric is a spontaneous electric polarization that can be switched under sufficiently large electric fields [14]. The ferroelectric crystal structure can be thought of as exhibiting two or more metastable states that differ in the direction of the spontaneous polarization. An applied electric field favors the state with the polarization parallel to the electric field. The polarization state of a ferroelectric can therefore be controlled with an external electric field.

The spontaneous polarization of a ferroelectric can be characterized experimentally by acquiring a polarization-electric-field hysteresis loop. The macroscopic polarization is usually measured by integrating the displacement current

flowing through a ferroelectric capacitor in a time-dependent electric field, typically a triangle-wave-form electric field. Fig. 1.2 shows a hysteresis loop of a $Pb(Zr,Ti)O_3$ ferroelectric thin film. The linear component of the hysteresis loop, evident at large electric fields, arises from the linear dielectric polarization of the ferroelectric. The polarization changes dramatically at the coercive electric field, 400 kV/cm in Fig. 1.2, where a polarization switching process occurs. The key feature of a ferroelectric hysteresis loop is that the switched polarization is conserved after removing the applied electric field and that the polarization has different values depending on the history of applied electric fields. The remnant polarization is measured from the hysteresis loops by extrapolating the saturation values of the polarization from both the positive and negative electric fields to zero applied electric field. The accepted value of the remnant polarization is half of the difference between the two extrapolated zero-field polarizations. In the example shown in Fig. 1.2, the spontaneous polarization is 45 $\mu C/cm^2$.

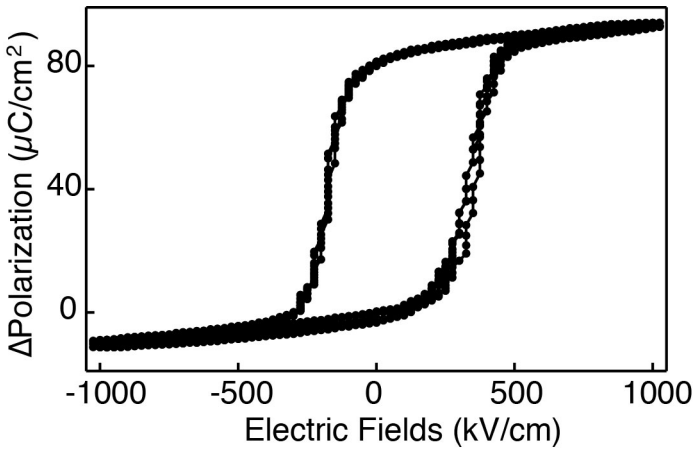

Figure 1.2 Hysteresis loop of a 80-nm $Pb(Zr,Ti)O_3$ ferroelectric thin film. The applied electric fields have a frequency of 100 Hz and a maximum magnitude of 8 V.

1.2 Polarization Domains

The fact that ferroelectrics can exhibit multiple polarization states is the basis for their practical application in memory devices, which in turn drives extensive study of domain formation and polarization switching [17]. The equilibrium arrangement of polarization domains is sensitive to both electrostatic and mechanical boundary conditions. Stripe domains are commonly found, with different orientations of polarization in adjacent domains [18]. More complex domain patterns including flux-closure domains have also been recently observed in ferroelectric nanostructures [19] and at interfaces of ferroelectric thin films [20].

The depolarization field plays an important role in the formation of domains. The depolarization field is a way of parameterizing the additional energy required to form a polarized material with boundaries at which the polarization rapidly transitions to zero, for example an interface between a ferroelectric and the vacuum. As is the case in ferromagnetic materials [21], ferroelectrics with a uniform polarization are energetically unstable in the presence of this depolarization field. The electrostatic energy associated with the depolarization field can be reduced by compensating the bound charges due to the polarization discontinuity, for example, with surface absorbates or with carriers provided by metallic electrodes. However, the charge compensation cannot eliminate the depolarization field completely, especially in ferroelectric ultrathin films [1, 22]. The uniform state is thus often not observed and polarization domains, with a reduced net polarization are instead formed.

Stripe domains with antiparallel polarizations are the simplest domain pattern and have been studied as a model system. These 180° stripe domains have been found

experimentally, in $PbTiO_3$ thin films [1, 23] and in $PbTiO_3/SrTiO_3$ superlattice thin films [9, 24]. The width of the domains in ferromagnetic materials is proportional to the square root of the film thickness, known as Kittel's law [18, 21]. In ferroelectric materials the formation of stripe domains is a result of the competition between the electrostatic energy of the depolarization field and the energy of creating domain walls [18]. Consider a ferroelectric thin film with a thickness of h and a domain wall width of W, as shown in Fig. 1.3(a). The corresponding electrostatic energy is proportional to W. The energy associated with creating the domain walls of the stripe domain pattern is proportional to the thickness and the domain wall density, proportional to h/W. Minimizing the total energy consisting of energy of depolarization fields and domain walls, gives the result that $W \propto \sqrt{h}$, which is the Kittel's law.

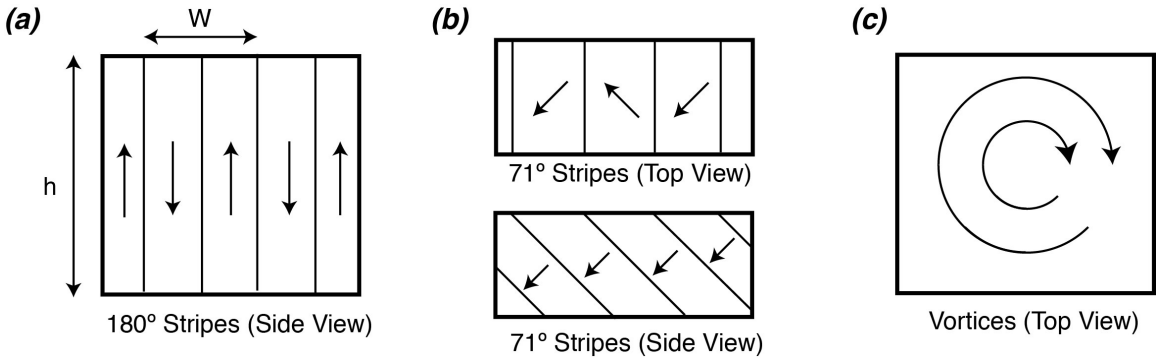

Figure 1.3 Schematics of domain patterns. (a) 180-degree stripe domains. (b) 71-degree stripe domains from both top and side views. (c) Domain vortices.

In ferroelectric thin films, the epitaxial stress is second driving force for domain formation. The epitaxial stress results from a mismatch between the lattice constants of the ferroelectric thin film and the substrate on which it is grown. The associated elastic energy increases with the film thickness. For films thicker than a critical value, the formation of mechanically distinct domains releases the elastic energy [25, 26]. Similar to

the domains driven by the depolarization field, the elastic domains form at the expense of interfacial energy of domain walls. The equilibrium domain pattern exhibits different configurations, depending on the crystallographic symmetry of the ferroelectric phase. For example, in a rhombohedral ferroelectric thin film, 71° domains develop with 101-family domain walls (Fig. 1.3 (b)) [27, 28]. The effect of polarization is equally crucial. In this case, the polarization of neighboring 71° domains is arranged head-to-tail so that the electrostatic energy is minimized.

Flux-closure domains exhibiting a novel polarization vortex consisting of continuous dipole rotation have predicted to occur in ferroelectric nanostructures [29]. The mechanism of the vortex formation and the effect on the functional properties are beginning to be understood. Evidence of flux-closure domains has been found at the boundaries of domains near the interfaces of ferroelectric thin films with high resolution transmission electron microscopy [20, 30]. In ferroelectric nanodots, intersections of 90° stripe domains were observed, forming a quadrant pattern to release the disclination stress [31, 32]. A flux-close domain can also be created artificially with piezoelectric force microscopy, for example, in a continuous $BiFeO_3$ ferroelectric thin film [33]. The domain vortex created in this way exhibits far larger electrical conductivity than the thin film materials far from the vortex [33].

1.3 Piezoelectricity

Ferroelectrics are within a subclass of piezoelectric materials. Piezoelectricity is the coupling between the electric polarization and the mechanical strain. The direct piezoelectric effect describes the change of the electric polarization produced by an external stress and the converse piezoelectric effect describes the mechanical strain that

results from applied electric fields. We will focus on the converse piezoelectric effect in ferroelectrics in the following discussion.

The piezoelectric effect can be represented with a third-rank tensor d_{ijk}, the piezoelectric coefficient, linking the applied electric fields with strain as in

$$x_{ij} = d_{ijk} E_k , \tag{1.1}$$

where E_k is the applied electric field, x_{ij} is the resulting strain, and i, j, and k are indices of crystallographic axes. The piezoelectric coefficient d_{ijk} is symmetric in j and k, and high crystallographic symmetry further reduces the number of the independent components of the piezoelectric coefficient. A Voigt notation is introduced to simplify the piezoelectric coefficient to an effective second-rank tensor d_{ij}.

The piezoelectricity in ferroelectrics arises from an electrostriction effect [34]. Electrostriction is a universal materials property relating the strain to the electric polarization

$$x_{ij} = Q_{ijkl} P_k P_l . \tag{1.2}$$

Here Q_{ijkl} and P_i are the electrostriction coefficient and polarization respectively. For ferroelectrics, the electric polarization consists of the spontaneous polarization and the field-induced polarization. Substitute $P_i = P_i^S + \varepsilon_0 \chi_{ij} E_j$ into Eq. (1.2) gives

$$x_{ij} = Q_{ijkl} P_k^S P_l^S + Q_{ijkl} \varepsilon_0 (P_k^S \chi_{km} + P_l^S \chi_{lm}) E_m + Q_{ijkl} \varepsilon_0^2 \chi_{km} \chi_{lm} E_m^2 , \tag{1.3}$$

where P_i^S is the spontaneous polarization, ε_0 is the vacuum permittivity, χ_{ij} is the dielectric susceptibility tensor. The first term on the right hand side of Eq. (1.3) defines the spontaneous strain with respect to the high-symmetry paraelectric phase. The third term is proportional to the square of the applied electric field and is generally negligible

compared to the second term. By neglecting the third term, the strain is proportional to the electric field with a piezoelectric coefficient expressed as

$$d_{mij} = Q_{ijkl}\varepsilon_0(P_k^S\chi_{km} + P_l^S\chi_{lm}), \tag{1.4}$$

The most widely used piezoelectric coefficient is d_{33}, relating the longitudinal strain to an external electric field parallel with one of the crystallographic axes. The d_{33} is proportional to the spontaneous polarization and can be expressed as [35]

$$d_{33} = 2\varepsilon_0\chi_{33}Q_{11}P_3^S . \tag{1.5}$$

The large spontaneous polarization is the reason the ferroelectrics are the most important piezoelectric martials.

Piezoelectricity can be modified by adjusting the composition of the material, the applied electric field, or mechanical boundary conditions so that the system is near a boundary between different structural phases [36]. A number of properties including both the piezoelectric and dielectric properties can be enhanced in the proximity of a phase boundary. The divergence of functional properties near a phase boundary can be understood in the picture of a soft phonon mode. In a paraelectric-to-ferroelectric phase transition, the soft mode is the lowest optical phonon mode, which exhibits a vanishing frequency at the transition [37, 38]. In the phase transition between two ferroelectric phases, the spontaneous polarization rotates in order to accommodate the new crystallographic symmetry, and can exhibit a similar softening of phonon modes [3]. The characteristic phonon softening at the phase transition is related to the divergence of the dielectric constant through the Lyddane-Sachs-Teller relation [39]. As indicated by Eq. (1.5) and discussed extensively in Damjanovic *et al.* as well as in Mitsui and Furuichi *et al.* [40, 41], the divergence of the dielectric constant, leads to an increase in the

piezoelectric coefficients. The components of the dielectric constant transverse to the principle axis of the emerging new phase are particularly important.

In Chapter 5, the enhancement of properties near phase transitions will be applied to the change in the piezoelectric properties of $BiFeO_3$ near a field-induced rhombohedral-to-tetragonal phase transition. Our explanation builds on what is observed in the ferroelectric alloy, which exhibits a morphtropic phase boundary between the tetragonal phase near the $PbTiO_3$ composition and the rhombohedral phase of the $PbZrO_3$ component. The $Pb(Zr,Ti)O_3$ system is a prominent example of the divergence of piezoelectric coefficients due to the softening of phonon modes [36].

The piezoelectric properties are affected by extrinsic factors. Here we use the term intrinsic contribution to refer to the structural change of a single domain to applied electric field, and the extrinsic contribution refers to the reorientation of domains and domain wall movement that effectively change the macroscopic dimension of ferroelectrics. In bulk ferroelectric ceramics, non-180° ferroelastic domains are displaced by electric fields, leading to a field-dependent piezoelectric coefficient that is much larger the intrinsic value. This piezoelectric nonlinearity is empirically described by a Rayleigh law as in [42, 43]

$$d' = d_0 + \alpha E \,, \tag{1.6}$$

where d' is the effective piezoelectric coefficient, d_0 is the intrinsic piezoelectric coefficient, and α is the Rayleigh coefficient.

In ferroelectric thin films where the non-180° ferroelastic domain walls are pinned, the 180° ferroelectric domain walls dominate the extrinsic contribution. With

only 180° domain walls the extrinsic effect can be estimated by averaging the intrinsic piezoelectric coefficient over domains with antiparallel polarizations. The relative volume of each polarization of the 180° domains can be changed by applied electric fields via a reversible ferroelectric domain wall movement, described by a dynamical poling model [44, 45]. The extrinsic effect in systems with displacement of 180° domain walls is accounted for by modifying the Eq. (1.6) with an additional electric-field-dependent term to the intrinsic piezoelectric coefficient.

1.4 Ferroelectric/Dielectric Superlattices

Ferroelectric/dielectric superlattices are designed based on the use of the interfaces to control materials properties. Structurally, the superlattice thin film consists of a periodic sequence of alternating component layers (Fig. 1.4). Although superlattice structure have been developed in a variety of materials over several decades, including III-V semiconductors [46, 47], it has only recently become possible to fabricate complex oxide superlattices with precise layer-by-layer control [48]. By varying the chemical formulas, relative ratio, and absolute layer number of superlattice components, a new set of degrees of freedom has emerged to manipulate the interfacial coupling and therefore control the functional properties [49]. Among many possible configurations of complex oxide superlattices, I will focus on ferroelectric/dielectric superlattices.

The dielectric layers of a ferroelectric/dielectric superlattice are polarized to minimize the electrostatic energy that would arise due to the discontinuity of the polarization. Neaton *et al*. predict that the macroscopic polarization of a superlattice thin film can even be larger than that of a uniform-composition bulk material of the ferroelectric component [50]. In epitaxial thin films, where the ferroelectric layers are

compressively strained along the in-plane direction, the out-of-plane polarization is enhanced via the coupling to structure. However, in relatively thick films, with thicknesses on the order of 100 nm, the ferroelectric layers are normally relaxed via misfit dislocation or by the formation of ferroelastic domains. As a result, the polarization enhancement is smaller. In the case of superlattices, however, by designing sufficiently thin ferroelectric layers and a dielectric component with the same chemical formula as the substrate, each set of ferroelectric layers can be coherently strained. The polarization enhancement of ferroelectric layers due to this high strain state can therefore be shared with dielectric layers. An overall polarization larger than the bulk ferroelectric can be achieved by controlling the ratio of the superlattice components [49, 50]. This tunability of polarization can also be extended into multi-component superlattices [48, 51].

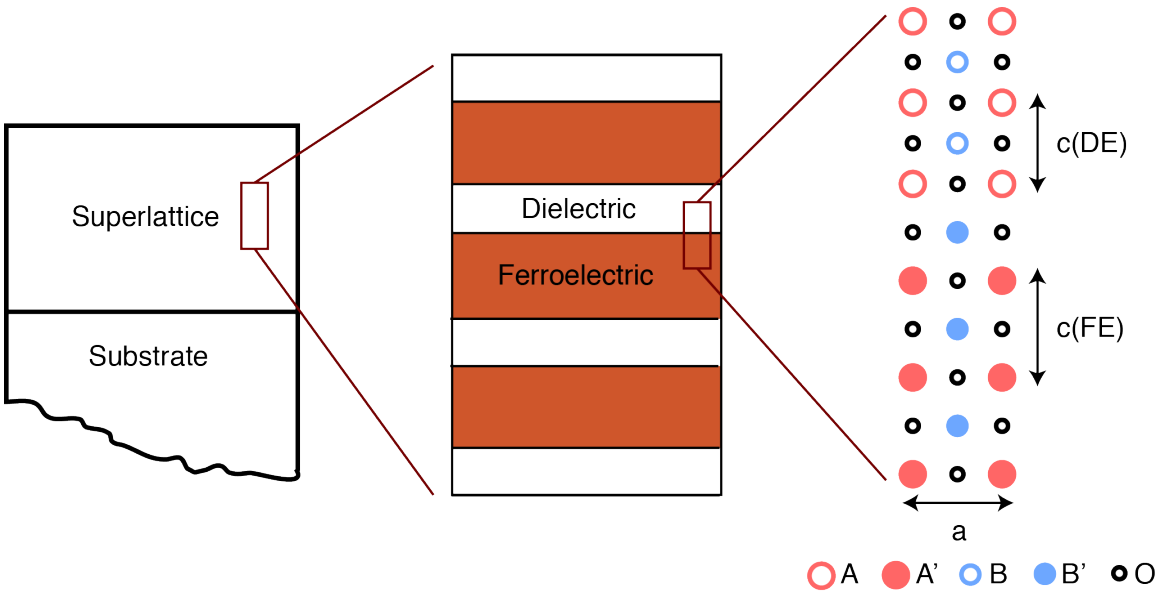

Figure 1.4 Schematics of a ferroelectric/dielectric superlattice thin film. In the right panel, the atomic structure of a perovskite superlattice is shown as an example. The ferroelectric and dielectric components share the same in-plane lattice parameter, but the out-of-plane lattice parameters can be different.

The modification of the ferroelectricity is further complicated when other structural instabilities such as antiferrodistortive order are taken into account. This nonpolar zone-boundary instability is commonly found in perovskite oxides where the tolerance factor $(r_A + r_O)/\sqrt{2}(r_B + r_O)$ is smaller than 1. Oversized B-site atoms push the surrounding oxygen atoms and result in oxygen octahedral rotations [52]. Examples of perovskites exhibiting antiferrodistortion include $CaTiO_3$ and $SrTiO_3$. For more in-depth discussion and classification of oxygen octahedral rotations, one can refer to Glazer *et al.* [53].

The antiferrodistortive order is often considered as a competing instability with the ferroelectric order. In superlattices where the two components are ferroelectric and antiferrodistortive respectively in their bulk forms, the competition of these instabilities results in unusual structural and ferroelectric properties. Theoretical calculations have predicted that overall polarization of the superlattice is suppressed due to existence of the oxygen octahedral rotations, particularly in the atomic unit cells of the dielectric components that are far from the ferroelectric/dielectric interface [54]. More importantly, the competition of ferroelectric and antiferrodistortive orders at the interfaces results in a reduction of the octahedral rotations and a local enhancement of the polarization [54]. An immediate consequence of this interfacial enhancement is that the functional properties are connected to the number of interfaces per unit length within the superlattice thin film.

The competition of structural instabilities is sensitive to external electric fields. Under a sufficiently large electric field, the antiferrodistortive order can be completely suppressed, resulting in a phase transition into an effectively uniform ferroelectric [55].

An increase of the piezoelectricity can be expected after this nonpolar-to-polar phase transition.

We have experimentally found that the piezoelectricity of $BaTiO_3/CaTiO_3$ depends on the timescale over which the mechanical response is measured. At the nanosecond timescale the structural distortion in response to a given field is much less than what is observed at the millisecond timescale. This observation fits with the prediction that the field induces a phase transition to a more responsive state [56]. We have further observed that the millisecond piezoelectricity agrees with the value for the high-symmetry ferroelectric phase. Finally, the piezoelectric strain developed over the course of applied electric fields is evenly shared between $BaTiO_3$ and $CaTiO_3$ component, a behavior similar to ferroelectrics with a uniform polarization [57, 58].

In some circumstances, however, the ferroelectric and antiferrodistortive order are coupled together, giving rise to improper ferroelectricity. In ultrathin $PbTiO_3/SrTiO_3$ superlattices where the thickness of each component is less than two atomic layers, the ground state combines both the ferroelectric and antiferrodistortive distortions [2]. This coupling is an interfacial effect, due to the asymmetric environment for the interfacial oxygen atoms. The ferroelectric polarization is no longer the primary order parameter describing the phase transitions. As a result, a temperature-insensitive dielectric constant is observed, a characteristic for improper ferroelectrics.

A stripe polarization domain state allows the superlattice to have simultaneously a low total polarization and a large polarization in the ferroelectric component. The eventual equilibrium state depends on the electrostatic coupling between ferroelectric

layers [7, 59]. A stripe domain state emerges when the dielectric layers are sufficiently thick to decouple ferroelectric layers. The transition between the weakly-coupled regime (where the stripe domain is stable) and the strongly-coupled regime (where a uniform polarization is stable) can be inferred from the measurement of Curie temperature [60] and domain period [61] as a function of the thickness of the dielectric layers.

In weakly-coupled superlattices, the stripe domains are geometrically similar to what have been found in ultrathin ferroelectric films [23], and the domain period follows a similar Kittel's law. Note here however, the domain period is proportional to the square-root of the thickness of the decoupled ferroelectric layers, not the thickness of the entire film [61]. The domain structure is extended into the dielectric layers, showing a large coherence length comparable to the film thickness. The detailed polarization configuration is complicated by the non-uniform polarization across the component layers. First-principles calculations predict in-plane component of the polarization and polarization vortices at the interfaces [62].

Little was previously known about the dynamics of the stripe domain pattern. A major part of this thesis is devoted to answer several questions here:

(i) What is switching mechanism of the nanoscale stripe domains under applied electric fields?

(ii) How do the individual ferroelectric and dielectric layers respond to applied electric fields?

(iii) What is the role of the atomic-scale polarization variation on the transformation of the nanoscale stripe domains?

1.5 Multiferroic $BiFeO_3$

Materials known as multiferroics exhibit magnetic ordering in addition to ferroelectricity. This property is fascinating because through it one can in principle control the polarization and magnetism through both external electric or magnetic fields. There are, however, only a few multiferroic oxides, due to a competition between ferroelectric and magnetic orders in most transition metal oxides [63]. Specifically, ferroelectric order originates from the off centering of cations, which requires empty *d* orbitals. In contrast, magnetic order usually requires partially filled *d* orbitals.

One solution to construct a single-phase multiferroic is to have different atoms responsible for ferroelectric and magnetic orders. This is the case for $BiFeO_3$, to date the only material showing both ferroelectric and antiferromagnetic ordering simultaneously at room temperature. The hybridization of Bi lone pair 6*s* and O 2*p* electrons provides the ferroelectricity [64], while the magnetization comes from Fe^{+3}. Other examples include $BiMnO_3$, $BiCrO_3$, and $PbVO_3$ [65].

Other mechanisms have been explored to induce ferroelectricity in transition metal magnetic oxides [65, 66]. In hexagonal manganite such as $YMnO_3$, the ferroelectricity is induced by a pure geometric effect due to the buckling of MnO_5 polyhedra and the displacement of Y ions [67]. Ferroelectricity can also be induced directly from the magnetic ordering. In orthorhombic manganites in which the spatially inhomogeneous spin forms a spiral pattern, the anisotropic superexchange interaction termed as Dzyoloshinskii-Moriya interaction [68, 69] favors a symmetry lowering and displaces the oxygen ions with respect to Mn ions [70]. Another group of multiferroics exhibit electronic ferroelectricity originating from the asymmetric charge ordering [71].

I focus on the room-temperature multiferroic $BiFeO_3$. Bulk $BiFeO_3$ has a rhombohedrally distorted perovskite structure at room temperature (a = 3.965 Å, α = 89.4° [72]), with a transition to the high-temperature centrosymmetric paraelectric phase at the Curie temperature for ferroelectricity, 1103 K. The Néel temperature defining the magnetic order is 643 K [73]. The rhombohedral distortion is sufficiently small that $BiFeO_3$ is usually described in pseudocubic structure for convenience. The direction of spontaneous polarization is along the body-diagonal $<111>_{pc}$, as shown in Fig. 1.5(a). The magnitude of polarization was believed to be very small for over 30 years until Wang *et al.* reported a measured polarization as large as 90-100 μC/cm^2 in an epitaxial $BiFeO_3$ thin film [73]. Later measurements on single crystal phase $BiFeO_3$ [74] and first-principles calculations [75] confirmed the initial observations of the large polarization.

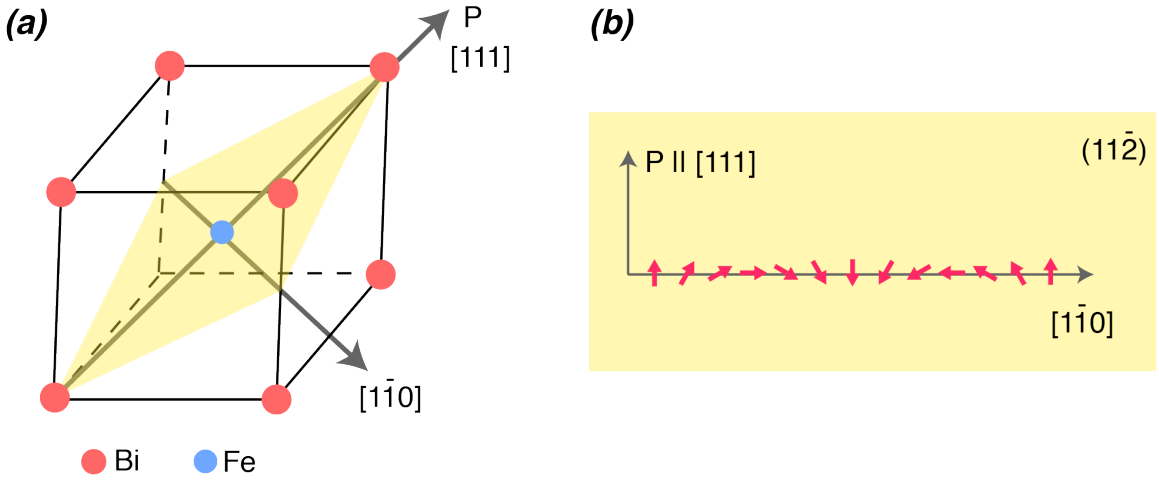

Figure 1.5 (a) Schematics of the spontaneous polarization and the propagation direction of the spin cycloid in a $BiFeO_3$ unit cell. The yellow-color plane represents the magnetic easy plane where the spin rotates. The oxygen atoms are omitted. (b) Schematics showing the rotating of spin (red arrows) in a spin cycloid.

In terms of the magnetic structure, $BiFeO_3$ bulk has a G-type antiferromagnetic spin configuration where the neighboring Fe ions have antiparallel spins [76]. However, unlike a perfect G-type antiferromagnetic, the existence of the ferroelectric polarization

breaks the inversion symmetry and allows a more complex magnetic order via the inverse Dzyoloshinskii-Moriya interaction [77-79]. This interaction leads to a local canted spin and a long-range spin cycloid, with a period of 62-64 nm and a propagation vector perpendicular to the polarization [80]. The magnetic easy plane where the spin rotates is defined by the propagation vector and the spontaneous polarization, as shown in Fig. 1.5.

A series of efforts have been made to understand the coupling between the ferroelectric and magnetic order in $BiFeO_3$. While the linear magnetoelectric interaction is believed to be weak due to the spin cycloid, the formation of the spin cycloid itself can be viewed as a product of a higher-order coupling of polarization to the gradient of magnetism [77, 79]. This nonlinear magnetoelectric interaction is a key mechanism for switching the magnetic easy plane via the switching of the polarization, as has been observed in $BiFeO_3$ single crystals [81, 82]. The spin wave corresponding to the oscillation of spins in and out of the cycloidal plane shows frequency shifts under external electric fields, indicating additional linear magnetoelectric interactions at low fields [83]. The internal coupling of ferroelectric and magnetic orders within a multiferroic can also be combined with interfacial exchange interactions. It is recently shown that the magnetic properties of ferromagnetic layers are controlled by electrically switching the multiferroic component in a $CoFe/BiFeO_3$ heterostructure [84].

In addition to the coupling between the ferroelectric and magnetic order, both types of order are also strongly related to the crystallographic structure. Strain engineering in epitaxial multiferroic thin film is commonly used to tailor the functional properties. With a moderate epitaxial strain (< 1%), the spontaneous polarization is rotated away form the $<111>_{pc}$ due to a strain-induced monoclinic distortion [85]. The

distortion can be so dramatic at large epitaxial strain that $BiFeO_3$ adopts a tetragonal symmetry with a giant tetragonality and an increased polarization of 150 $\mu C/cm^2$ [86, 87]. The epitaxial strain tends to destabilize the spin cycloid and induce a collinear antiferromagnetic order. The long-range spin cycloid has only been observed in either partially relaxed thick films [88] or thin films with little mismatch strain [89]. A recent study by Sando *et al.* shows a new type of spin cycloid in films with a small tensile strain [89], providing new insight into the coupling between magnetism and structure.

The structure of $BiFeO_3$ thin films under external perturbations, however, has not yet been fully understood. As introduced earlier, the piezoelectricity of a ferroelectric can be enhanced by placing the system near the morphtropic phase boundary. Similar modification of the piezoelectricity have been reported in $BiFeO_3$ by inducing phase transitions via large epitaxial strain [86] or rare-earth elements doping [90]. Chapter 5 describes structural changes in epitaxial $BiFeO_3$ thin films in high electric fields. The nonlinearity of the high-filed piezoelectricity described there arises from the proximity of the system to the rhombohedral-to-tetragonal phase transition [11].

An additional crucial challenge in multiferroic $BiFeO_3$ is to further the understanding of the optical modification of structural properties at the ultrafast timescale. A recent work in prototype ferroelectric $PbTiO_3$ has shown a picosecond-timescale strain following a femtosecond laser pulse [91]. Several mechanisms contribute to the ultrafast strain. Two important components, involving nonlinear optical interaction and a carrier-mediated piezoelectric effect, will be discussed in more detail in Chapter 6. A key question is to what degree the mechanisms observed in $PbTiO_3$ can be applied to $BiFeO_3$, which has a more complicated crystallographic structure and domain

morphology and the additional magnetic degree of freedom. Studies of photoinduced effects in $BiFeO_3$ have emphasized the switchable photovoltaic effect and an above-bandgap photo voltage [4, 92]. In Chapter 6, I describe a detailed structural analysis of $BiFeO_3$ thin films at the picosecond timescale. The thickness dependence of strain relaxation and the broadening of x-ray diffraction peaks provide a more in-depth understanding of ultrafast manipulation of structural degree of freedom.

1.6 References

[1] D. D. Fong *et al.*, "*Ferroelectricity in Ultrathin Perovskite Films,"* Science **304**, 1650 (2004).

[2] E. Bousquet *et al.*, "*Improper Ferroelectricity in Perovskite Oxide Artificial Superlattices,"* Nature **452**, 732 (2008).

[3] H. X. Fu, and R. E. Cohen, "*Polarization Rotation Mechanism For Ultrahigh Electromechanical Response in Single-crystal Piezoelectrics,"* Nature **403**, 281 (2000).

[4] T. Choi *et al.*, "*Switchable Ferroelectric Diode and Photovoltaic Effect in $BiFeO_3$,"* Science **324**, 63 (2009).

[5] S. Lisenkov, I. Ponomareva, and L. Bellaiche, "*Unusual Static and Dynamical Characteristics of Domain Evolution in Ferroelectric Superlattices,"* Phys. Rev. B **79**, 024101 (2009).

[6] S. Young, and A. Rappe, "*First Principles Calculation of the Shift Current Photovoltaic Effect in Ferroelectrics,"* Phys. Rev. Lett. **109**, 116601 (2012).

[7] V. Stephanovich, I. Luk'yanchuk, and M. Karkut, "*Domain-enhanced Interlayer Coupling in Ferroelectric/Paraelectric Superlattices,"* Phys. Rev. Lett. **94**, 047601 (2005).

[8] A. Torres-Pardo *et al.*, "*Spectroscopic Mapping of Local Structural Distortions in Ferroelectric $PbTiO_3/SrTiO_3$ Superlattices at the Unit-cell Scale,"* Phys. Rev. B **84**, 220102(R) (2011).

[9] J. Y. Jo *et al.*, "*Nanosecond Dynamics of Ferroelectric/Dielectric Superlattices,"* Phys. Rev. Lett. **107**, 055501 (2011).

[10] P. Chen *et al.*, "*Field-Dependent Domain Distortion and Interlayer Polarization Distribution in $PbTiO_3/SrTiO_3$ Superlattices,"* Phys. Rev. Lett. **110**, 047601 (2013).

[11] P. Chen *et al.*, "*Nonlinearity in the High-electric-field Piezoelectricity of Epitaxial $BiFeO_3$ on $SrTiO_3$,"* Appl. Phys. Lett. **100**, 062906 (2012).

[12] H. Wen *et al.*, "*Electronic Origin of Ultrafast Photoinduced Strain in $BiFeO_3$,"* Phys. Rev. Lett. **110**, 037601 (2013).

[13] R. Cohen, "*Origin of Ferroelectricity in Perovskite Oxides,"* Nature **358**, 136 (1992).

[14] A. F. Devonshire, "*Theory of Ferroelectrics,"* Advances in Physics **3**, 85 (1954).

[15] G. A. Samara, "*Vanishing of the Ferroelectric and Antiferroelectric States in KH2PO2-Type Crystals at High Pressure,"* Phys. Rev. Lett. **27**, 103 (1971).

[16] J. H. Haeni *et al.*, "*Room-temperature Ferroelectricity in Strained $SrTiO_3$,"* Nature **430**, 758 (2004).

[17] W. J. Merz, "*Domain Formation and Domain Wall Motions in Ferroelectric $BaTiO_3$ Single Crystals,"* Phys. Rev. **95**, 690 (1954).

[18] T. Mitsui, and J. Furuichi, "*Domain Structure of Rochelle Salt and KH_2PO_4,"* Phys. Rev. **90**, 193 (1953).

[19] A. Schilling *et al.*, "*Shape-induced Phase Transition of Domain Patterns in Ferroelectric Platelets,"* Phys. Rev. B **84**, 064110 (2011).

[20] C.-L. Jia *et al.*, "*Direct Observation of Continuous Electric Dipole Rotation in Flux-Closure Domains in Ferroelectric $Pb(Zr,Ti)O_3$,"* Science **331**, 1420 (2011).

[21] C. Kittel, "*Theory of the Structure of Ferromagnetic Domains in Films and Small Particles,"* Phys. Rev. **70**, 965 (1946).

[22] J. Junquera, and P. Ghosez, "*Critical Thickness for Ferroelectricity in Perovskite Ultrathin Films,"* Nature **422**, 506 (2003).

[23] S. K. Streiffer *et al.*, "*Observation of Nanoscale 180 Degrees Stripe Domains in Ferroelectric $PbTiO_3$ Thin Films,"* Phys. Rev. Lett. **89**, 067601 (2002).

[24] P. Zubko, N. Stucki, C. Lichtensteiger, and J. M. Triscone, "*X-Ray Diffraction Studies of 180 degrees Ferroelectric Domains in $PbTiO_3/SrTiO_3$ Superlattices under an Applied Electric Field,"* Phys. Rev. Lett. **104**, 187601 (2010).

[25] A. L. Roitburd, "*Equilibrium Structure of Epitaxial Layers,"* Phys. Status Solidi A **37**, 329 (1976).

[26] W. Pompe, X. Gong, Z. Suo, and J. S. Speck, "*Elastic Energy Release due to Domain Formation in the Strained Epitaxy of Ferroelectric and Ferroelastic Films,"* J. Appl. Phys. **74**, 6012 (1993).

[27] J. Speck, and W. Pompe, "*Domain Configurations due to Multiple Misfit Relaxation Mechanisms in Epitaxial Ferroelectric Thin Films. I. Theory,"* J. Appl. Phys. **76**, 466 (1994).

[28] Y.-H. Chu *et al.*, "*Nanoscale Control of Domain Architectures in $BiFeO_3$ Thin Films,"* Nano Lett. **9**, 1726 (2009).

[29] I. I. Naumov, L. Bellaiche, and H. Fu, "*Unusual Phase Transitions in Ferroelectric Nanodisks and Nanorods,"* Nature **432**, 737 (2004).

[30] C. T. Nelson *et al.*, "*Spontaneous Vortex Nanodomain Arrays at Ferroelectric Heterointerfaces,"* Nano Lett. **11**, 828 (2011).

[31] A. Schilling *et al.*, "*Domains in Ferroelectric Nanodots,"* Nano Lett. **9**, 3359 (2009).

[32] L. J. McGilly, and J. M. Gregg, "*Polarization Closure in $PbZr_{0.42}Ti_{0.58}O_3$ Nanodots,"* Nano Lett. **11**, 4490 (2011).

[33] N. Balke *et al.*, "*Enhanced Electric Conductivity at Ferroelectric Vortex Cores in $BiFeO_3$,"* Nature Phys. **8**, 81 (2011).

[34] V. Sundar, and R. E. Newnham, "*Electrostriction and Polarization,"* Ferroelectrics **135**, 431 (1992).

[35] M. J. Haun *et al.*, "*Thermodynamic Theory of $PbTiO_3$,"* J. Appl. Phys. **62**, 3331 (1987).

[36] R. Guo *et al.*, "*Origin of the High Piezoelectric Response in $PbZr_{1-x}Ti_xO_3$,"* Phys. Rev. Lett. **84**, 5423 (2000).

[37] A. A. Sirenko *et al.*, "*Soft-mode Hardening in $SrTiO_3$ Thin Films,"* Nature **404**, 373 (2000).

[38] M. Ahart *et al.*, "*Origin of Morphotropic Phase Boundaries in Ferroelectrics,"* Nature **451**, 545 (2008).

[39] R. Lyddane, R. Sachs, and E. Teller, "*On the Polar Vibrations of Alkali Halides,"* Phys. Rev. **59**, 673 (1941).

[40] M. Iwata, and Y. Ishibashi, "*Phenomenological Theory of Morphotropic Phase Boundary with Monoclinic Phase in Solid-solution Systems of Perovskite-type Oxide Ferroelectrics,"* Jpn. J. Appl. Phys. 1 **44**, 3095 (2005).

[41] D. Damjanovic, "*Comments on Origins of Enhanced Piezoelectric Properties in Ferroelectrics,"* IEEE. T. Ultrason. Ferr. **56**, 1574 (2009).

[42] D. Damjanovic, and M. Demartin, "*The Rayleigh Law in Piezoelectric Ceramics,"* J. Phys. D: Appl. Phys. **29**, 2057 (1996).

[43] D. Damjanovic, "*Stress and Frequency Dependence of the Direct Piezoelectric Effect in Ferroelectric Ceramics,"* J. Appl. Phys. **82**, 1788 (1997).

[44] S. Trolier-McKinstry, N. Bassiri Gharb, and D. Damjanovic, "*Piezoelectric Nonlinearity due to Motion of 180° Domain Walls in Ferroelectric Materials at Subcoercive Fields: A Dynamic Poling Model,"* Appl. Phys. Lett. **88**, 202901 (2006).

[45] N. B. Gharb, S. Trolier-McKinstry, and D. Damjanovic, "*Piezoelectric Nonlinearity in Ferroelectric Thin Films,"* J. Appl. Phys. **100**, 044107 (2006).

[46] A. Segmuller, and A. Blakeslee, "*X-ray Diffraction from One-dimensional Superlattices in* $GaAs_{1-x}P_x$ *Crystals,"* J. Appl. Crystallogr. **6**, 19 (1973).

[47] L. Esaki, and R. Tsu, "*Superlattice and Negative Differential Conductivity in Semiconductors,"* IBM Journal of Research and Development **14**, 61 (1970).

[48] H. N. Lee *et al.*, "*Strong Polarization Enhancement in Asymmetric Three-component Ferroelectric Superlattices,"* Nature **434**, 792 (2005).

[49] M. Dawber *et al.*, "*Tailoring the Properties of Artificially Layered Ferroelectric Superlattices,"* Adv. Mater. **19**, 4153 (2007).

[50] J. B. Neaton, and K. M. Rabe, "*Theory of Polarization Enhancement in Epitaxial* $BaTiO_3/SrTiO_3$ *Superlattices,"* Appl. Phys. Lett. **82**, 1586 (2003).

[51] S. M. Nakhmanson, K. M. Rabe, and D. Vanderbilt, "*Polarization Enhancement in Two- and Three-component Ferroelectric Superlattices,"* Appl. Phys. Lett. **87**, 102906 (2005).

[52] W. Zhong, and D. Vanderbilt, "*Competing Structural Instabilities in Cubic Perovskites,"* Phys. Rev. Lett. **74**, 2587 (1995).

[53] A. M. Glazer, "*The Classification of Tilted Octahedra in Perovskites,"* Acta Cryst. B **28**, 3384 (1972).

[54] X. F. Wu, K. M. Rabe, and D. Vanderbilt, "*Interfacial Enhancement of Ferroelectricity in $CaTiO_3/BaTiO_3$ Superlattices,"* Phys. Rev. B **83**, 020104 (2011).

[55] C. Swartz, and X. Wu, "*Modeling Functional Piezoelectricity in Perovskite Superlattices with Competing Instabilities,"* Phys. Rev. B **85**, 054102 (2012).

[56] P. Chen *et al.*, "*Domain- and Symmetry-transition Origins of Reduced Nanosecond Piezoelectricity in Ferroelectric/dielectric Superlattices,"* New J. Phys. **14**, 013034 (2012).

[57] J. Y. Jo *et al.*, "*Piezoelectricity in the Dielectric Component of Nanoscale Dielectric-Ferroelectric Superlattices,"* Phys. Rev. Lett. **104**, 207601 (2010).

[58] J. Y. Jo *et al.*, "*Component-specific Electromechanical Response in a Ferroelectric/dielectric Superlattice,"* Phys. Rev. B **82**, 174116 (2010).

[59] M. Sepliarsky *et al.*, "*Long-ranged Ferroelectric Interactions in Perovskite Superlattices,"* Phys. Rev. B **64**, 060101 (2001).

[60] E. Specht, H. Christen, D. Norton, and L. Boatner, "*X-Ray Diffraction Measurement of the Effect of Layer Thickness on the Ferroelectric Transition in Epitaxial $KTaO_3/KNbO_3$ Multilayers,"* Phys. Rev. Lett. **80**, 4317 (1998).

[61] P. Zubko *et al.*, "*Electrostatic Coupling and Local Structural Distortions at Interfaces in Ferroelectric/Paraelectric Superlattices,"* Nano Lett. **12**, 2846 (2012).

[62] P. Aguado-Puente, and J. Junquera, "*Structural and Energetic Properties of Domains in $PbTiO_3/SrTiO_3$ Superlattices from First Principles,"* Phys. Rev. B **85**, 184105 (2012).

[63] N. A. Hill, "*Why Are There so Few Magnetic Ferroelectrics?,"* J. Phys. Chem. B **104**, 6694 (2000).

[64] R. Seshadri, and N. A. Hill, "*Visualizing the Role of Bi 6s "Lone Pairs" in the Off-center Distortion in Ferromagnetic $BiMnO_3$,"* Chem. Mat. **13**, 2892 (2001).

[65] R. Ramesh, and N. A. Spaldin, "*Multiferroics: Progress and Prospects in Thin Films,"* Nature Mater. **6**, 21 (2007).

[66] S.-W. Cheong, and M. Mostovoy, "*Multiferroics: A Magnetic Twist for Ferroelectricity,"* Nature Mater. **6**, 13 (2007).

[67] B. B. Van Aken, T. T. M. Palstra, A. Filippetti, and N. A. Spaldin, "*The Origin of Ferroelectricity in Magnetoelectric $YMnO_3$,"* Nature Mater. **3**, 164 (2004).

[68] T. Moriya, "*Anisotropic Superexchange Interaction and Weak Ferromagnetism,"* Phys. Rev. **120**, 91 (1960).

[69] I. Dzyaloshinsky, "*A Thermodynamic Theory of "Weak" Ferromagnetism of Antiferromagnetics,"* Nucl. Instrum. Methods Phys. Res., Sect. A **4**, 241 (1958).

[70] I. A. Sergienko, and E. Dagotto, "*Role of the Dzyaloshinskii-Moriya Interaction in Multiferroic Perovskites,"* Phys. Rev. B **73**, 094434 (2006).

[71] N. Ikeda *et al.*, "*Ferroelectricity from Iron Valence Ordering in the Charge-frustrated System $LuFe_2O_4$,"* Nature **436**, 1136 (2005).

[72] F. Kubel, and H. Schmid, "*Structure of a Ferroelectric and Ferroelastic Monodomain Crystal of the Perovskite $BiFeO_3$,"* Acta Crystallogr., Sect. B: Struct. Sci **46**, 698 (1990).

[73] J. Wang *et al.*, "*Epitaxial $BiFeO_3$ Multiferroic Thin Film Heterostructures,"* Science **299**, 1719 (2003).

[74] D. Lebeugle, D. Colson, A. Forget, and M. Viret, "*Very Large Spontaneous Electric Polarization in $BiFeO_3$ Single Crystals at Room Temperature and its Evolution under Cycling Fields,"* Appl. Phys. Lett. **91**, 022907 (2007).

[75] J. B. Neaton *et al.*, "*First-principles Study of Spontaneous Polarization in Multiferroic $BiFeO_3$,"* Phys. Rev. B **71**, 014113 (2005).

[76] J. M. Moreau, C. Michel, R. GERSON, and W. J. James, "*Ferroelectric $BiFeO_3$ X-ray and Neutron Diffraction Study,"* J. Phys. Chem. Solids **32**, 1315 (1971).

[77] H. Katsura, N. Nagaosa, and A. V. Balatsky, "*Spin Current and Magnetoelectric Effect in Noncollinear Magnets,"* Phys. Rev. Lett. **95**, 057205 (2005).

[78] C. Ederer, and N. Spaldin, "*Weak Ferromagnetism and Magnetoelectric Coupling in Bismuth Ferrite,"* Phys. Rev. B **71**, 060401 (2005).

[79] A. M. Kadomtseva *et al.*, "*Space-time Parity Violation and Magnetoelectric Interactions in Antiferromagnets,"* Jetp Lett. **79**, 571 (2004).

[80] I. Sosnowska, T. P. Neumaier, and E. Steichele, "*Spiral Magnetic Ordering in Bismuth Ferrite,"* J. Phy. C: Solid State Phys. **15**, 4835 (1982).

[81] S. Lee *et al.*, "*Single Ferroelectric and Chiral Magnetic Domain of Single-crystalline $BiFeO_3$ in an Electric Field,"* Phys. Rev. B **78**, 100101 (2008).

[82] D. Lebeugle *et al.*, "*Electric-field-induced Spin Flop in $BiFeO_3$ Single Crystals at Room Temperature,"* Phys. Rev. Lett. **100**, 227602 (2008).

[83] P. Rovillain *et al.*, "*Electric-field Control of Spin Waves at Room Temperature in Multiferroic $BiFeO_3$,"* Nature Mater. **9**, 975 (2010).

[84] Y.-H. Chu *et al.*, "*Electric-field Control of Local Ferromagnetism Using a Magnetoelectric Multiferroic,"* Nature Mater. **7**, 478 (2008).

[85] H. W. Jang *et al.*, "*Strain-induced Polarization Rotation in Epitaxial (001) $BiFeO_3$ Thin Films,"* Phys. Rev. Lett. **101**, 107602 (2008).

[86] R. J. Zeches *et al.*, "*A Strain-Driven Morphotropic Phase Boundary in $BiFeO_3$,"* Science **326**, 977 (2009).

[87] J. Zhang *et al.*, "*Microscopic Origin of the Giant Ferroelectric Polarization in Tetragonal-like $BiFeO_3$,"* Phys. Rev. Lett. **107**, 147602 (2011).

[88] X. Ke *et al.*, "*Magnetic Structure of Epitaxial Multiferroic $BiFeO_3$ Films with Engineered Ferroelectric Domains,"* Phys. Rev. B **82**, 134448 (2010).

[89] D. Sando *et al.*, "*Crafting the Magnonic and Spintronic Response of $BiFeO_3$ Films by Epitaxial Strain,"* Nature Mater. **12**, 641 (2013).

[90] S. Fujino *et al.*, "*Combinatorial Discovery of a Lead-free Morphotropic Phase Boundary in a Thin-film Piezoelectric Perovskite,"* Appl. Phys. Lett. **92**, 202904 (2008).

[91] D. Daranciang *et al.*, "*Ultrafast Photovoltaic Response in Ferroelectric Nanolayers,"* Phys. Rev. Lett. **108**, 087601 (2012).

[92] S. Y. Yang *et al.*, "*Above-bandgap Voltages from Ferroelectric Photovoltaic Devices,"* Nature Nanotech. **5**, 143 (2010).

2 Time-Resolved X-ray Microdiffraction

2.1 X-ray Interaction with Electrons

X-ray scattering results are described through this thesis, including the results of experiments to determine the static structure and the structural evolution of ferroelectric oxide thin films. The structural sensitivity of x-ray scattering is in part because the wavelength of hard x-rays is on the order of 1 Å, matching the lattice spacing of inorganic crystals. Compared to other structural probes, x-ray scattering has several advantages. It is, in general, nondestructive with the exception of organic materials due to their higher reactivity. X-ray scattering requires relatively little sample preparation. By slightly adjusting the scattering geometry, x-ray scattering can either be used to probe surfaces, or bulk regions within the penetration depth on the order of several micrometers. The most important feature to the work reported in this thesis is that the high brilliance and unique temporal structure of x-ray beam provided by synchrotron radiation facilities enable structural measurements at the picosecond timescale.

X-ray interacts with electrons in a number of forms. This thesis will focus on the weak elastic scattering, in which the photon energies of incident and scattered x-rays are almost exactly equal. The amplitude of the scattered x-ray wave is proportional to the Thomson scattering radius, 2.82×10^{-5} Å, which allows accurate quantitative scattering simulations as described below. X-ray diffraction patterns measure the interference of scattered x-rays from many-electron systems. The condition for constructive interference from extended crystals is the Bragg equation [1]:

$$\lambda = 2d \sin\theta , \tag{2.1}$$

Here λ is the wavelength of the x-rays, d is the spacing of a set of lattice planes, θ is the incident angle of the x-ray beam with respect to the planes.

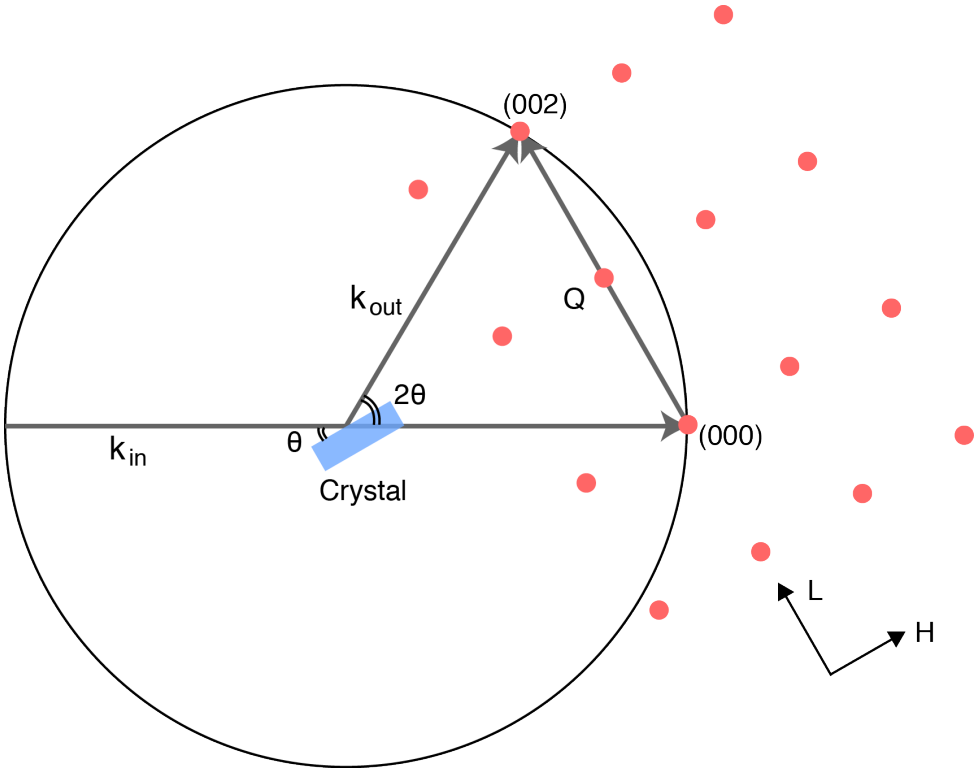

Figure 2.1 Ewald sphere representation of the (002) Bragg reflection projected onto the (H0L) plane. The Ewald sphere is superimposed on the crystal used in x-ray diffraction. The origin of the reciprocal lattice of crystal is placed on where the incident x-ray intersects the Ewald sphere.

The Ewald sphere graphically represents the scattering geometry for elastic scattering. In the example shown in Fig. 2.1, the sample crystal is orientated so that the (002) reciprocal lattice vector $\vec{G}$ coincides with the scattering wavevector. Here the scattering wavevector is the difference between the out-going and incident wavevectors, $\vec{Q} = \vec{k}_{out} - \vec{k}_{in}$. Based on the geometric arrangement of different vectors, the magnitude of the reciprocal lattice vector is $\left|\vec{G}\right| = \frac{2\pi}{d_{(002)}} = \left|\vec{Q}\right| = \frac{4\pi \sin\theta}{\lambda}$, which is exactly the Bragg

equation. The x-ray intensity distribution in the vicinity of a reciprocal lattice vector is often mapped out by varying sample orientation and detector position.

In addition to elastic scattering, the Compton effect describes the inelastic scattering where the scattered x-ray loses a fraction of photon energy. The x-ray can also be strongly absorbed when the photon energy is equal to or slightly larger than the binding energy of inner-shell electrons. The absorption provides invaluable electronic, chemical and magnetic information, which are outside the scope of this thesis. Instead, I will briefly discuss the effect of absorption on x-ray scattering in section 2.5.

2.2 Synchrotron Radiation X-ray Light Sources

A wide range of x-ray sources are used for x-ray diffraction and scattering, ranging from laboratory-scale equipment to facilities that exist only at national facilities. These sources can be compared along one set of key parameters using a quantity called brilliance, defined as the intensity of an x-ray beam normalized by the size and angular divergence of the source and the energy bandwidth. Laboratory x-ray tubes use the elemental characteristic radiation and bremsstrahlung radiation of a metal target (normally copper) impinged by high-energy electrons. The brilliance of laboratory x-ray source is limited by the large 4π solid angle of emitted photons, the low efficiency of the conversion of electrical energy to x-rays, and a large photon energy bandwidth. Because of the large solid angle of emission and large energy bandwidth, only a small fraction of emitted x-ray photons are collected and monochromatized for scattering measurements.

Synchrotron radiation provides x-rays with orders of magnitude higher brilliance than laboratory x-ray sources. Synchrotron radiation is the light emitted by charged

particles travelling in circular orbits [2]. In third-generation synchrotron radiation facilities, such as the Advanced Photon Source (APS) at Argonne National Laboratory, electrons are accelerated to relativistic speed in two stages, consisting of a linear accelerator and a booster synchrotron, before being injected into a storage ring. The storage ring at the APS consists of 40 straight sections, connected with bending magnets. In addition to bending the trajectory of electrons into a circular orbit, the bending magnets also emit a wide spectrum of photons that are spatially confined within a cone along the direction of the instantaneous velocity of electrons. The radiation reaches x-ray-wavelength regime, as a result of the apparent acceleration of electrons boosted by the doppler effect [3].

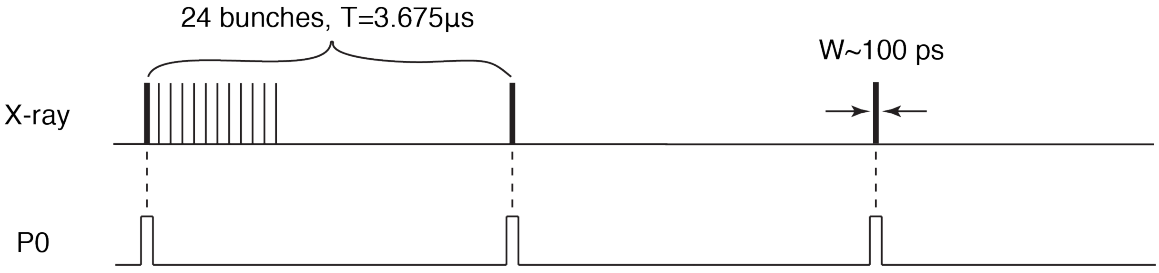

Figure 2.2 Schematics of x-ray bunches and the corresponding electronic signal, P0, in the 24-bunch mode at APS.

X-rays can be produced with far higher brilliance than is possible from bending magnet sources by introducing insertion devices in the straight sections. The key idea of the insertion devices is to use an array of alternating magnets to force an oscillation of travelling electrons. In a wiggler insertion device, the radiation from each oscillation of the electrons is added up incoherently with the following oscillations. In comparison, an undulator is designed so that all the oscillations from one electron are in phase. The coherence addition of oscillations leads to a more monochromic emission spectrum and a reduction of the opening angle of the radiation [3]. At a result, the undulator has the far

higher brilliance than wigglers and bending magnets. All of the x-ray measurements that will be discussed in the following chapters take advantage of the high-brilliance radiation from undulators.

The electrons in the storage ring are grouped into bunches to allow radio frequency cavities to reaccelerate the beam, compensating for the energy lost to radiation. A side effect of the grouping of the charge into bunches is that the radiation from storage rings is emitted in a precise timing sequence. At the APS the full-width at half maximum of bunch duration is approximately 100 ps in the most common operating mode. This x-ray bunch duration in turn sets the limit of the temporal resolution of pump-probe time-resolved diffraction and scattering experiments.

In more detail, the time structure of the x-ray radiation depends on the mode in which the storage ring is operated. At the APS, there are 1296 evenly separated electron buckets. In the 24-bunch mode that is used in our experiments, only 24 buckets spaced by 153 ns are filled [4] (Fig 2.2). The storage ring provides an electronic clock signal P0 with a fixed phase delay to the x-ray pulses and with a period of 3.675 μs, corresponding to the period of the electrons travelling around the entire ring. This P0 signal provides essentially a master clock to synchronize x-ray pulses to other signals including electric fields and laser pulses.

2.3 Microdiffraction and Focusing Optics

The high brilliance x-ray beams provided by synchrotron radiation facilities make it possible to focus x-rays to sub-micrometer spot size while maintain high fluxes and relatively small angular divergences. A spatial resolution of 30 nm, for example, has been

achieved at APS [5]. The availability of intense tightly focused beams greatly improves the spatial resolution of x-ray scattering experiments. As a result, x-ray microdiffraction has been widely used to probe the local structure of functional materials [6, 7]. In our experiments, a sub-micron x-ray beam is important in order to separately probe the regions of ferroelectric materials under external excitation. This section discusses the most important experimental aspect of x-ray microdiffraction: focusing the incident x-ray beam.

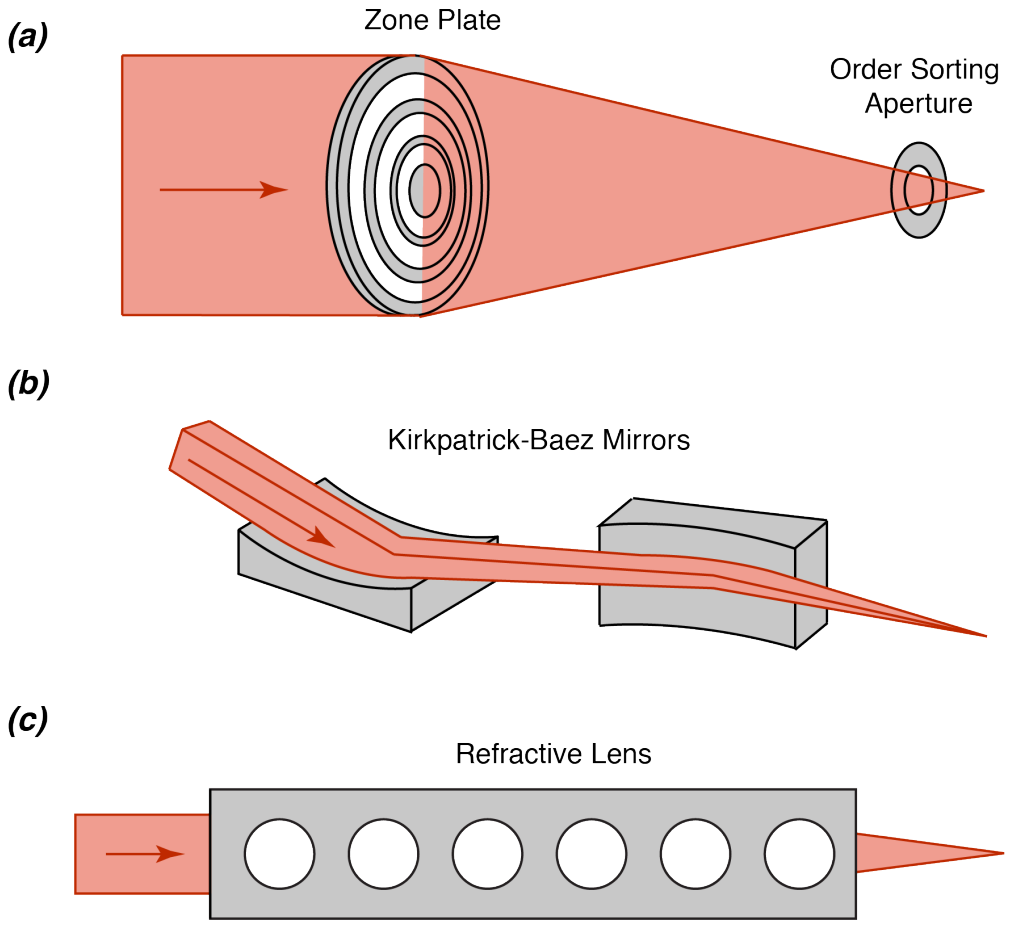

Figure 2.3 Schematics of x-ray focusing optics: (a) Fresnel zone plate, (b) Kirkpatrick-Baez mirrors and (c) compound refractive lens.

Fresnel zone plates [8] are the main focusing optics used in our structural studies of ferroelectric thin films. The zone plate is a circular pattern consisting of a set of

concentric zones defined lithographically, as schematically shown in Fig. 2.3(a). The spacing and size of zones are designed so that the x-rays scattered from each zone interfere constructively at the focal point. The first-order focal length f depends on the x-ray wavelength [9],

$$f = \frac{4N\Delta r_N^2}{\lambda}. \tag{2.2}$$

Here N is the total number of zones and Δr_N is the size of the outmost zone. Additional optics, including a center stop and an order sorting aperture (as in Fig. 2.3(a)) are used to prevent the unfocused x-rays and x-rays focused to higher-order focal points from reaching the sample. The zone plate used in our experiments (Xradia, Inc.) focuses x-rays to a 100 nm spot size, with a focusing efficiency of 10% at a photon energy of 10 keV.

A number of other means have been developed for x-ray focusing. Reflective x-ray optics can be efficiently used in the hard x-ray regime because the refractive index of materials in the x-ray range of photon energies is slightly less than unity. As a result, a total external reflection occurs at an incident angle below a critical value on the order of 0.1°. Kirkpatrick-Baez mirrors [10] are a pair of curved mirrors taking advantage of the effect of the total external reflection to focus the x-rays in two orthogonal directions (Fig. 2.3(b)). X-rays can also be focused using refraction. In compound refractive lenses, shown in Fig. 2.3(c), a series of converging x-ray lens are created by patterning a set of holes in low-atomic-number materials [11].

2.4 Time-Resolved X-ray Diffraction Techniques

Time-resolved x-ray techniques allow us to measure the transient structure of complex oxide thin films in response to electrical or optical excitation. Time resolved

techniques have been developed and continuously improved in our group [12]. This section focuses on the experimental techniques of time-resolved x-ray microdiffraction studies of materials in applied electric fields. Similar principles can be applied to the optical excitation.

The experimental arrangement for time-resolved x-ray measurements is schematically shown in Fig. 2.4. The ferroelectric oxide thin films we have studied were deposited on top of a continuous bottom electrode. Top electrodes with a diameters ranging from 20 to 100 μm were patterned on the surface of thin films to form ferroelectric capacitors. The incident x-ray beam was focused to the center of the ferroelectric capacitors using the focusing optics mentioned in section 2.3.

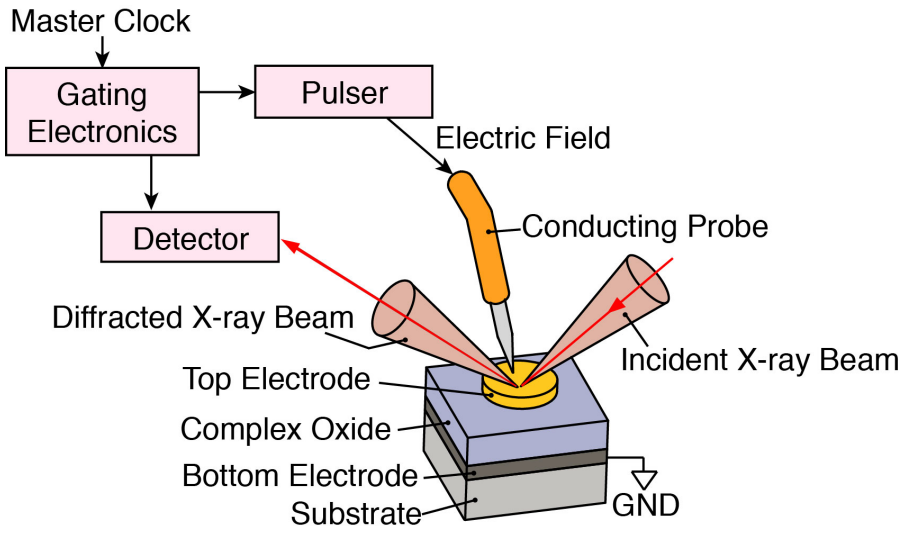

Figure 2.4 Eexperimental setup for time-revolved x-ray microdiffraction with applied electric fields.

During the application of electric fields, the bottom electrode was grounded by connecting it to the shell of a coaxial cable, and the top electrode was contacted by a probe tip manipulated by a three-axis translation stage. The electronic pulse generator

(Picosecond Pulse Generator, Model 2600) has the capability to apply electrical pulses with duration of 2-300 ns and amplitude up to 45 V. Electronic excitation was synchronized to x-ray pulses using the strategy described in the next paragraph. The x-ray detector consisted of either an avalanched photodiode or a pixel-array two-dimensional detector. Electronic signals associated the detection of a particular x-ray bunch can be selectively gated and separately recorded. By varying the time delay between electric excitation and the selected x-ray pulses, we can probe the transient structure at different stages after the application of an electric field.

The process of synchronizing the applied electrical pulses to the x-ray beam is illustrated in Fig. 2.5. The electronic clock signal (at APS, the P0 signal) with a fixed phase delay to x-ray pulses sets the overall timebase (Fig. 2.2). An electronic circuit designed in our group, termed the "gate box," took in the P0 signal and generated a set number of gate pulses. The overall process was triggered by the data acquisition software, either spec (Certified Software, Inc.) or the EPICS data acquisition system used at the APS. The repetition rate of the pulses generated by the gate box can be controlled by dividing the repetition rate of the input master clock P0. We often used a repetition rate of 10 kHz, which results from a compromise between the recovery rate of the ferroelectric sample after electrical cycling (favoring low repetition rates) and the period of time required to complete the experiment (favoring high rates).

Gate pulses were delayed using a delay generator and sent to two different destinations. One copy of the delayed gate pulses was used to gate the x-ray detector. The second copy of the gate signal was further processed because the gate pulses directly from the gate box can have large temporal jitter and thus are not suitable for high-

precision time-resolved measurements. The jitter arises from the digital design of the gate box. An AND logic circuit was developed to produce a set of electric pulses with reduced time jitter, by resynchronizing the output of the gate box with the P0 signal. This gated P0 was further delayed with a second delay generator and sent to trigger the final electric pulse generator exciting the sample. The delay to the final electric pulser was used as the variable in our time-resolved measurement.

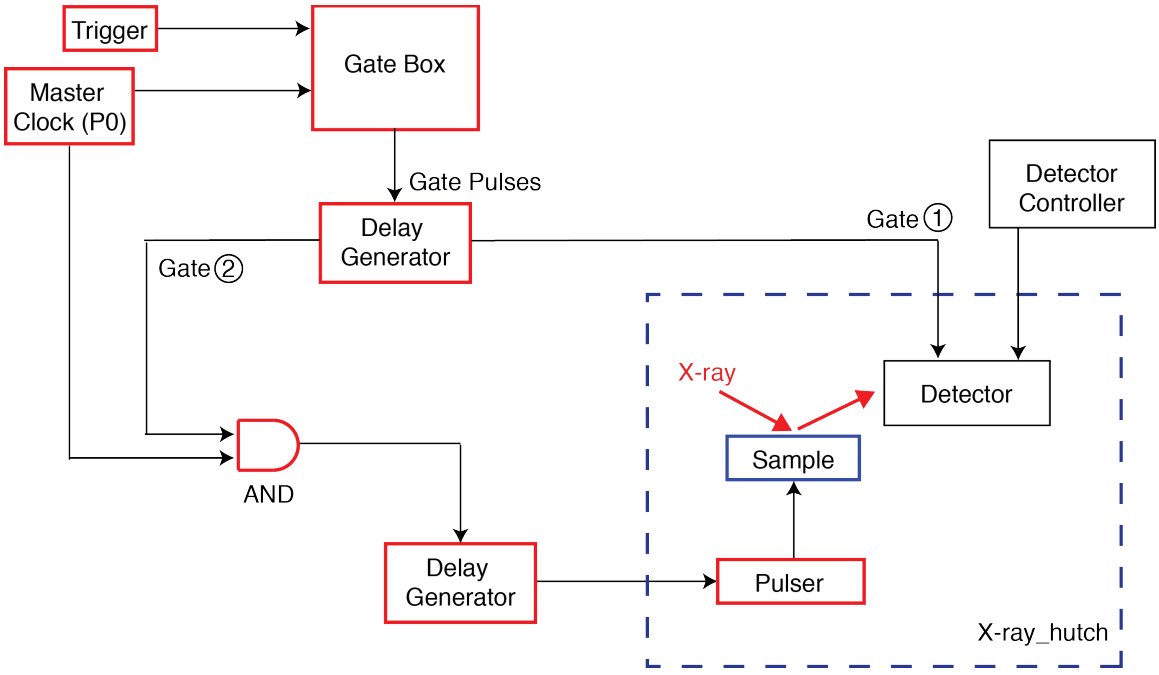

Figure 2.5 Gating electronics to synchronize the applied electric fields to x-ray pulses.

The repetition rate of electric excitation pulses was around 10 kHz, two orders of magnitude smaller than the repetition rate of x-ray pulses. As a consequence, the time-resolved scheme described here utilized only 1% of the total flux. A diffraction pattern is often accumulated over hundreds of thousands of gated x-ray signals in order to achieve a reasonable counting statistics.

The temporal resolution of the time-resolved diffraction and scattering measurements is limited by a series of factors. Besides the 100-ps width of x-ray pulses, electronic jitter, the finite rise time of electric excitation pulses and the charging time of ferroelectric capacitors all limit the effective temporal resolution of our experiments. In most samples the charging time of capacitors is the dominant factor, with time constants that range from 1 to 100 ns depending on the system. The charging time can be reduced by using small top electrodes with a diameter down to 10 μm and low-sheet-resistance bottom electrodes. When electrical excitation can be avoided altogether, as for the optical excitation experiments described in Chapter 6, the limitation imposed by sample charging is lifted and a temporal resolution of 100 ps is achieved.

2.5 Kinematic X-ray Diffraction Simulation

Kinematic x-ray diffraction refers to the strategies that can be used to compute the diffraction pattern of a crystal in the weak-scattering limit where multiple scattering can be neglected. This approximation is generally applicable experimentally except for highly perfect crystals with a number of planes approaching the extinction length, several hundred nm for the materials discussed in this thesis. The simulation of diffraction patterns within the kinematic approximation provides a valuable way to interpret x-ray structural measurements. These interpretations are discussed in detail in Chapter 4 and Chapter 6. The basic formulas of the intensity calculation of kinematic x-ray scattering [13] are given in this section.

The x-ray scattering intensity is proportional to the square of the structure factor of the crystal illuminated by the x-ray beams,

$$I \propto \left| F^{crystal}(\vec{Q},E) \right|^2 , \tag{2.3}$$

where the structure factor of the crystal is $F^{crystal}(\vec{Q},E)$, which is a function of the scattering wavevector $\vec{Q}$ and x-ray photon energy *E*. The structure factor of the crystal is the product of two terms:

$$F^{crystal}(\vec{Q},E) = \sum_n f_n(\vec{Q},E) e^{i\vec{Q}\cdot\vec{r}_n} \sum_m e^{i\vec{Q}\cdot\vec{R}_m} , \tag{2.4}$$

where *f*, *r* and *R* are the atomic scattering factor, atomic position with respect to a particular lattice site and the coordinate describing the periodic lattice.

The factor given by the first sum on the right hand side of Eq. (2.4) is the structure factor of the repeating unit, termed the unit cell structure factor. The structure factor of the unit cell gives the envelope of the distribution of scattered x-ray intensity. The repeating unit is usually is a unit cell for a crystal, but can also be extended to a much larger cell such as the polarization domain or the superlattice repeating unit.

The second sum on the right hand side of Eq. (2.4) is the lattice sum, which determines the position and width of the Bragg reflections. When the crystal dimension is reduced, such as in thin films or nanoscale islands, the lattice sum also leads to intensity fringes adjacent to Bragg reflections.

Besides being scattered, x-ray can also be absorbed in interaction with atoms. Absorption modifies the atomic scattering factor by introducing dispersion correction terms f_1 and f_2 [14]:

$$f(\vec{Q},E) = f_0(\vec{Q}) + f_1(E) + if_2(E) . \tag{2.5}$$

The dispersion correction is the origin of the energy dependence of the atomic scattering factor, and is particularly important at photon energy near absorption edges. The f_0 term can be approximated by the Fourier transform of the electron density as in

$$f_0(\vec{Q}) = \int \rho(\vec{r}) e^{i\vec{Q}\cdot\vec{r}}\, d\vec{r}\,. \tag{2.6}$$

where r is spatial coordinate of electrons. At the forward-scattering limit, with $Q = 0$, the f_0 term is just the atomic number. The values of all the three contributions to the atomic scattering factor are available in tables in the X-ray Oriented Program [15] or in Ref. 14.

2.6 References

[1] B. D. Cullity, and S. R. Stock, "*Elements of X-ray Diffraction*" (Prentice Hall, 2001).

[2] L. G. Parratt, "*Use of Synchrotron Orbit-Radiation in X-Ray Physics,*" Rev. Sci. Instrum. **30**, 297 (1959).

[3] J. Als-Nielsen, and D. McMorrow, "*Elements of Modern X-ray Physics*" (Wiley, 2011).

[4] Advanced Photon Source storage ring operation modes, http://www.aps.anl.gov/Accelerator_Systems_Division/Accelerator_Operations_Physics/SRparameters/node5.html

[5] X-ray Microscopy Capabilities, http://nano.anl.gov/facilities/xray_cap.html

[6] J. Y. Jo *et al.*, "*Structural Consequences of Ferroelectric Nanolithography,*" Nano Lett. **11**, 3080 (2011).

[7] D. H. Do *et al.*, "*Structural Visualization of Polarization Fatigue in Epitaxial Ferroelectric Oxide Devices,*" Nature Mater. **3**, 365 (2004).

[8] E. Di Fabrizio *et al.*, "*High-efficiency Multilevel Zone Plates for keV X-rays,*" Nature **401**, 895 (1999).

[9] J. Kirz, and D. Vaughan, "*X-ray Data Booklet*" (Lawrence Berkeley Laboratory, University of California, 1985).

[10] W. Liu *et al.*, "*Short Focal Length Kirkpatrick-Baez Mirrors for a Hard X-ray Nanoprobe,*" Rev. Sci. Instrum. **76**, 113701 (2005).

[11] A. Snigirev, V. Kohn, I. Snigireva, and B. Lengeler, "*A Compound Refractive Lens for Focusing High-energy X-rays,"* Nature **384**, 49 (1996).

[12] A. Grigoriev *et al.*, "*Synchronizing Fast Electrically Driven Phenomena with Synchrotron X-ray Probes,"* Rev. Sci. Instrum. **78**, 023105 (2007).

[13] B. E. Warren, "*X-Ray Diffraction"* (Dover Publications, 1969).

[14] C. T. Chantler, "*Theoretical Form Factor, Attenuation, and Scattering Tabulation for Z=1–92 from E=1–10 eV to E=0.4–1.0 MeV,"* J. Phys. Chem. Ref. Data **24**, 71 (1995).

[15] X-ray Oriented Program, http://www.esrf.eu/computing/scientific/xop2.1/

3 Nanosecond Transformation of Polarization Stripe Domains in Ferroelectric/Dielectric Superlattices

3.1 Introduction

Ferroelectric/dielectric superlattices have electronic and structural properties that are not available in compositionally uniform ferroelectrics [1-3]. These properties can be tuned with additional degrees of freedom provided by the interfacial coupling in the superlattice structure. Methods include varying the composition and relative thickness of ferroelectric and dielectric layers [4, 5]. This chapter focuses on the nanoscale stripe domains recently discovered in ferroelectric/dielectric superlattices [6-8]. The stripe domains reflect the energy landscape of the superlattice. The phenomena associated with the stripe domains are the key to understanding the coupling of ferroelectric polarization, crystallographic structure and elastic distortion at the interfaces of superlattice components.

The stripe domains in superlattices are macroscopically have a similar geometry to the stripe domains observed in ultrathin ferroelectric films [9-11], but have a different origin and more complex atomic-scale structure. As described in Chapter 1, the formation of the stripe domain pattern is driven by the competition of the electrostatic energy associated with the depolarization field and the energy of creating domain walls. In ferroelectric/dielectric superlattices, it is the non-uniform polarization profile between ferroelectric and dielectric components that has the key role in defining the depolarization field [12], rather than the film/air or film/substrate interfaces as in the ultrathin-film ferroelectric case [13]. A large fraction of the polarization is confined in ferroelectric

layers; it is this polarization that forms the stripe domains. Atomic-scale structural changes are also expected to accompany the complex polarization distribution of the stripe domains [12]. The effect of this structural variation on the dynamics of domains will be discussed in detail in Chapter 4. The static structure of stripe domains has been extensively studied [6, 14]. The stripe domains are unstable in applied electric fields and eventually transform into a uniform polarization domain state. The associated dynamics, however, has not yet been probed with a sufficient temporal resolution.

From their observations in a quasi-steady-state study based on a long-timescale measurement, Zukbo *et al.* proposed that the switching process is governed by the continuous motion of domain walls. In this picture, the volume fraction of polarization domains that are favored under applied electric fields increases continuously by the continuous displacement of each domain wall into the adjoining stripe domains [6]. In addition to this proposal, theoretical calculations have provided a range of predictions, including the formation of polarization bubbles and a difference in the stabilities of the domains in ferroelectric and dielectric layers [7]. To capture the precise nature of the transition of stripe domains, the dynamics of stripe domains must be probed with nanosecond timescale experiments that match the switching timescale.

This chapter describes an experimental study of the dynamics of the transition from stripe domains to a single uniform-polarization domain state [15]. There are two key results. First, time-resolved x-ray scattering shows that there is no piezoelectric expansion in the area of the superlattice in which the stripe domain persists after the application of the electric field. The overall superlattice after switching does, however, exhibit piezoelectricity. Based on this observation, we propose a heterogeneous switching

model that the polarization switching proceeds by eliminating stripe domains to form regions of uniform polarization, which subsequently grow across the extent of the sample. A second key result is that the timescale of the polarization switching depends on the magnitude of the applied electric field and can be as fast as a few nanoseconds at high fields.

3.2 Experimental Arrangement

A $PbTiO_3/SrTiO_3$ superlattice with well-defined stripe domains was chosen for this dynamics study. The superlattice has a repeating unit consisting of 12 unit cells of $PbTiO_3$ and 3 unit cells of $SrTiO_3$ and a total thickness of 100 nm. The superlattice was grown by Prof. Matthew Dawber's group at Stony Brook University [4]. The superlattice was deposited using off-axis radio frequency magnetron sputtering on a 20-nm-thick $SrRuO_3$ continuous bottom electrode layer on a (001)-oriented $SrTiO_3$ substrate. Au top electrodes with a diameter of 50 μm were patterned on top of the superlattice through shadow masks, forming an array of superlattice thin film capacitors.

The tetragonality of the $PbTiO_3$ layer forced the ferroelectric polarization to be either parallel or antiparallel to the superlattice surface normal. The bottom electrode was grounded and voltage pulses were applied to the top electrode through a conducting probe tip. As a result, the application of positive electric fields favors the growth of polarization-down domains.

Measurements of time-resolved structure of the superlattice were conducted at station 7ID-B at the Advanced Photon Source at Argonne National Laboratory. The experimental details of the time-resolved x-ray microdiffraction study were introduced in

Chapter 2. The 10 keV x-ray beam was focused to a spot size of 200 nm near the center of the superlattice capacitors using a Fresnel zone plate. The diffracted x-rays were detected using a pixel-array area detector [16], which allows diffraction patterns to be acquired over a two-dimensional sheet in reciprocal space. During the dynamics study, a set of 150-ns-duration electric pulses was applied at a repetition rate of 18 kHz. To measure the transient structure, a set of electric pulses at the same repetition rate of applied electric fields was used to externally gate the detector, and select a particular x-ray bunch. Diffraction patterns were accumulated over millions of cycles of electric pulses to reach a reasonable counting statistics.

3.3 Static Structure of the $PbTiO_3$/$SrTiO_3$ Superlattice

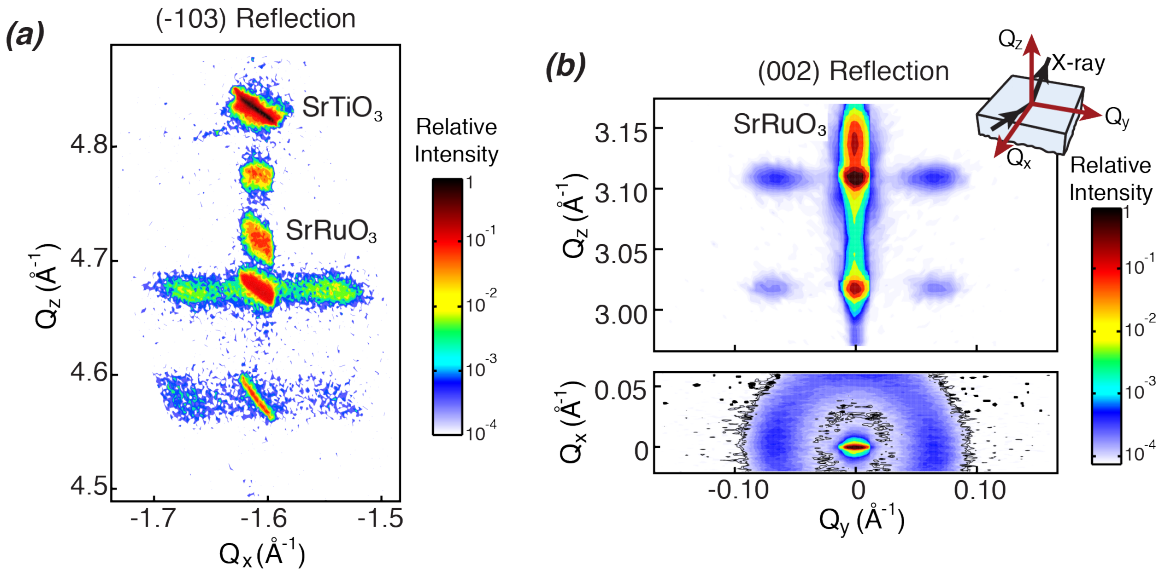

Figure 3.1 (a) Reciprocal space map at $Q_y = 0$ near the (-103) Bragg reflection. (b) Reciprocal space maps at $Q_x = 0$ (top) and $Q_z = 3.106$ Å^{-1} (bottom) near the (002) Bragg reflection. Reflections from the $SrTiO_3$ substrate and $SrRuO_3$ bottom electrode are labeled next to the peaks. The map in (a) was acquired using a laboratory x-ray diffractometer with a 1/16° detector slit, resulting in the anisotropic broadening of the Bragg reflections. The maps in (b) were acquired using synchrotron x-ray diffraction with zone plate optics. Reflections from the stripe nanodomains appear at non-zero values of Q_x and Q_y in (a) and (b) and form a ring in the Q_x-Q_y plane in the bottom panel of (b). The insert shows a schematic of the scattering geometry.

The static structure of the superlattice was inferred from a series of reciprocal space maps. Maps of the intensity of x-rays scattered near (-103) and (002) Bragg reflections are shown in different planar sections in reciprocal space in Fig. 3.1. Besides the Bragg reflections arising from the $SrTiO_3$ substrate and $SrRuO_3$ bottom electrode, a rich set of reflections can be assigned to the $PbTiO_3$/ $SrTiO_3$ superlattice. The in-plane wavevector Q_x of superlattice structural reflections follows the value set by the $SrTiO_3$ substrate, as shown in Fig. 3.1(a), a result of the coherent epitaxial growth of the superlattice thin film. The intense reflections at $Q_z = 4.66$ Å^{-1} in Fig 3.1(a) and $Q_z = 3.106$ Å^{-1} in Fig 3.1(b) arise from the average out-of-plane lattice spacing of the entire superlattice, 4.046 Å. The periodicity of the repeating unit further results in satellite reflections along Q_z. The structural reflections of the superlattice, including Bragg peaks and satellites, occur at values of Q_z given by $Q_z = \frac{2\pi}{d_{avg}}(m + \frac{l}{n})$, where m and l are reflections indices, d_{avg} is the average lattice constant of each unit cell, and n is the total number of atomic layers in one repeating unit.

The in-plane stripe domains produce weak x-ray diffuse scattering peaks with offset from the structural superlattice reflections in Q_x and Q_y. The intensity of the domain satellite is three orders of magnitude weaker than the corresponding superlattice structural reflection. In both the (-103) and (002) reciprocal space maps shown in Fig. 3.1, the domain satellites have an in-plane component deviate from the structural reflections by ΔQ_x or $\Delta Q_y = 0.066$ Å^{-1}, corresponding to a domain period of 9.5 nm. In the Q_x-Q_y plane shown in Fig. 3.1(b), the domain satellite forms a ring with a constant radius around the superlattice reflection. The azimuthal variation of intensity of the

domain diffuse scattering is plotted in Fig. 3.2(c). The intensity is maximized along [100] and [010] directions around the ring pattern, approximately a factor of two larger than the intensity along the [110] direction. We thus conclude that the stripe domains are populated with a slightly preferred orientation along <100>.

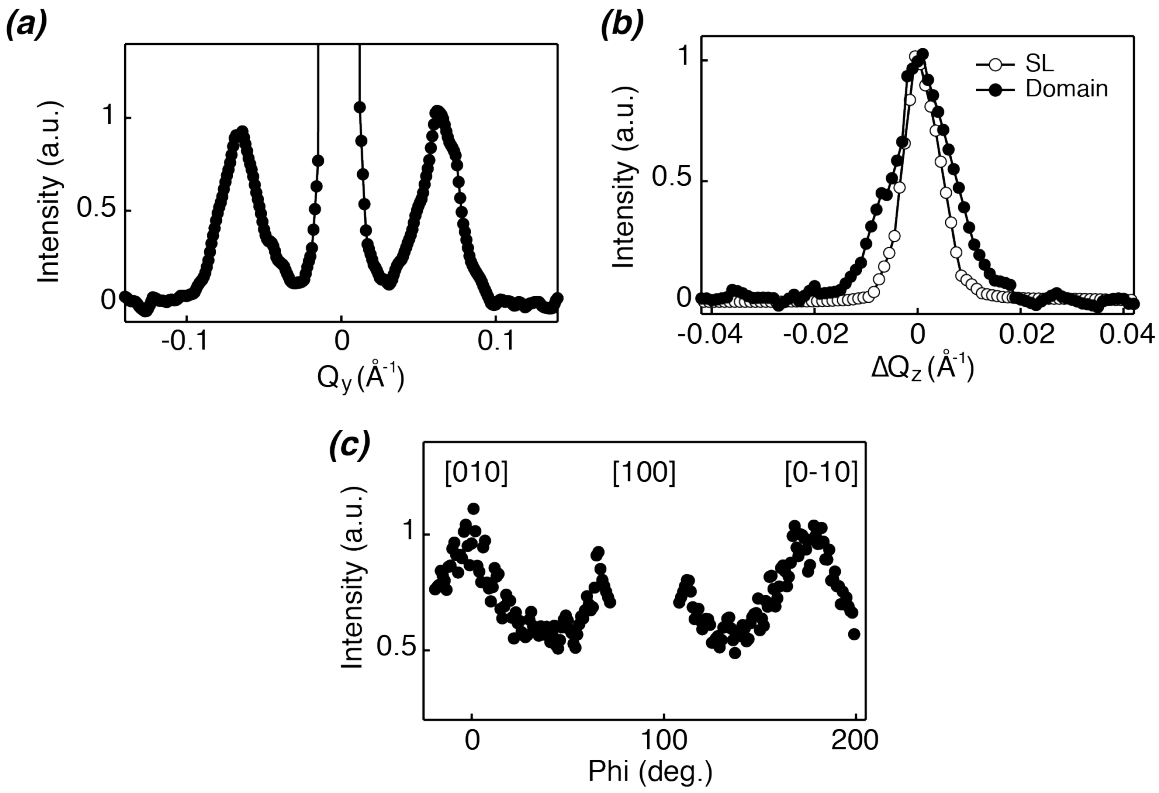

Figure 3.2 (a) Line profile of the normalized intensity of domain satellites across Q_z = 3.106 Å^{-1}. The central intense peak is the superlattice structural reflection. (b) Comparison of the out-of-plane peak width of the l = 0 domain satellite and l = -1 superlattice structural reflection. The l = 0 superlattice structural reflection is not used due to artificial broadening caused by the saturation of the detector. The horizontal axis is shown as the deviation of Q_z from the peak position. (c) Normalized intensity of domain satellite as a function of the azimuthal angle (phi) along the (00L) rod. These line profiles are extracted from Fig. 3.1(b).

We can also extract the coherence length of stripe domains from the domain diffuse scattering patterns. The coherence length L is inversely proportional to the peak width W of domain satellites, as in

$$L = \frac{1.76\pi}{W}. \tag{3.1}$$

This equation is derived by Fourier transforming an object with a finite length L and computing the full width at half maximum (FWHM) of the reciprocal-space central peak. Fig. 3.2(a) and (b) show line profiles of domain satellites along Q_y and Q_z directions, respectively. The FWHM is 0.0323 $Å^{-1}$ along Q_y and 0.0147 $Å^{-1}$ along Q_z. In comparison, superlattice structural reflection has width of 0.0087 $Å^{-1}$. This value of 0.0087 $Å^{-1}$, however, underestimates the out-of-plane coherence length of the superlattice, which is expected to be the thickness of 100 nm. The discrepancy is in part caused by the measurement resolution limited by factors including the 0.14° convergent angle of the incident x-ray. The same measurement resolution can be applied to the domain satellites.

We estimate that the in-plane coherence length of stripe domain is 17.5 nm, about two domain periods. Together with the ring-like diffraction pattern, we can deduce that the stripe domain pattern exhibits a high degree of orientational disorder and that the real space in-plane configuration of stripe domain resembles the labyrinth domain pattern found in ferromagnetic thin films [17]. The out-of-plane coherence length is 42 nm, equivalent to 7 superlattice repeating units. A coherent length equal to film thickness is expected for the case where the domain walls are aligned between $PbTiO_3$ and $SrTiO_3$ components. The short out-of-plane coherence length measured here can be a result of the roughness of domain walls that effectively decouples the domain and reduces the coherence length.

3.4 Partially Switched State of the $PbTiO_3/SrTiO_3$ Superlattice

The transient structure of the superlattice was probed by acquiring a series of x-ray diffraction patterns at different times after the beginning of the electric field pulse. Fig. 3.3(a) shows the evolution of both the superlattice (002) structural Bragg reflection

and $SrRuO_3$ Bragg reflections during the application of 84 MV/m electric-field pulses. The peak position of the $SrRuO_3$ Bragg reflection was constant over the entire duration of the applied fields. On the contrary, the superlattice structural refection shifted to smaller Q_z as a result of piezoelectric expansion. The expansion occurred over a time of approximately 100 ns at this field magnitude. This characteristic timescale depends on both the transformation of the domains and on the RC time constant for the charging of the superlattice capacitor.

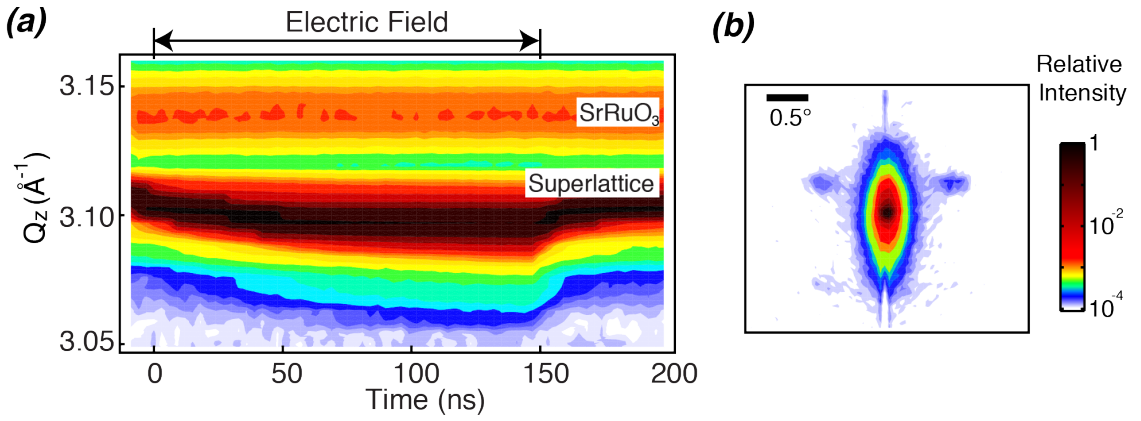

Figure 3.3 (a) Evolution of the superlattice and $SrRuO_3$ (002) Bragg reflections as a function of time under a 150-ns, 84 MV/m electric pulse. (b) Diffraction pattern in an applied electric field of 106 MV/m with the diffractometer optimized for the superlattice reflection at Q_z = 3.085 Å^{-1}. The projection of the Q_z axis onto this diffraction pattern is along the vertical axis of the figure.

The stripe domains and the corresponding x-ray domain satellites are expected to disappear during the field-driven transformation to a uniform-polarization state. Fig. 3.3(b) shows a diffraction pattern acquired in a partially transformed state where the domain satellites were still present together with the superlattice reflection. In contrast to the shift of the superlattice structural reflection, the domain satellites have a negligible change in their Q_z wavevectors, indicating a strong suppression of the piezoelectric effect in the stripe domains.

The suppression of the piezoelectric effect only occurs in the stripe domain. This puzzle – of how a polarized ferroelectric material in a large electric field can exhibit no piezoelectric distortion – can be solved by considering the role of mechanical clamping in the electromechanical properties of the domains. In the absence of clamping effects, domains with opposite polarizations have different signs of piezoelectric distortion. In a nanometer scale domain pattern, however, the alternating sign of the strain would result in large and energetically unfavorable discontinuities of the lattice structure at each domain wall. The energy of this configuration has been calculated for similar domains in ref. [18]. The additional constraint imposed by the domain pattern thus results in a suppression of the piezoelectric distortion is expected in nanoscale domains. The system can avoid large elastic energy associated with the discontinuity of the lattice near domain walls.

The changes in the stripe domain pattern induced by the applied electric fields can be studied by examining the field-induced changes of the wavevectors of the domain diffuse scattering satellites. Fig. 3.4(a) shows peak positions along Q_z and Q_y directions as a function of time after the beginning of the electric field pulse. The value of Q_z changed by less than 0.001 $Å^{-1}$ for both 38 MV/m and 84 MV/m electric field pulses, a factor of five smaller than the shift of the superlattice structural reflection. This result shows that piezoelectricity was strongly suppressed regardless the magnitude of the electric field. The values of Q_y of the domain satellites also remain constant under in applied electric fields. The lack of the variation in the in-plane domain period is consistent with the observation in Zukbo *et al.* that the domain period does not change under electric fields [6]. The constant period has a straightforward explanation: it is

geometrically difficult to add or remove stripes from the overall pattern. Changing the domain period would require a collective transformation of stripe domains over a macroscopic area and therefore did not occur in our experimental conditions.

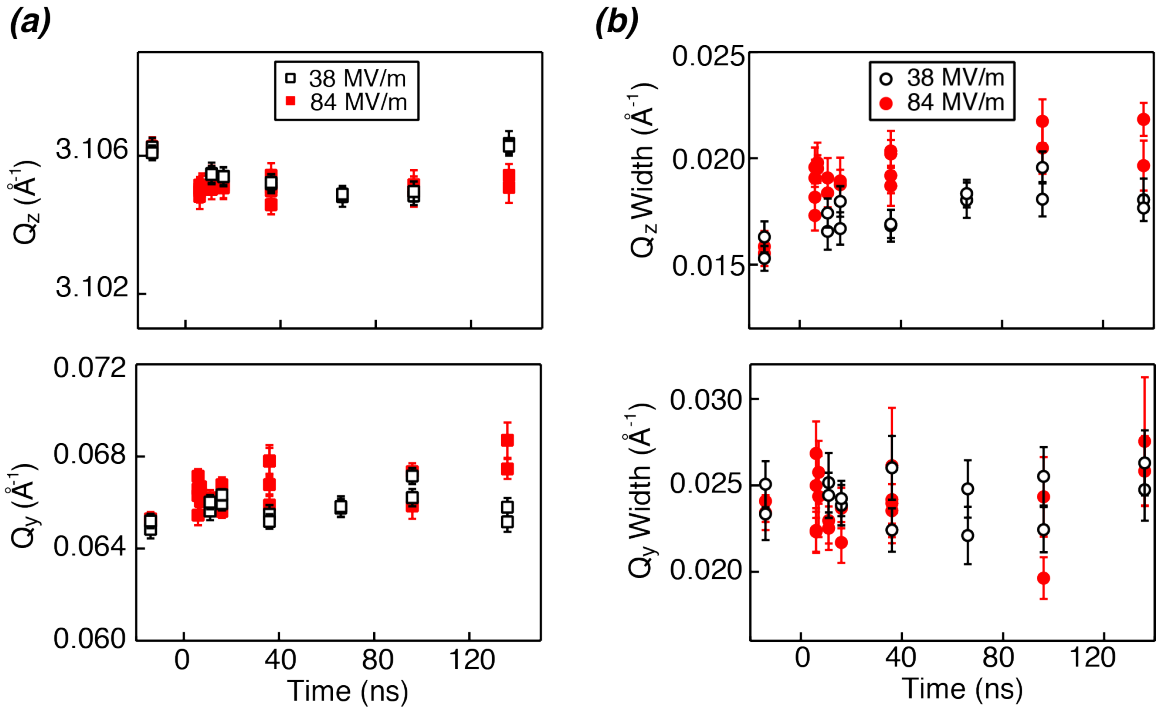

Figure 3.4 Values of (a) Q_z and Q_y of the domain satellite as a function of time during applied electric fields of 38 MV/m (open squares) and 84 MV/m (filled squares). Peak widths of the domain satellites along (b) Q_z and Q_y as a function of time during applied electric fields of 38 MV/m and 84 MV/m. The pulse duration is 150 ns. The standard deviation in the Gaussian peak fitting is used as the error bar.

The change of the coherence length of the domain pattern can be investigated by examining the field-induced changes in the widths of domain satellites. The electric-field-induced evolution of the peak width is shown in Fig. 3.4(b) under both 38 MV/m and 84 MV/m electric field pulses. Note here that the zero-field peak width is slightly different from the width estimated in Fig. 3.2, indicating a spatial variation of the coherence length across the superlattice sample. The peak width along Q_z increases gradually under electric pulses, with larger change under higher electric fields. At 84 MV/m, the peak width

increases to 0.022 $Å^{-1}$, corresponding to an average coherence length of 26 nm. The in-plane peak width along Q_y, on the other hand, shows no systematic change under electric fields. We did, however, observe a decreasing trend of the in-plane width in another superlattice capacitor under similar experimental conditions. We therefore conclude that stripe domains have a similar or slightly larger degree of in-plane disorder during the transformation into a single domain state.

3.5 Heterogeneous Transformation Model

We propose a heterogeneous transformation model to describe the polarization transformation from the stripe domains state to the uniform electric field in an applied electric field. The puzzling observation described in the previous section was that stripe domains and the overall superlattice show very different piezoelectric responses in the same electric field. The key features of the model we propose are illustrated in Fig. 3.5. With this model we can resolve the puzzle.

We propose a model in which different regions of stripe domains transform heterogeneously across the areas under applied electric fields. During the transition, the regions that are already transformed are sufficiently large so that they are free from the mechanical clamping effect limiting the piezoelectricity. The regions that are not yet transformed preserve the stripe domain pattern and show negligible piezoelectric expansion. The x-ray footprint is an order of magnitude larger than the domain period and therefore the diffraction patterns can capture the structural response from both the transformed and untransformed regions. The spatial variation of the transformation can result from either surface defects or from random variations in the domain configuration. We hypothesize that both of these effects can locally modify the thermodynamics of the

transformation.

The heterogeneous switching model is different from switching model used to describe the domain dynamics of in compositionally uniform ferroelectrics. Nanosecond switching phenomena in uniformly polarized ferroelectrics are accurately described by models of the nucleation of polarization domains and the subsequent motion of domain walls [19, 20]. These models are not applicable in the case of nanoscale stripe domains, where the polarization domains favored by electric fields have already constituted half of the volume fraction at zero fields and each unflavored domain is only a few nanometers wide.

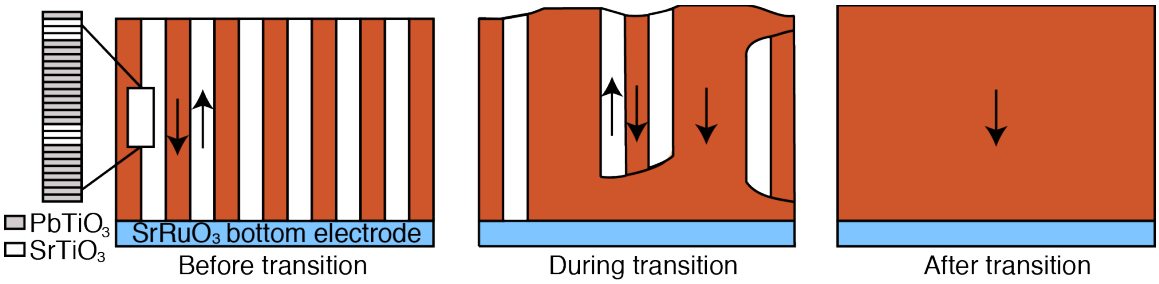

Figure 3.5 Schematic domain patterns according to the proposed heterogeneous switching model. The arrangement of domains is shown before, during, and after the transition from stripe nanodomains to the uniform polarization state. The in-plane coherence length of the stripe pattern is drawn as infinite in order to simplify the representation. The sequence of atomic unit cells in the superlattice is shown as an inset.

Zukbo *et al.* have proposed that the volume fraction of domains favored by electric fields increases via a continuous displacement of domain walls over the course of applied fields [6]. In this continuous displacement model, the domain wall motion is expected to occur simultaneously over the area with electric fields, and as a result the piezoelectric distortion would develop at the same rate in both the domain satellite and the superlattice structural reflection. This expectation is incompatible with our observations that stripe domains show a much smaller piezoelectric distortion in

comparison with the superlattice as a whole.

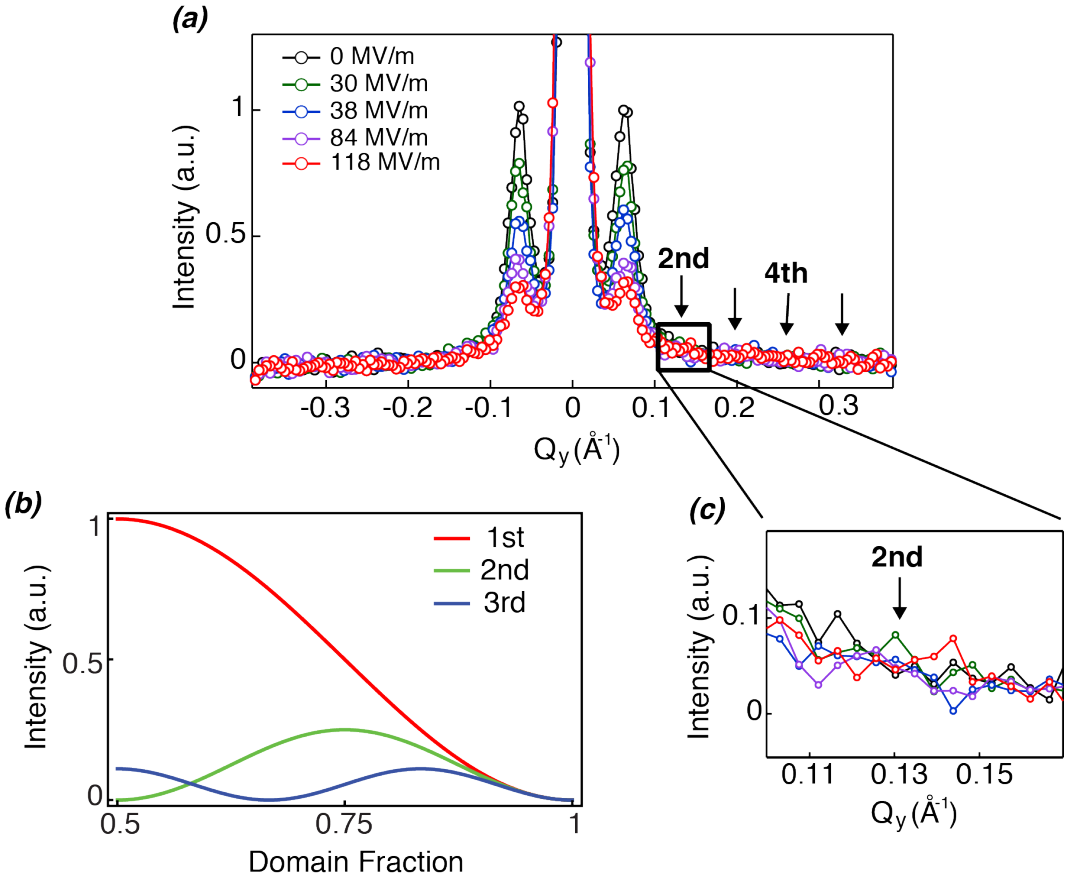

Figure 3.6 (a) Normalized intensity of domains satellites as a function of Q_y at electric fields ranging from zero to 118 MV/m. The expected reciprocal-space positions for higher order domain satellites are marked with arrows. (b) Simulated intensity of domain satellites as a function of domain fraction. (c) Zoomed-in intensity vs. Q_y curves in the area in (a) marked with a square.

In areas where domains are metastable under electric fields, we also found no evidence that the volume fraction of domains is changed within the remaining stripe domains. The x-ray scattering intensity of domain satellites is affected by the arrangement of stripe domains. Assuming an infinite coherence length and that the domain walls are perfectly aligned, the intensity of domain satellites follows the equation

$$I \propto \frac{\sin(kr\pi)^2}{k^2}. \tag{3.2}$$

where r is the domain fraction and k is the order of domain satellites along the in-plane direction [6]. When the superlattice has the equal fraction of polarization-up and down domains, domain satellites with even order k have zero intensity.

Taking into account the short in-plane coherence length observed, we have experimentally searched for higher order domain diffuse scattering satellites, and simulated the evolution of those satellites as in the continuous displacement model. Fig. 3.6(a) shows domain satellites measured under a range of electric fields. A simulation of the change of domain satellites as the domain fraction changes in the continuous displacement model is shown in Fig. 3.6(b). For a domain fraction of 75%, the second-order domain satellite is predicted to have maximum intensity, reaching approximately half of the intensity of the first-order domain diffuse scattering peak.

No intensity maxima are observed at the reciprocal-space position for the expected second-order domain satellites, as illustrated in Fig. 3.6(c). The absence of second-order domain satellites is consistent with $r = 0.5$, equal fractions of the domain structure in each polarization. The field-induced evolution of domain satellites suggests that there is no significant change of the fraction of the stripe domain to the polarization direction favored by the applied electric field. We therefore conclude that the change of domain fraction is not a significant physical process during the transformation of stripe domains.

We also note the absence of domain satellites with third-order or higher, which can be a result of random variations in domain orientation and domain period. These variations smear out the domains satellites, especially the higher-order ones, as have been demonstrated in stripe domains in $PbTiO_3$ thin films [11].

Our results can also be used to test other predictions. Theoretical calculations by Lisenkov *et al.* predict that dielectric layers in superlattice transform earlier than the ferroelectric layers [7]. If the dielectric layers were switched completely while the ferroelectric layers conserve stripe domains, a change in the Q_z of the domain reflection would be expected in order to accommodate the piezoelectric expansion in the dielectric layers. This expansion was not observed in our experiments. We therefore expect a more moderate structural distortion on basis of the stripe domain configuration. The detailed difference in the dynamics between the ferroelectric and dielectric layers, including the domain walls and lattice constant in each superlattice component, will be discussed more extensively in Chapter 4.

3.6 Nanosecond Transformation to the Uniform Polarization State

The time-dependence of the transition from the stripe domain state to the uniform polarization state can be studied using the time-dependence of domain diffuse scattering satellite reflections. Following the heterogeneous transformation model, the intensity of the domain satellite is proportional to the volume of the remaining unswitched stripe domains. Fig. 3.7(a) shows a series of diffraction patterns near one of the domain satellites during an electric field pulse with a magnitude of 84 MV/m. As the time after the onset of the electric field increased, the domain satellite declined.

The characteristic times for the transformation were deduced by analyzing the intensities of the domain diffuse scattering satellites. The integrated intensities of the domain satellites were calculated after removing two sources of background (i) a uniform background intensity and (ii) the tail of the intense superlattice structural reflection. A monotonic decrease of the intensities of the domain satellites was observed under applied

electric fields ranging from 38 to 168 MV/m. The time-evolution of the integrated intensities of the domain satellites are shown in Fig. 3.7(b) for applied electric fields of a series of magnitudes in this range.

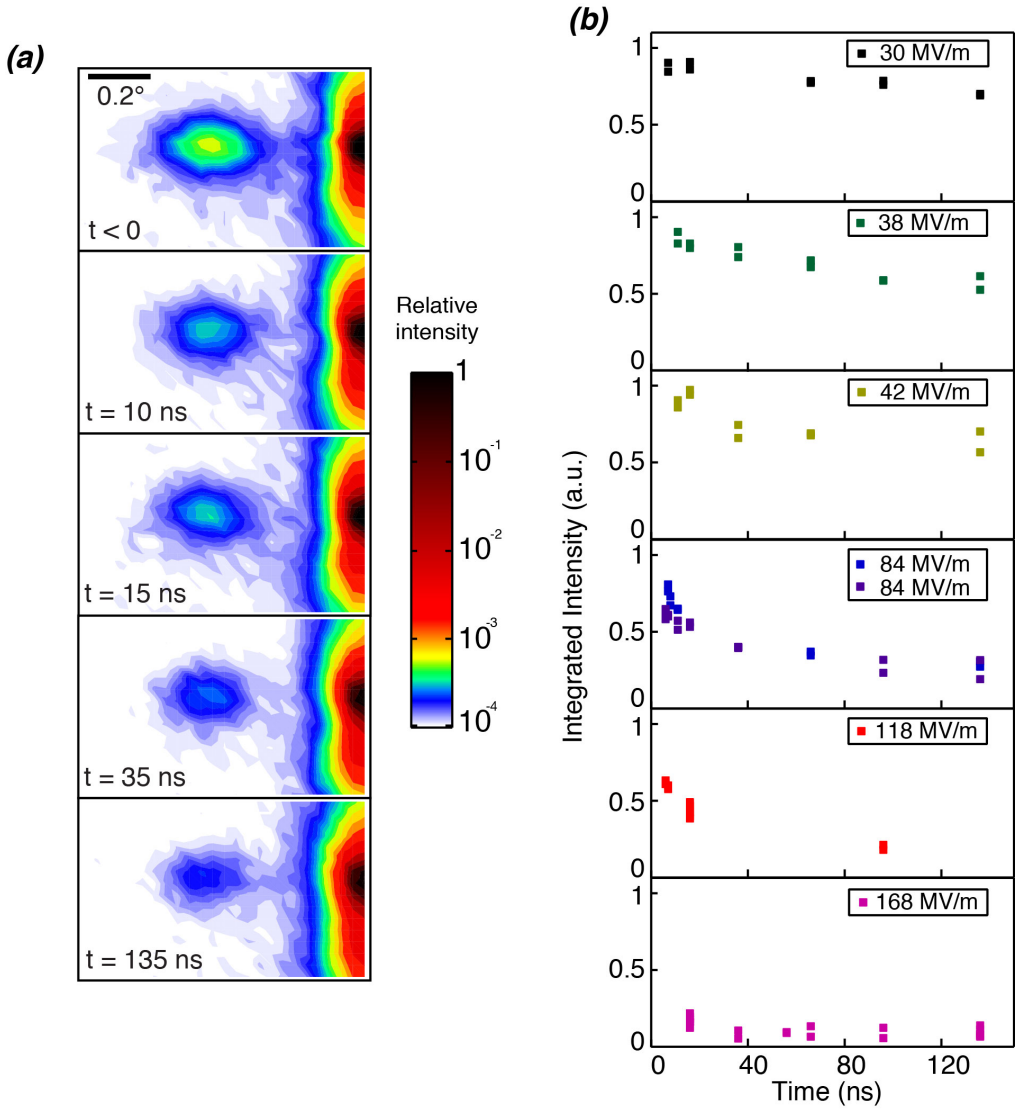

Figure 3.7 (a) Diffraction patterns at several times following the onset of an electric field of 84 MV/m. The diffraction patterns were acquired with the diffractometer set for the zero-field Bragg condition. (b) The integrated intensity of the domain satellites as a function of time in electric fields ranging from 30 MV/m to 168 MV/m.

The magnitude of the electric field has a profound effect on the rate of the change of the intensities of domain satellites. A characteristic time representing the timescale of

the transition of stripe domains was extracted by fitting the time-dependence of the intensities in Fig. 3.7(b) with an exponential decay function. This exponential, to which we attach no specific physical meaning, is a convenient model-independent approach for extracting the characteristic time of switching. As shown in Fig. 3.8, the characteristic time is on the order of 1-100 nanoseconds and depends on the magnitude of electric fields. Specifically, the timescale is reduced by more than one order of magnitude when the electric field is increased from 38 to 168 MV/m.

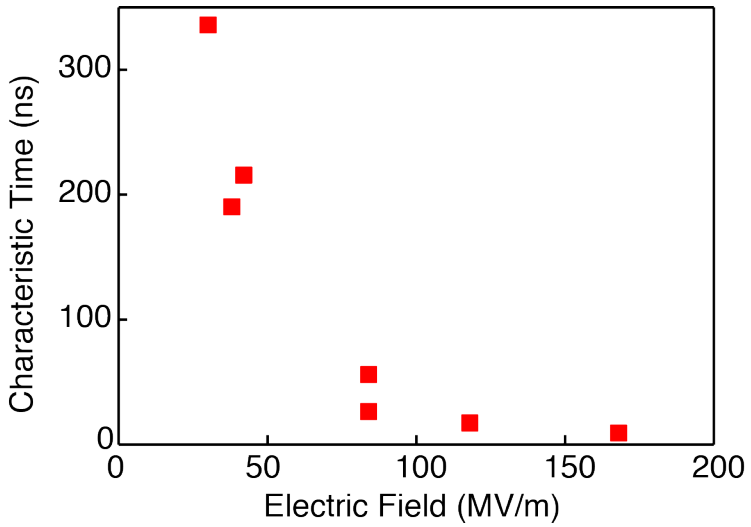

Figure 3.8 Characteristic times for the dynamics of the domain reflection as a function of the magnitude of electric fields.

The applied electric fields not only modify the energy landscape of the superlattice to favor a monodomains state but also set the kinetics of the polarization switching. Merz's law describes the switching kinetics in compositionally uniform ferroelectrics [21], where the maximum switching current i is related to external fields:

$$i \propto \exp(-\alpha / E) \tag{3.3}$$

Here α is the activation energy for the domain switching. Extending the Merz's law to the superlattice studied here, we can expect that the decrease of the intensity of domain

satellites is more rapid at higher fields, as we observed. The case of superlattice is also much more complicated because the activation energy can vary as the topological arrangement of stripe domains changes across the superlattice. As a result, the region of superlattice that conserves the stripe domain at a particular time under a relatively low electric field can be completely transformed under a relatively large electric field.

Finally, we note that the domain satellites are still observable with very low intensity even after times as long as 150 ns after the beginning of electric fields with magnitudes as high as 168 MV/m. The persistence of the domain diffuse scattering peak indicates that a complete transformation to the uniform polarization state requires longer than this duration. Using bipolar triangular voltage waveforms in which each voltage polarity is applied for 0.6 ms, a complete polarization switching is achieved in electrical measurements.

3.7 Conclusions

The time-resolved x-ray study in the $PbTiO_3$/ $SrTiO_3$ superlattice presented here reveals a novel polarization switching mechanism. Electromechanical considerations lead us to conclude that regions of stripe domains switch at different rates in a macroscopic level across the extent of the sample. The magnitude of the applied electric field determines the kinetics of the transition of stripe domains, and modifys the timescale over which the transformation occurs. The observation that the stripe domains can be switched at a timescale as fast as a few nanoseconds at high fields leads to the possibility that the stripe degree of freedom can be manipulated in device structures with GHz operating frequencies.

3.8 References

[1] J. B. Neaton, and K. M. Rabe, "*Theory of Polarization Enhancement in Epitaxial $BaTiO_3/SrTiO_3$ Superlattices,"* Appl. Phys. Lett. **82**, 1586 (2003).

[2] H. N. Lee *et al.*, "*Strong Polarization Enhancement in Asymmetric Three-component Ferroelectric Superlattices,"* Nature **434**, 792 (2005).

[3] E. Bousquet *et al.*, "*Improper Ferroelectricity in Perovskite Oxide Artificial Superlattices,"* Nature **452**, 732 (2008).

[4] M. Dawber *et al.*, "*Tailoring the Properties of Artificially Layered Ferroelectric Superlattices,"* Adv. Mater. **19**, 4153 (2007).

[5] E. Specht, H. Christen, D. Norton, and L. Boatner, "*X-Ray Diffraction Measurement of the Effect of Layer Thickness on the Ferroelectric Transition in Epitaxial $KTaO_3/KNbO_3$ Multilayers,"* Phys. Rev. Lett. **80**, 4317 (1998).

[6] P. Zubko, N. Stucki, C. Lichtensteiger, and J. M. Triscone, "*X-Ray Diffraction Studies of 180 degrees Ferroelectric Domains in $PbTiO_3/SrTiO_3$ Superlattices under an Applied Electric Field,"* Phys. Rev. Lett. **104**, 187601 (2010).

[7] S. Lisenkov, I. Ponomareva, and L. Bellaiche, "*Unusual Static and Dynamical Characteristics of Domain Evolution in Ferroelectric Superlattices,"* Phys. Rev. B **79**, 024101 (2009).

[8] V. Stephanovich, I. Luk'yanchuk, and M. Karkut, "*Domain-enhanced Interlayer Coupling in Ferroelectric/Paraelectric Superlattices,"* Phys. Rev. Lett. **94**, 047601 (2005).

[9] D. D. Fong *et al.*, "*Ferroelectricity in Ultrathin Perovskite Films,"* Science **304**, 1650 (2004).

[10] S. K. Streiffer *et al.*, "*Observation of Nanoscale 180 Degrees Stripe Domains in Ferroelectric $PbTiO_3$ Thin Films,"* Phys. Rev. Lett. **89**, 067601 (2002).

[11] R. Takahashi *et al.*, "*Ferroelectric Stripe Domains in $PbTiO_3$ Thin Films: Depolarization Field and Domain Randomness,"* J. Appl. Phys. **104**, 064109 (2008).

[12] P. Aguado-Puente, and J. Junquera, "*Structural and Energetic Properties of Domains in $PbTiO_3/SrTiO_3$ Superlattices from First Principles,"* Phys. Rev. B **85**, 184105 (2012).

[13] R. Mehta, Silvermabd, and J. Jacobs, "*Depolarization Field in Thin Ferroelectric Films,"* J. Appl. Phys. **44**, 3379 (1973).

[14] P. Zubko *et al.*, "*Ferroelectric Domains in $PbTiO_3/SrTiO_3$ Superlattices,"* Ferroelectrics **433**, 127 (2012).

[15] J. Y. Jo *et al.*, "*Nanosecond Dynamics of Ferroelectric/Dielectric Superlattices,"* Phys. Rev. Lett. **107**, 055501 (2011).

[16] T. Ejdrup *et al.*, "*Picosecond Time-resolved Laser Pump/X-ray Probe Experiments Using a Gated Single-photon-counting Area Detector,"* J. Synchrot. Radiat. **16**, 387 (2009).

[17] A. Tripathi *et al.*, "*Dichroic Coherent Diffractive Imaging,"* Proc. Natl. Acad. Sci. U.S.A. **108**, 13393 (2011).

[18] L. Chen, and A. L. Roytburd, "*180 Degrees Ferroelectric Domains as Elastic Domains,"* Appl. Phys. Lett. **90**, 102903 (2007).

[19] A. Grigoriev *et al.*, "*Nanosecond Domain Wall Dynamics in Ferroelectric Pb(Zr,Ti)O3 Thin Films,"* Phys. Rev. Lett. **96**, 187601 (2006).

[20] R. C. Miller, and G. Weinreich, "*Mechanism for the Sidewise Motion of 180° Domain Walls in Barium Titanate,"* Phys. Rev. **117**, 1460 (1960).

[21] W. J. Merz, "*Domain Formation and Domain Wall Motions in Ferroelectric $BaTiO_3$ Single Crystals,"* Phys. Rev. **95**, 690 (1954).

4 Interlayer Domain Distortion and Piezoelectric Strain in $PbTiO_3/SrTiO_3$ Superlattices

4.1 Introduction

The atomic-scale structure of ferroelectric/dielectric superlattices is determined to a great extent by the interaction between the lattice distortion and polarization of component layers [1, 2]. In a superlattice where dielectric layers are sufficiently thick, the dielectric layers partially decouple the adjacent ferroelectric layers and promote the formation of stripe polarization domains [3-5]. The dielectric layers become polarized, but the polarization in the center of the dielectric layers is much less than the polarization in the ferroelectric layers [6-9]. In addition to the in-plane polarization periodicity, stripe domains also modify the lattice structure. Polarization vortices [10, 11] are predicted to occur at corners of domains to accommodate the difference between the polarizations of the different component layers. The elastic deformation associated with the polarization vortex can induce a nanometer scale structure into the domain wall, effectively broadening domain walls beyond the unit-cell scale domain walls found in ferroelectrics with uniform composition [8].

The complex interfacial structural phenomena found in ferroelectric/dielectric superlattices lead to unusual dynamics of the polarization domain configuration. In Chapter 3, it has already shown that the electric fields can transform stripe domains into a uniform polarization state, at a characteristic time on the order of tens of nanoseconds [3]. There are several predictions of the effects of the non-uniform polarization profile on the field-induced-evolution of the structure of the superlattice [12-14]. We can conceptually

divide these predictions into two regimes.

In the first regime, at times approximately 1 to 100 ns after the onset of the applied electric field, the stripe domains have not yet switched. During this time range, the stripe pattern is metastable and the lattice structure within the stripe domains show little change of the lattice constant due to mechanical clamping [3, 15]. First-principles calculations predict that the domains walls within the metastable stripe domains in the weakly polarized dielectric layers are slightly displaced with a lower threshold electric field than the ferroelectric layers [13].

In the second regime, long after the onset of the electric field, a uniform polarization state has been reached and the clamping of the lattice structure is lifted. In this case the clamping effect is no longer important and the superlattice as a whole exhibits a large piezoelectric expansion. In the uniform polarization state the domain degree of freedom is no longer available and the polarization of the dielectric layers must increase to match the ferroelectric layers. Because they have a large change of the polarization the dielectric layers can be expected to exhibit a large piezoelectric expansion commensurate with their polarization. These properties of the uniform polarization state have been predicted for $PbTiO_3$/ $SrTiO_3$ superlattices in a first-principles calculation [14], but not yet observed experimentally.

This chapter describes a structural study of how the domain structure and lattice structure evolve in each superlattice component layer as a function of the applied electric field. The experiments probe the atomic structure and domain structure of a $PbTiO_3$/ $SrTiO_3$ superlattice in the two regimes of its response to an applied electric field. *In situ*

time-resolved synchrotron x-ray microdiffraction was used to measure the intensities of x-ray reflections arising (i) from the stripe domain and (ii) from the lattice structure of the superlattice. In the first time regime, the change in the intensities of domain reflections indicates that the average polarization of the dielectric $SrTiO_3$ layers increases. In the second time regime, intensity evolution of the superlattice structural reflections shows that the dielectric $SrTiO_3$ layers exhibit a piezoelectric effect commensurate with the polarization expected due to the elimination of the stripe domains.

4.2 Experimental Arrangement

The $PbTiO_3/SrTiO_3$ superlattice studied here has a similar layer structure to the superlattice sample described in Chapter 3, except that the repeating unit consists of 8 unit cells of $PbTiO_3$ and 3 unit cells of $SrTiO_3$. Time-evolution of the structure of the superlattice during applied electric fields was measured at station 7ID-B of the Advanced Photon Source at Argonne National Laboratory. The experimental setup for the time-resolved x-ray microdiffraction experiment was described in Chapters 2 and 3 [3]. Capacitors with top electrode diameters of 50 and 130 μm were studied in the experiments described in this chapter. The RC charging time constant in the circuit consisting of a superlattice capacitor and the resistive $SrRuO_3$ bottom electrode was 85 ns for the 50 μm-diameter capacitors.

X-ray reflections arising from the lattice and domain structure of the $PbTiO_3$/ $SrTiO_3$ superlattice are shown in the reciprocal space map acquired near the (002) Bragg reflection (Fig. 4.1). The atomic periodicity of the superlattice produces a series of x-ray reflections at out-of-plane wavevectors $Q_z = \frac{2\pi}{d_{avg}}(m + \frac{l}{n})$, where the integer m indexes

the reflections from the average lattice constant of each unit cell d_{avg}, n is the total number of atomic layers in the repeating unit, and l indexes the out-of-plane satellite reflections from the large repeating unit of the superlattice. The reflections from the superlattice structure and stripe domain are labeled using out-of-plane indices m and l. For the sample described in this chapter, the stripe domain pattern has a period of 66 Å and results in diffuse x-ray scattering satellites at in-plane wavevector $Q_y = \pm 0.095$ Å^{-1}.

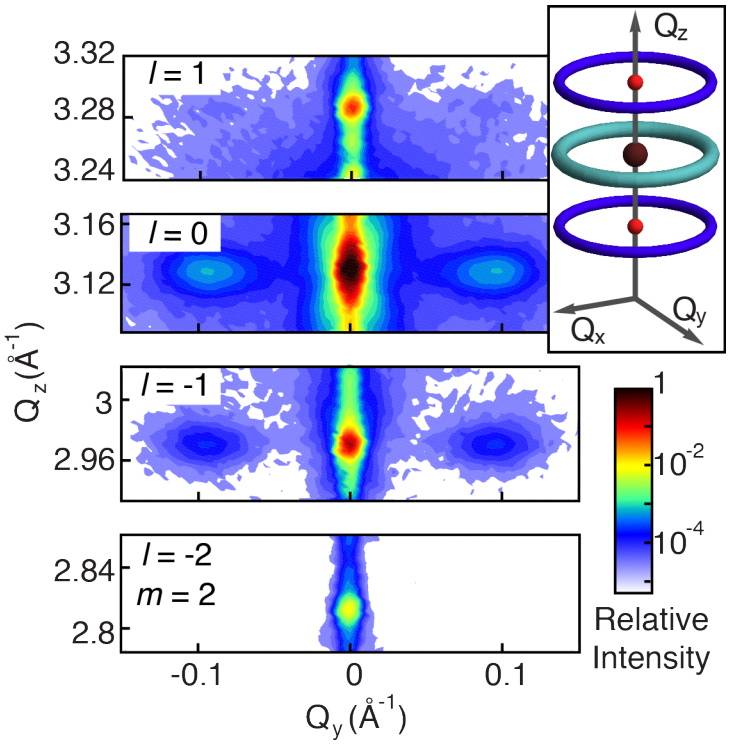

Figure 4.1 Reciprocal space map of the $PbTiO_3/SrTiO_3$ superlattice acquired near the $m = 2$ reflections. A schematic of the three-dimensional reciprocal space of the superlattice is shown as an inset. The spheres along $Q_x = Q_y = 0$ and the surrounding rings represent superlattice structural reflections and domain satellite reflections, respectively.

A superlattice can be viewed as a convolution of its repeating unit with a lattice with a period corresponding to the size of the repeating unit, as shown in Fig. 4.2. The x-ray scattering pattern gives the squared magnitude of the Fourier transform of the electron density associated with this superlattice structure. The wavevectors of the

maxima in the diffraction pattern are determined by the periodicity of the repeating unit. The intensities of these peaks are determined by the atomic structure within the repeating unit. In the structural measurement described here we mapped out the x-ray intensity distribution of two series of x-ray reflections: (i) the reflections arising from the stripe domain pattern and (ii) the conventional superlattice reflections from the atomic layering. Analysis of these diffraction patterns provides information about the contribution of each component layer to the domain configuration and the lattice parameter within each layer.

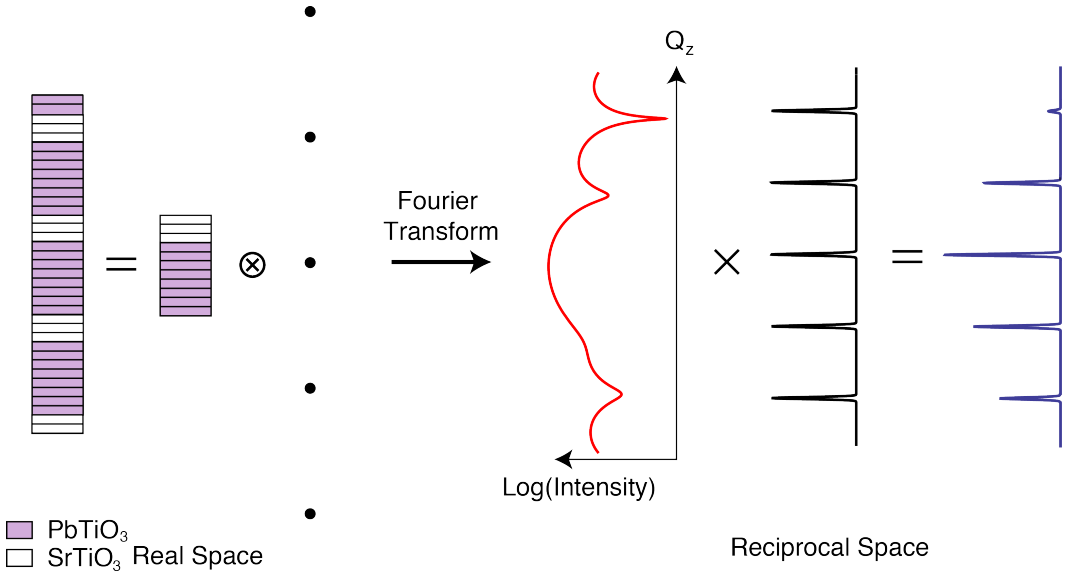

Figure 4.2 Schematics showing the principles of the convolution theorem in relating the real space of a superlattice to the x-ray diffraction pattern in reciprocal space. The symbol ⊗ indicates the convolution operation. The intensity vs. Q_y curve is calculated based one repeating unit of the experimental sample with a kinematical x-ray diffraction simulation.

4.3 Electric-field Dependent Domain Distortion

The transformation from the stripe domain state to the uniform polarization state leads to the decrease in the intensity of domain satellite plotted in the Fig. 4.3(a). Similar switching behavior was discussed in detail in Chapter 3. In Fig. 4.3(a), the intensity of the domain satellite deceases by 80% at a time 30 ns after the onset of a 212 MV/m electric

field. The following discussion focuses on the initial 20 ns of the switching process during which the stripe domains are not yet completely transformed and in which a significant fraction of the sample is in a metastable stripe domain state.

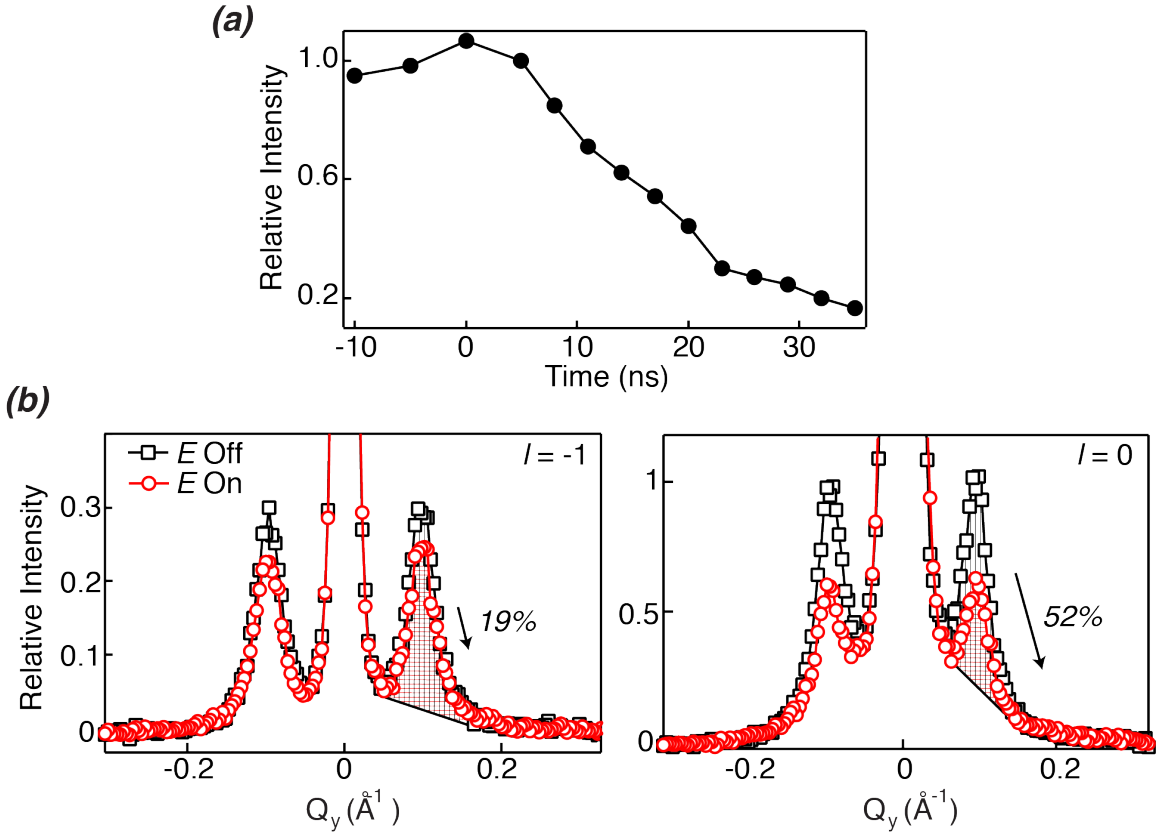

Figure 4.3 (a) Normalized intensity of the domain satellite with $m = 2$ and $l = 0$ as a function of time during a 60 ns-duration electric field with a magnitude of 212 MV/m. (b) Diffraction patterns along the Q_y direction for $l = -1$ (left panel) and $l = 0$ (right panel) domain satellites, at zero field (squares) and 5 ns after the onset of a 60 ns, 212 MV/m electric field (circles). The hatching and cross-hatching indicate the areas over which the intensities of the domain satellites are integrated.

The evolution of the superlattice structure leads to changes in the relative intensities of the intensity distribution of the domain satellites. Here we analyze the field-induced change of the intensities of the domain satellites with $l = 0$ and $l = -1$, as shown in Fig. 4.3(b). The domain satellites with $l = -2$ and 1 are too weak to be distinguished from the background under our experimental conditions (Fig. 4.1) and thus will not be

analyzed. The integrated intensities of domain satellites decrease in the applied electric field at a rate that depends on the indices of the reflections. At 5 ns after the onset of an electric field with a nominal magnitude of 212 MV/m, the integrated intensity of l = -1 domain satellite has decreased by 19% with respect to its zero-field intensity. In comparison, the l = 0 domain satellite has decreased much more dramatically at this time, by 52%. The difference in the rate at which the intensity decreases reflects the change of the domain configuration within the repeating unit of the superlattice under applied fields.

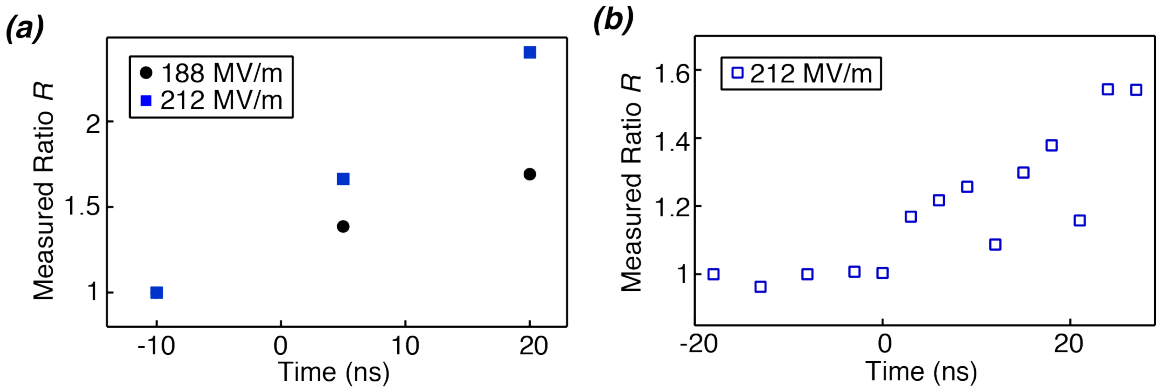

Figure 4.4 Ratios of the integrated intensities of the l = -1 domain satellites to the l = 0 domain satellites as a function of time under electric fields with different nominal magnitudes. The diffraction patterns used in (a) are optimized separately for both l = 0 and l = -1 domain satellites. Diffraction patterns used in (b) are optimized for l = 0 domain satellites only.

The quantitative analysis of the atomic structure within the superlattice requires carefully removing the contribution to the relative intensities arising from the transformation of stripe domains to the uniform polarization state. To do this we define a quantity R, which is ratio of the integrated intensities of l = -1 domain satellites to l = 0 domain satellites.

The ratio R was measured using two different segments of the diffuse domain satellite rings. The plot in Fig. 4.4(a) is based on diffraction patterns with the incident

angle optimized separately for $l = 0$ and $l = -1$ domain satellites. The diffraction patterns used to measure R in Fig. 4.4(b) were optimized for $l = 0$ domain satellites only, but also capture the shoulder of $l = -1$ domain satellites. In Fig. 4.4(b), the intensities of $l = 0$ and -1 domain satellites are integrated over different geometric segments of the ring of diffuse scattering and thus could possibly be sensitive to artifacts associated with changes in the domain geometry. In both cases, however, Fig. 4.4 shows that R increases by more than 50% at 20 ns after the application of a large electric field.

4.4 Domain Distortion Models

The field-induced changes in the relative intensities of domain satellites arise from changes in the way the polarization and atomic structure are distributed within the repeating unit of the superlattice. In principle, a measurement of the relative intensities with a large number of domain satellites could be used to obtain this information exactly. The exact domain structure is not available, however, because it was possible to measure only a limited number of domain satellites in our experiments. There is sufficient information in the experimental data, however, to build a kinematic x-ray diffraction simulation that captures the key field-induced structural changes.

The simulation is based on a calculation of the overall structural factor of an arrangement of atoms with the same repeating unit as the experimental superlattice. We have previously developed a model to simulate the intensities of superlattice reflections under different conditions of how the strain is distributed in ferroelectric and dielectric layers in a single domain state [16]. Here we extend this model to account for the nanoscale stripe domains. The domain x-ray satellites result from the difference in the structure factors of the unit cells with opposite polarizations. As a result, the domain

satellites are affected by parameters including the positioning of domain walls, lattice constant and atomic displacement in both $PbTiO_3$ and $SrTiO_3$ layers.

The lateral extent of the simulation encompasses a domain period of 16 unit cells, approximately matching the experimental domain period. The $SrTiO_3$ bulk lattice constant 3.905 Å is used as the global in-plane lattice constant, which is consistent with the coherent epitaxial growth of the superlattice. Along the out-of-plane direction, we apply the $SrTiO_3$ bulk lattice constant to the $SrTiO_3$ layers and stretch the $PbTiO_3$ layers so that the total average lattice constant of the simulation agrees with the experiment. The ferroelectric polarization is accounted for by displacing atoms away from their high-symmetry sites within both $PbTiO_3$ and $SrTiO_3$ unit cells. The $PbTiO_3$ atomic positions are chosen to match those found in $PbTiO_3$ ceramics [17]. Theoretical studies of the stripe domain state predict that the polarization in $SrTiO_3$ layers is 30%-50% of the polarization in $PbTiO_3$ layers [6, 8]. We therefore make a simplifying assumption that the fractional atomic displacements in $SrTiO_3$ layers are 40% of those in $PbTiO_3$ layers. The key results of the simulation, however, do not depend on the magnitude of the initial atomic displacements in $SrTiO_3$ layers.

In zero-applied electric field, each component has a fixed out-of-plane polarization in which upward and downward polarization directions each have a 50% volume fraction. We further assume that the zero-field domain walls are perfectly aligned in each layer with a zero width, as shown in Fig. 4.5(a). We have neglected all in-plane components of the polarization and the polarization vortices predicted in theoretical calculations.

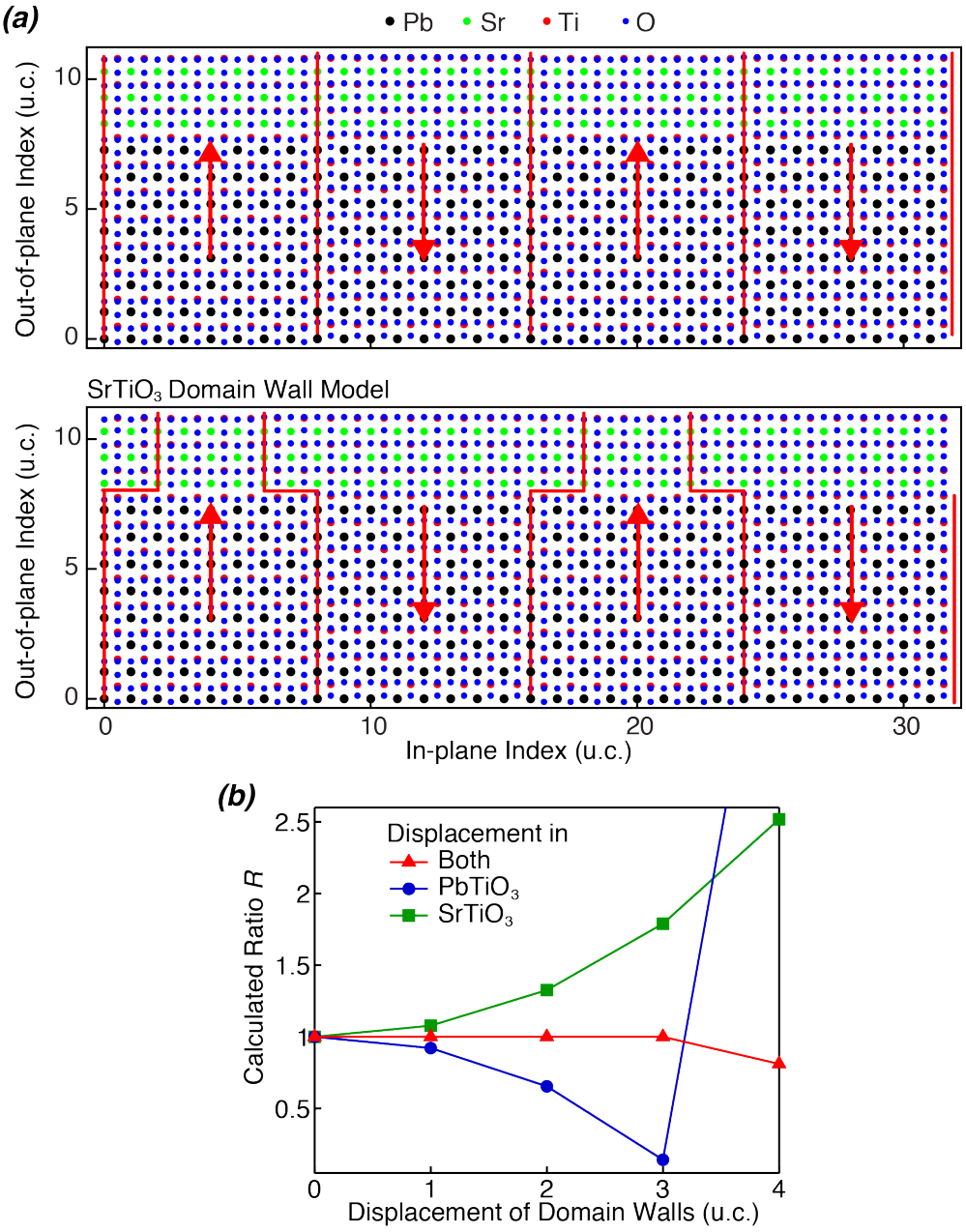

Figure 4.5 Arrangements of atoms of the simulated $PbTiO_3/SrTiO_3$ superlattice with (a) well-aligned domain walls and (b) domain walls displaced by two unit cells in $SrTiO_3$ layers. (c) The calculated ratio R as a function of domain wall displacement in both component layers (triangles), in $PbTiO_3$ layers only (circles) and in $SrTiO_3$ layers only (squares).

We hypothesize that the experimentally observed changes of the relative intensities of domain satellites are caused by the modification of the domain configuration within $SrTiO_3$ layers. Lisenkov *et al.* predict that the weakly polarized

dielectric layers are less stable than the ferroelectric layers, and consequently exhibit increased polarization before the ferroelectric layers under the same applied electric fields [13]. Following these predictions, we have constructed two distinct models of the superlattice in applied electric fields. We have used these models to compute the intensity of the domain satellite as the overall polarization of $SrTiO_3$ layers increases. The models are (1) that the domain walls in the $SrTiO_3$ layer are slightly displaced as a result of the electric field and (2) that the fractional atomic displacements in $SrTiO_3$ layers are modified by the electric field. Other factors that affect the intensities of domain satellites, including the lattice constant of each component layer, do not change within the domains under the applied electric field, and are thus not considered here [3].

In the first model, we displace all the domain walls into the polarization-up domains in $SrTiO_3$ layers so that the $SrTiO_3$ layers develop a net polarization aligned with the applied electric field. Situations with zero displacement and with a displacement of two unit cells are shown in Fig. 4.5(b). We have also considered alternative geometries for the domain wall displacement, including cases where the domain walls are displaced in the $PbTiO_3$ layers as well as in both $SrTiO_3$ and $PbTiO_3$ layers.

For each simulation, the quantity R, the ratio of the integrated intensities of $l = -1$ domain satellites to $l = 0$ domain satellites, is computed. The results are summarized in Fig. 4.5(c). The value of the ratio R depends on the displacement of the domain walls in on the geometry of the domain wall displacement (*i.e.* in $SrTiO_3$, $PbTiO_3$ or both). A monotonically increase in R trend is predicted to occur when only domain walls in $SrTiO_3$ layers are displaced. In the extreme case where the domain walls are displaced by four unit cells, the stripe domain pattern no longer persists in the $SrTiO_3$ layer and the

ratio R increases by a factor of 2.4. In compassion, when the domain walls in $PbTiO_3$ layers are displaced, ratio R decreases initially, and then shows an anomaly of large increase at the point where the stripes are eliminated.

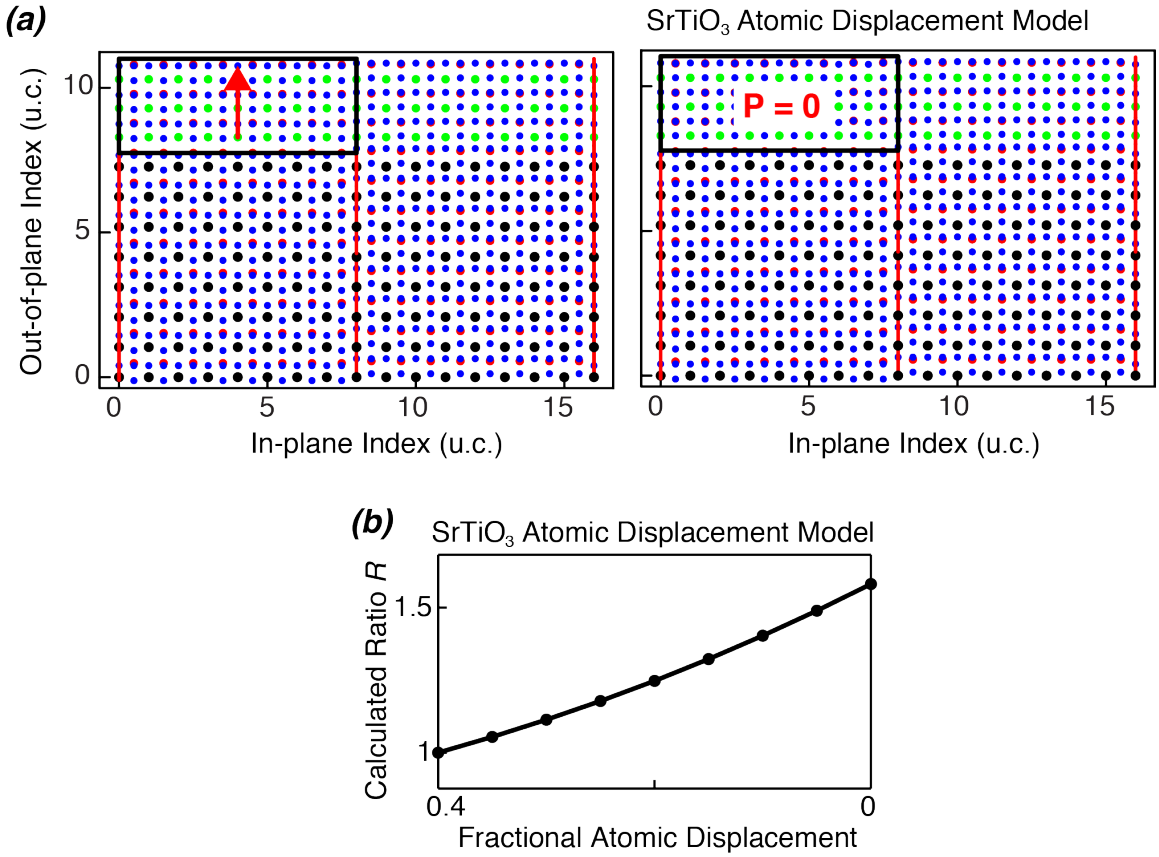

Figure 4.6 (a) Arrangements of atoms in the simulated $PbTiO_3/SrTiO_3$ superlattice in two situations: the fractional atomic displacement of $SrTiO_3$ polarization-up domains is 40% of that in $PbTiO_3$ bulk ceramics (left panel), and is reduced to zero (right panel). (b) Simulated change in R resulting from decreased fractional atomic displacement in polarization-up domains of $SrTiO_3$ layers. The fractional atomic displacement is normalized to the value in $PbTiO_3$ bulk ceramics.

In the second model, we increase the overall polarization of $SrTiO_3$ layers by changing the fractional atomic displacement within the polarization-up domains of the $SrTiO_3$ layers. Fig. 4.6(a) shows the zero-field atomic arrangement when the fractional atomic displacement of the $SrTiO_3$ layers is 40% of that in the $PbTiO_3$ layers, and field-induced atomic arrangement when the fractional atomic displacement of the $SrTiO_3$

layers is reduced to zero. The simulated ratio *R* increases monotonically as the fractional atomic displacement decreases, as shown in Fig. 4.6(b). In the case where the initially polarization-up domains of $SrTiO_3$ layers become non-polar, with a centrosymmetric unit cell, the ratio *R* increases by a factor of 1.6.

The increase of the ratio *R* we observed during the application of large electric fields shows that the stripe domains are slightly distorted before the transformation into a uniform polarization state. The exact form of the distortion is unclear, but both the domain-wall and atomic-displacement models point to a similar physical effect that an increase of the average polarization in $SrTiO_3$ layers leads to an increase of the ratio *R*. Both models lead us to the same consistent picture that high electric fields increase the net polarization of $SrTiO_3$ layers in the metastable stripe-domain state, but leave the $PbTiO_3$ layers unaffected. The increase of the ratio *R* we observed agrees with the kinematic x-ray diffraction simulation, and the maximum change is within the range of prediction. The magnitude of the distortion is expected to increase with the magnitude of electric fields. This electric field scaling accounts for the time dependence of the ratio *R* shown in Fig. 4.4, where the magnitude of the field is increasing in the initial 20 ns after the onset of applied electric fields, since the charging time constant of superlattice capacitors is a factor of four larger than 20 ns.

4.5 Interlayer Distribution of Piezoelectric Strain

We now focus on the second time regime, long after the onset of the applied electric fields. Because the lattice structure is coupled to the remnant polarization, the field-induced evolution of the atomic structure of each superlattice component provides insight into the evolution of the polarization distribution. In this time regime, the domain

pattern disappears and only the structural superlattice x-ray reflections at $Q_x = Q_y = 0$ remain. The diffraction patterns are produced mainly by area with uniform polarization. The mechanical clamping imposed by the stripe domain pattern is removed and the superlattice as a whole exhibit piezoelectric expansion [3]. A structural prediction based on the evolution of the initial non-uniform polarization profile [14] is tested in this section. We start with the hypothesis that, because of their large change in polarization, the $SrTiO_3$ layers exhibit a larger piezoelectric expansion than the $PbTiO_3$ layers.

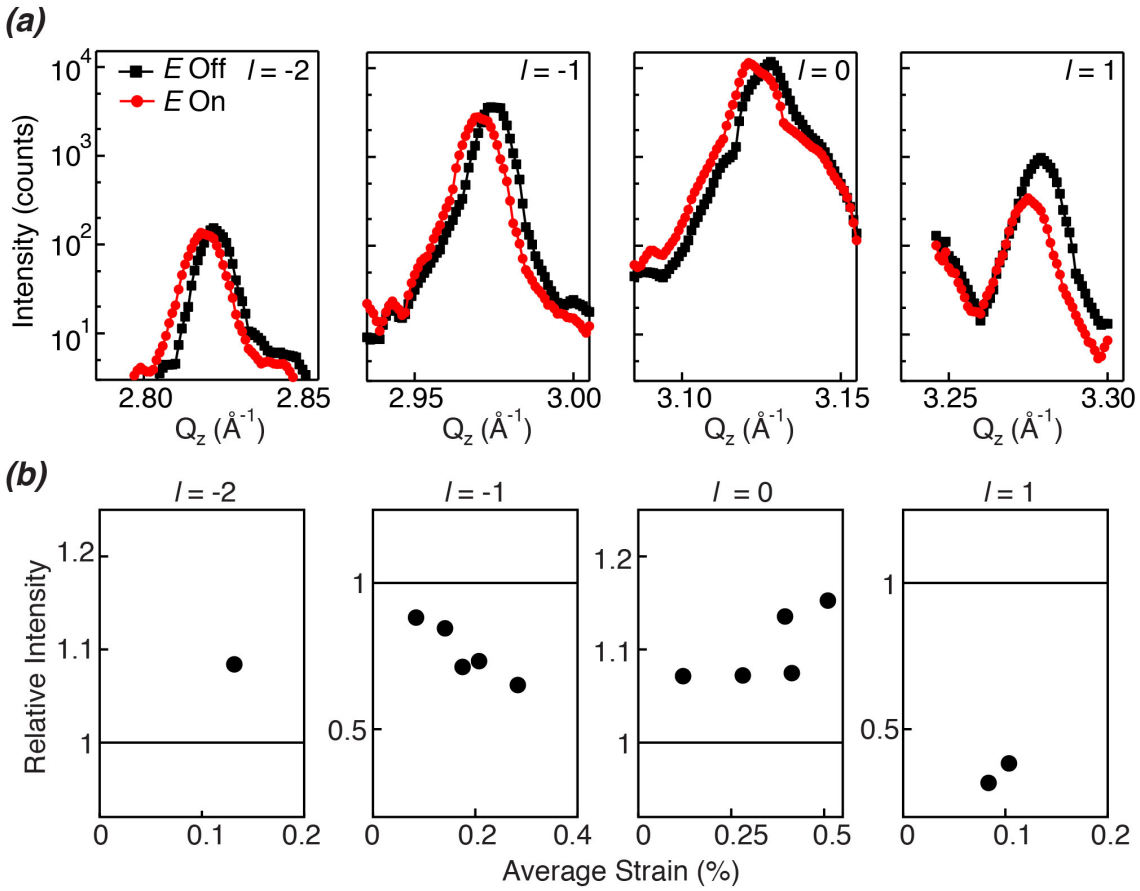

Figure 4.7 (a) Diffraction patterns of superlattice structural reflections with indices *m* = 2 and *l* = -2, -1, 0 and 1 at zero fields (square) and at the end of a 300 ns, 212 MV/m electric fields (circle). (b) The integrated intensities of superlattice structural reflections with indices *m* = 2 and *l* = -2, -1, 0 and 1 normalized to zero-field values as a function of the average strain.

Fig. 4.7(a) shows diffraction patterns of superlattice structural reflections with m = 2 and l = 2, -1, 0 and 1, acquired at zero fields and under 212 MV/m electric field pulses. The diffraction patterns are shown for a time 300 ns after the beginning of applied fields is chosen, so that the superlattice has approximately reached the uniform polarization state. The diffraction patterns acquired in the applied electric fields are different in two respects from the patterns acquired at zero applied fields. First, all of the x-ray reflections acquired in the applied field are shifted to lower Q_z due to piezoelectric expansion. The piezoelectric strain is determined by measuring the shift in the center of mass of the intensity distribution along Q_z. Second, the reflections change in intensity due to the change in the atomic structure within the repeating unit of the superlattice. The intensities integrated over three-dimensional space in reciprocal space are shown as a function of the piezoelectric strain in Fig. 4.7(b).

The magnitude and sign of the field-induced changes in the intensity depend on the indices of the reflections. The intensities of the l = -2 and l = 0 reflections increase after the transformation to the uniform-polarization state while the l = -1 and l = 1 superlattice reflections decrease in intensity. In this particular case, the magnitude of the intensity change is larger for the reflections with decreased intensity. For example, at 0.1% strain the structural reflection with l = 1 exhibits a 60% decrease in its intensity in the applied field and the l = 0 reflection has an 8% increase in intensity.

A kinematic x-ray diffraction simulation similar to that in section 4.4 was used to interpret the structural changes responsible for the field-induce changes in the intensities of the superlattice structural reflections. The simulation compares the intensities of the x-ray reflections from the eventual uniform polarization-down state to the intensities of

reflections from the initial stripe domain configuration. The polarization transformation is accounted by changing the sign of the fractional atomic displacement in both the $SrTiO_3$ and $PbTiO_3$ layers. We consider three options for how the $PbTiO_3$ and $SrTiO_3$ layers share the piezoelectric strain: (1) the distortion is distributed evenly between $PbTiO_3$ and $SrTiO_3$ layers, (2) the distortion occurs only in $PbTiO_3$ layers and (3) the distortion occurs only in $SrTiO_3$ layers. These options are schematically shown in Fig. 4.8(a) where the fraction of strain in the $PbTiO_3$ layers is denoted as F. We also include the change of lattice constants due to the piezoelectric expansion and allow the atomic displacements in the $SrTiO_3$ layers to increase as the size of $SrTiO_3$ unit cells increases.

The atomic model proposed by Swartz and Wu points out that the interfacial layer has different lattice structure compared to adjacent superlattice components [14]. We approximate this model by setting the lattice parameter of the interfacial layer as the average of lattice parameters of neighboring layers. This consideration, however, does not affect the key results of the intensity calculation.

The polarization switching itself changes the intensity of the superlattice x-ray reflections. Polarization-down and polarization-up unit cells have different structure factors when both the fractional atomic displacements and the desperation correction of the atomic scattering factor are taken into account. For the x-ray reflections we studied here, the diffracted intensity associated with the polarization-down configuration is larger than the zero-field stripe domain pattern. This difference is apparent in the calculated zero-strain x-ray intensity for four different superlattice structural reflections with $m = 2$, $l = -2$, -1 0 and 1, as shown Fig. 4.8(b). The magnitude of the increase of the relative intensity varies with the indices of the x-ray reflection. A similar dependence of the

intensity on the crystallographic direction of the remnant polarization is observed in compositionally uniform Pb(Zr,Ti)O_3 thin films [18, 19].

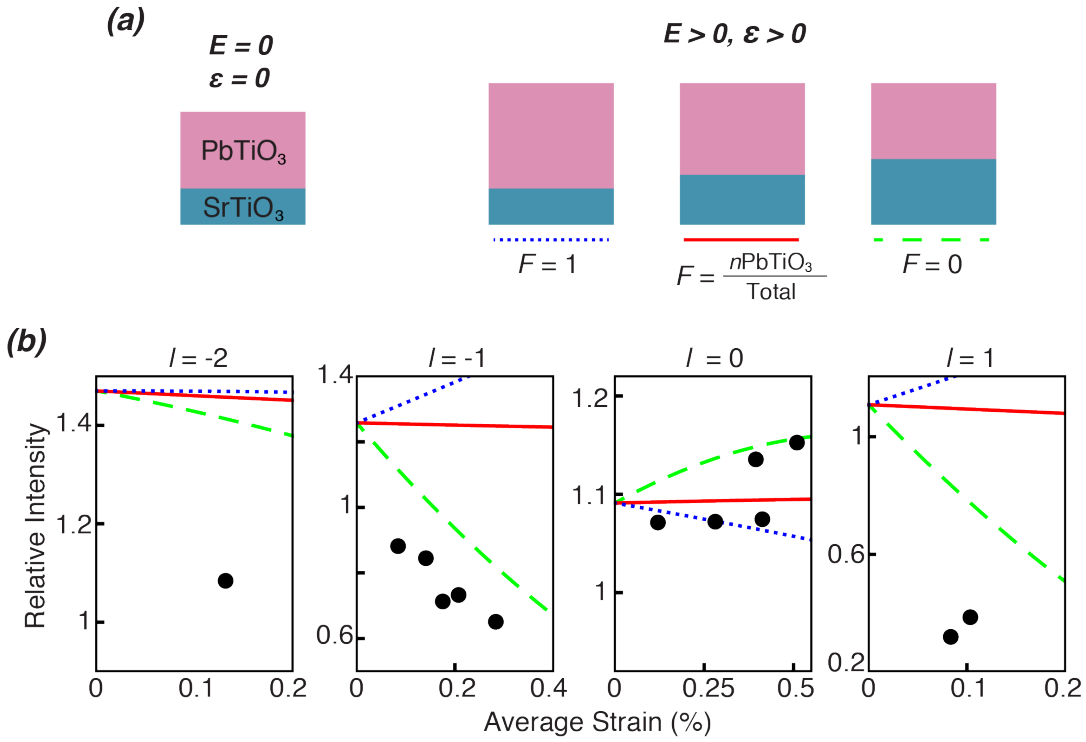

Figure 4.8 (a) Sketch of the strain distribution model. Here *F* is the fraction of strain in the $PbTiO_3$ layers. (b) Comparison of the experimental measured integrated intensities and the kinematic simulation of superlattice structural reflections with indices *m* = 2 and *l* = -2, -1, 0, and 1 as a function of the average strain. The lines are kinematic simulations in which the piezoelectric distortion is equal in $PbTiO_3$ and $SrTiO_3$ layers (solid lines), only in $PbTiO_3$ layers (dotted lines), and only in $SrTiO_3$ layers (dashed lines).

As the piezoelectric strain develops in the superlattice, the calculated x-ray scattering intensity is strongly affected by the strain distribution across the component layers. The relative intensity shows little change with the average strain in the case where the $SrTiO_3$ and $PbTiO_3$ layers share the strain evenly. On the contrary, when the strain is only concentrated in one of the superlattice components, the relative intensity deviates from the zero-strain prediction as the average strain increases. The largest intensity

change is predicted for structural reflections with $l = 1$. For instance, the relative intensity drops to 30% when 0.1% strain occurs in only the $SrTiO_3$ layers.

The experimentally observed variation of the intensity as a function of the piezoelectric strain is best fit by the case where all of the piezoelectric distortion occurs in the $SrTiO_3$ layers. The $l = -1$ and 1 superlattice reflections, for example, decrease as the piezoelectric distortion increases, agree with the x-ray diffraction simulation, as shown in Fig. 4.8(b). The intensity variation in the superlattice structural reflections shows that the $SrTiO_3$ layers are stretched more significantly than the $PbTiO_3$ layers under the applied electric fields. The larger piezoelectric distortion in the $SrTiO_3$ layers matches the expectation of the transformation of the weakly coupled $PbTiO_3$/ $SrTiO_3$ superlattices into strongly coupled superlattices, in which the polarization reaches a uniform distribution across superlattice components [14].

The intensity changes shown here are unique for weakly coupled $PbTiO_3$/ $SrTiO_3$ superlattices, and are very different from $BaTiO_3$/$CaTiO_3$ superlattices. The latter superlattice behaves as a compositionally uniform ferroelectric under large electric fields. The piezoelectric strain is distributed evenly in the ferroelectric $BaTiO_3$ and dielectric $CaTiO_3$ layers and x-ray diffraction patterns do not show intensity changes in the superlattice reflections as the overall lattice expanses [16, 20].

4.6 Conclusions

We have shown that the relatively weak polarization of the $SrTiO_3$ layers in a $PbTiO_3$/ $SrTiO_3$ superlattice has important effects on the evolution of the domain and atomic structure in applied electric fields [21]. The layer-dependent evolution of the

nanometer-scale polarization configuration and the associated structural distortion were measured in two time regimes. The evolution of the x-ray diffraction pattern is consistent with theoretical predictions that the applied field leads to large increases in the polarization of the $SrTiO_3$ component. The x-ray characterization methods used here provide the atomic-to-nanoscale structural resolution required to understand the dynamic properties of this system. Insight into the origin of the time-domain properties of superlattices has the potential to increase the functionalities of complex oxides by providing the means to tune the field- and time-dependence of electronic properties.

4.7 References

[1] E. Bousquet *et al.*, "*Improper Ferroelectricity in Perovskite Oxide Artificial Superlattices,"* Nature **452**, 732 (2008).

[2] M. Dawber *et al.*, "*Unusual Behavior of the Ferroelectric Polarization in $PbTiO_3/SrTiO_3$ Superlattices,"* Phys. Rev. Lett. **95**, 177601 (2005).

[3] J. Y. Jo *et al.*, "*Nanosecond Dynamics of Ferroelectric/Dielectric Superlattices,"* Phys. Rev. Lett. **107**, 055501 (2011).

[4] P. Zubko *et al.*, "*Electrostatic Coupling and Local Structural Distortions at Interfaces in Ferroelectric/Paraelectric Superlattices,"* Nano Lett. **12**, 2846 (2012).

[5] V. Stephanovich, I. Luk'yanchuk, and M. Karkut, "*Domain-enhanced Interlayer Coupling in Ferroelectric/Paraelectric Superlattices,"* Phys. Rev. Lett. **94**, 047601 (2005).

[6] D. C. Ma, Y. Zheng, and C. H. Woo, "*Phase-field Simulation of Domain Structure for $PbTiO_3/SrTiO_3$ Superlattices,"* Acta Mater. **57**, 4736 (2009).

[7] A. Torres-Pardo *et al.*, "*Spectroscopic Mapping of Local Structural Distortions in Ferroelectric $PbTiO_3/SrTiO_3$ Superlattices at the Unit-cell Scale,"* Phys. Rev. B **84**, 220102(R) (2011).

[8] P. Aguado-Puente, and J. Junquera, "*Structural and Energetic Properties of Domains in $PbTiO_3/SrTiO_3$ Superlattices from First Principles,"* Phys. Rev. B **85**, 184105 (2012).

[9] Y. L. Li *et al.*, "*Prediction of Ferroelectricity in $BaTiO_3/SrTiO_3$ Superlattices with Domains,"* Appl. Phys. Lett. **91**, 112914 (2007).

[10] C. T. Nelson *et al.*, "*Spontaneous Vortex Nanodomain Arrays at Ferroelectric Heterointerfaces,"* Nano Lett. **11**, 828 (2011).

[11] C.-L. Jia *et al.*, "*Direct Observation of Continuous Electric Dipole Rotation in Flux-Closure Domains in Ferroelectric $Pb(Zr,Ti)O_3$,"* Science **331**, 1420 (2011).

[12] A. P. Levanyuk, and I. B. Misirlioglu, "*Phase Transitions in Ferroelectric-paraelectric Superlattices,"* J. Appl. Phys. **110**, 114109 (2011).

[13] S. Lisenkov, I. Ponomareva, and L. Bellaiche, "*Unusual Static and Dynamical Characteristics of Domain Evolution in Ferroelectric Superlattices,"* Phys. Rev. B **79**, 024101 (2009).

[14] C. Swartz, and X. Wu, "*Modeling Functional Piezoelectricity in Perovskite Superlattices with Competing Instabilities,"* Phys. Rev. B **85**, 054102 (2012).

[15] L. Chen, and A. L. Roytburd, "*180 Degrees Ferroelectric Domains as Elastic Domains,"* Appl. Phys. Lett. **90**, 102903 (2007).

[16] J. Y. Jo *et al.*, "*Piezoelectricity in the Dielectric Component of Nanoscale Dielectric-Ferroelectric Superlattices,"* Phys. Rev. Lett. **104**, 207601 (2010).

[17] P. P. Neves *et al.*, "*XAS and XRD Structural Characterization of Lanthanum-Modified $PbTiO_3$ Ceramic Materials,"* The Journal of Physical Chemistry B **108**, 14840 (2004).

[18] D. H. Do *et al.*, "*Structural Visualization of Polarization Fatigue in Epitaxial Ferroelectric Oxide Devices,"* Nature Mater. **3**, 365 (2004).

[19] J. Y. Jo *et al.*, "*Structural Consequences of Ferroelectric Nanolithography,"* Nano Lett. **11**, 3080 (2011).

[20] J. Y. Jo *et al.*, "*Component-specific Electromechanical Response in a Ferroelectric/dielectric Superlattice,"* Phys. Rev. B **82**, 174116 (2010).

[21] P. Chen *et al.*, "*Field-Dependent Domain Distortion and Interlayer Polarization Distribution in $PbTiO_3/SrTiO_3$ Superlattices,"* Phys. Rev. Lett. **110**, 047601 (2013).

5 Nonlinearity of Piezoelectricity in Epitaxial $BiFeO_3$ on $SrTiO_3$ under High Electric Fields

5.1 Introduction

The multiferroic complex oxide $BiFeO_3$ is so far the only single-phase material exhibiting ferroelectric and antiferromagnetic order simultaneously at room temperature [1, 2]. Phenomena in both of these degrees of freedom depend on the crystallographic structure and distortion of the atomic lattice [3, 4]. An in-depth understanding of the structure of $BiFeO_3$ and the evolution of its structure in applied fields are therefore of particular importance. Theoretical calculations have shown that a structure phase of $BiFeO_3$ with tetragonal symmetry have a lower free energy than the bulk rhombohedral phase in high electric fields applied along a pseudocubic <001> direction [5]. For the case in which $BiFeO_3$ is initially unstrained, the predicted threshold electric field is on the order of 1000 MV/m, which is much larger than typical electrical breakdown fields [6] and imposes a technical challenge for experimental tests. No phase transition has been observed, for example, in a previous *in situ* x-ray diffraction measurement under electric fields up to 35 MV/m [7]. In addition to the possibility of a field-induced phase transition, understanding high-electric-field phenomena is also crucial in applications of electronic materials based on thin films and nanostructures, where a moderate voltage can lead to fields higher than 100 MV/m.

Materials near the boundaries in pressure, temperature, or composition between structural phases exhibit piezoelectric, dielectric, and mechanical properties that are very different from those of materials far from the transition. The modification of these

properties is a consequence of the softening of the lattice accompanying the phase transitions [8-10]. Enhanced piezoelectricity has been reported in $BiFeO_3$ thin films in which large compressive biaxial strain [11] or doping with rare earth elements [12] places the system near the structural phase transition. The field-induced phase transition and the corresponding enhancement of the piezoelectricity have been extensively studied in relaxor-ferroelectric systems where the transition electric fields are less than 1 MV/m [13, 14]. In highly strained $BiFeO_3$ thin films grown on substrates with a large lattice mismatch, the rhombohedral and tetragonal phases coexist at zero fields and a field-driven rhombohedral-to-tetragonal phase transition has also been reported under the application of a moderate electric field of 176 MV/m [15]. In epitaxial $BiFeO_3$ thin films grown on $SrTiO_3$ substrates [1], however, the $BiFeO_3$ is more firmly on the rhombohedral side of the phase diagram and the production of the field-induced tetragonal phase has not been experimentally demonstrated.

In this chapter, the structure of an epitaxial $BiFeO_3$ thin film grown on $SrTiO_3$ substrate is characterized under electric fields up to 281 MV/m using time-resolved x-ray microdiffraction. The results of the experiment show that the piezoelectric strain is proportional to the applied electric field up to 150 MV/m, and that the strain increases more rapidly at higher fields. The diffuse x-ray scattering relative to the Bragg reflection increases at high electric fields, while the peak intensity of Bragg reflections simultaneously decreases. The increase of piezoelectricity and diffuse scattering observed at high electric fields are consistent with the softening of phonon modes of $BiFeO_3$ in the proximity of the predicted phase transition.

5.2 Experimental Arrangement

A $BiFeO_3$ thin film with a thickness of 50 nm was prepared for the high field measurement by the research group of Prof. Chang-Beom Eom. The sample was deposited onto an $SrRuO_3$ continuous bottom electrode on an (001)-oriented $SrTiO_3$ substrate by off-axis magnetron sputtering [16]. Pt top electrodes with diameters ranging from 5 to 200 μm were deposited to form $Pt/BiFeO_3/SrRuO_3$ capacitors. The breakdown field for long-duration electric field pulses is on the order of 100 MV/m for typical ferroelectric capacitors [6]. In order to briefly exceed the low-frequency breakdown field without damaging the sample, we used a series of short-duration voltage pulses with duration of 10 to 20 ns [17]. The applied electric fields were along the [001] direction in order to test the prediction that the field would produce a rhombohedral-to-tetragonal phase transition [5]. The charging time of the $BiFeO_3$ capacitors is minimized by reducing the resistance of $SrRuO_3$ bottom electrode and by using small Pt top electrodes. A 50-nm $SrRuO_3$ layer, thicker than typical bottom electrodes, was deposited in this case and the corresponding sheet resistance is 440 Ω. The initial structural transient of the piezoelectric distortion described below occurred with a time constant of 1.4 ns for 25-μm capacitors, corresponding to a small RC time constant as we expected.

The zero-field structure of the $BiFeO_3$ thin film was studied using a laboratory x-ray diffractometer. Incident x-ray was monochromatized by coupled x-ray mirrors and 4-bounce Ge (220) single crystals to produce a beam of Cu $K\alpha_1$ characteristic radiation. Fixed slits of 1/16° or 1/32° were used to define the angular resolution of the detector.

The structure of $BiFeO_3$ in large applied electric fields was studied using time-resolved x-ray microdiffraction at station 7ID-B of the Advanced Photon Source at

Argonne National Laboratory and at beamline BL13XU at the SPring-8 light source, Harima, Japan. At the Advanced Photon Source, x-rays with a photon energy of 10 keV were focused to a spot size of 100-200 nm with a Fresnel zone plate and the diffracted x-rays were detected using an avalanche photodiode or a pixel array detector [18]. Diffraction patterns were acquired using 25-μm capacitors. At SPring-8 12.3 keV x-ray beams were focused to 2.5 μm with a refractive lens [19] and the diffracted x-rays were detected using an avalanche photodiode. The 50-μm capacitors were studied in the experiments at Spring-8 because of the larger x-ray beam size at that particular instrument. The detectors were synchronized to applied electric fields using the gating electronics described in Chapter 2. The transient x-ray diffraction patterns during the course of electric fields were accumulated over thousands of repetition of electric field pulses in order to achieve adequate counting statistics.

5.3 Static Structure of the Epitaxial $BiFeO_3$ Thin Film

Understanding the microscopic structure of $BiFeO_3$ thin films in the zero-field state was the first step in our study. The out-of-plane and in-plane lattice structures of the epitaxial $BiFeO_3$ thin film were characterized by x-ray diffraction measurements. The peak intensity of the $BiFeO_3$ (002) Bragg reflection is at Q_z = 3.086 $Å^{-1}$, as shown in Fig. 5.1(a), corresponding to an out-of-plane lattice parameter of 4.071 Å. The intensity fringes at both small- and large-Q_z side of the Bragg reflection arise from the thickness of $BiFeO_3$ film. The 0.0117 $Å^{-1}$ spacing of the fringes gives a $BiFeO_3$ film thickness of 54 nm. In the (103) reciprocal space map in Fig. 5.1(b), the $SrTiO_3$ reflection is split due to the twinning in the $SrTiO_3$ substrate. The $BiFeO_3$ and $SrRuO_3$ (103) reflections occur at

the value of the in-plane wavevector Q_x as the $SrTiO_3$ substrate, indicating that the $BiFeO_3$ layer is coherently strained to the lattice constant of the substrate.

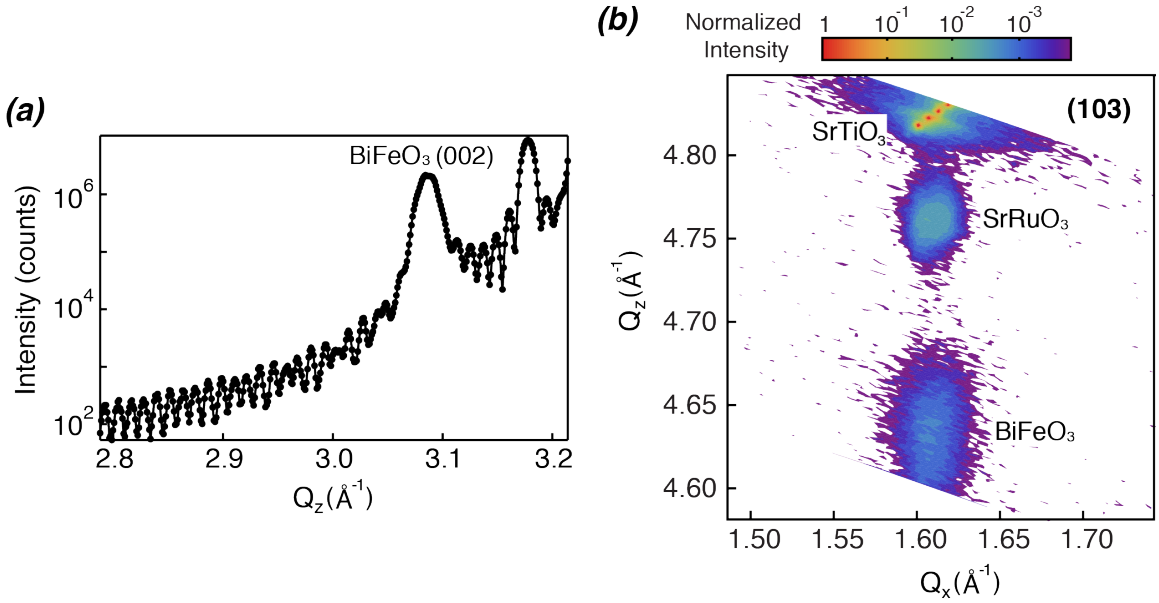

Figure 5.1 (a) Intensity near the $BiFeO_3$ (002) Bragg reflection as a function of out-of-plane wavevector Q_z. The intense reflection at Q_z = 3.177 Å^{-1} arises from the $SrRuO_3$ bottom electrode. (b) Reciprocal space map covering, from bottom to top, the $BiFeO_3$ (103), $SrRuO_3$ (103) and $SrTiO_3$ (103) Bragg reflections. The intensity is normalized to the peak intensity of the $SrTiO_3$ (103) reflection.

The $BiFeO_3$ thin film has a complex polarization domain structure. The $BiFeO_3$ bulk rhombohedral structure is monoclinically distorted under the elastic constrain imposed by the cubic $SrTiO_3$ substrate. The monoclinic distortion can, however, occur within three different crystallographic planes. Following the notation developed by Vanderbilt *et al*. [20], the $BiFeO_3$ thin film studied here has a M_A type monoclinic distortion within the 110-family plane, as evident by the detailed reciprocal spacing mapping near (103) and (113) Bragg reflections in Fig. 5.2. With four equivalent ferroelastic domains, the M_A monoclinic distortion splits the (103) Bragg reflection along Q_z, and splits the (113) Bragg reflection along both Q_z and Q_{xy} [21, 22]. The reciprocal space maps in Fig. 5.2 are not able to resolve all the split peaks. The envelope of the

intensity distribution, however, agrees with the expected peak positions considering the M_A type distortion.

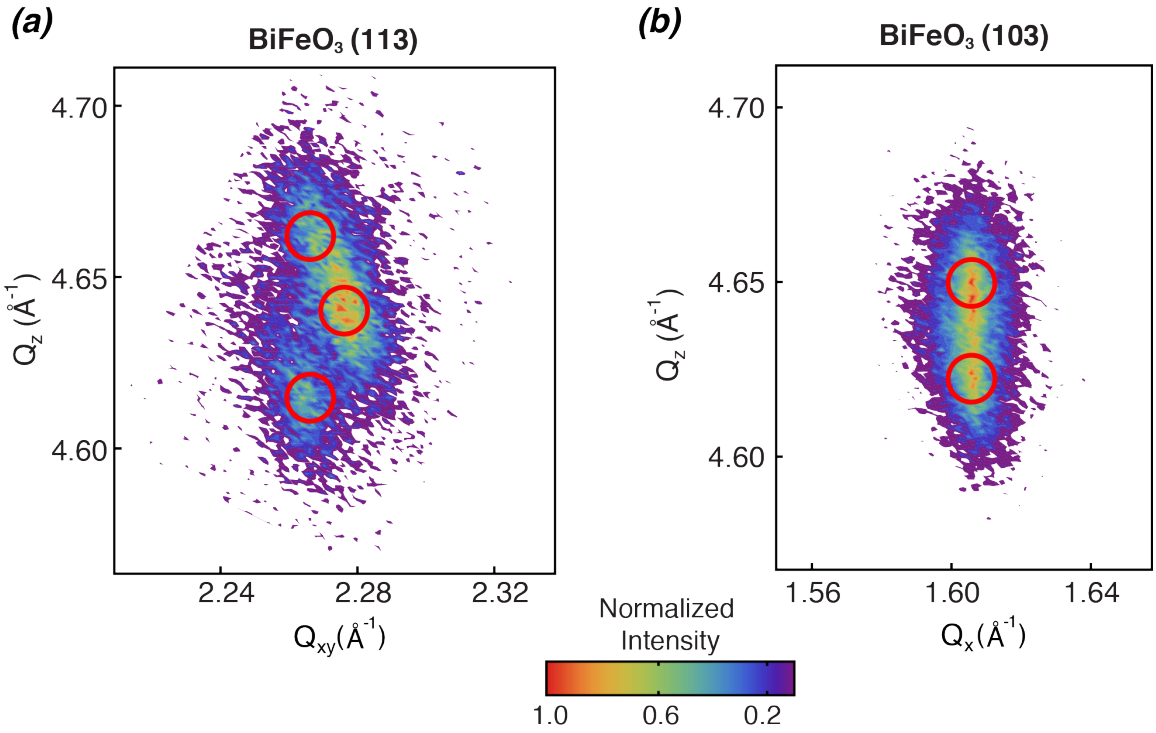

Figure 5.2 Reciprocal space maps near $BiFeO_3$ (a) (113) Bragg reflection and (b) (103) Bragg reflection. The intensity is normalized to peak intensity in each panel. The expected diffraction peaks for M_A phase are shown with red circles.

Despite its complex ferroelastic domain configuration, all of the domains share the same out-of-plane lattice parameter. The in-plane lattice parameter is set by the substrate and is not expected to change under electric fields [17]. In the following sections, we will focus on the field-induced structural change along out-of-plane direction.

5.4 Increase in the Piezoelectricity

Information about the time-dependence of the structure of the $BiFeO_3$ thin film is obtained from time-resolved x-ray diffraction patterns. In Fig. 5.3, diffraction patterns

near the $BiFeO_3$ (002) Bragg reflection are shown at different times during an electric field pulse with a magnitude of 102 MV/m and a duration of 12 ns. The onset of the electric field occurs at time zero, which was experimentally defined as the time where the Bragg reflection started to shift towards smaller Q_z.

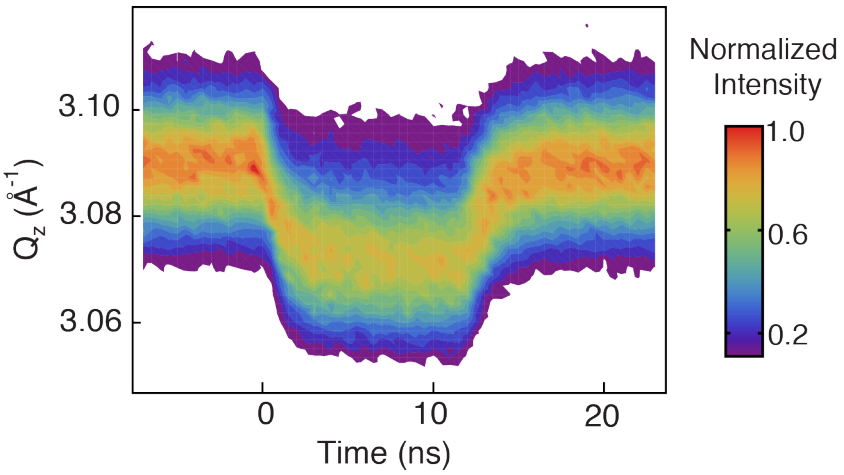

Figure 5.3 $BiFeO_3$ (002) Bragg reflection as a function of time and wavevector Q_z during a 12-ns, 102 MV/m electric field pulse.

The initial peak shift observed in Fig. 5.3 has a characteristic time of 1.4 ns, estimated from by fitting an exponential decay. This characteristic time is governed by the RC time constant of the electric circuit composed of the $BiFeO_3$ capacitor and the $SrRuO_3$ bottom electrode. The rise time of the electric field pulser used in our measurement is 300 ps, far shorter than the observed time constant. The peak position recovered to the zero-field value after the electric field was turned off. Detailed diffraction studies were conducted at a fixed time long after the initial peak shift was complete, at which the electric field within the $BiFeO_3$ thin film has reach a steady state value.

A three-dimensional map of the reciprocal space near the (002) $BiFeO_3$ Bragg

reflection was constructed from a series of diffraction patterns. Experimentally this was accomplished by varying the sample orientation and recording two-dimensional diffraction pattern at each orientation. Fig. 5.4(a) shows the Q_x-Q_z section of the reciprocal space at zero fields and at 17 ns after the onset of a 20-ns electric pulse with a magnitude of 217 MV/m.

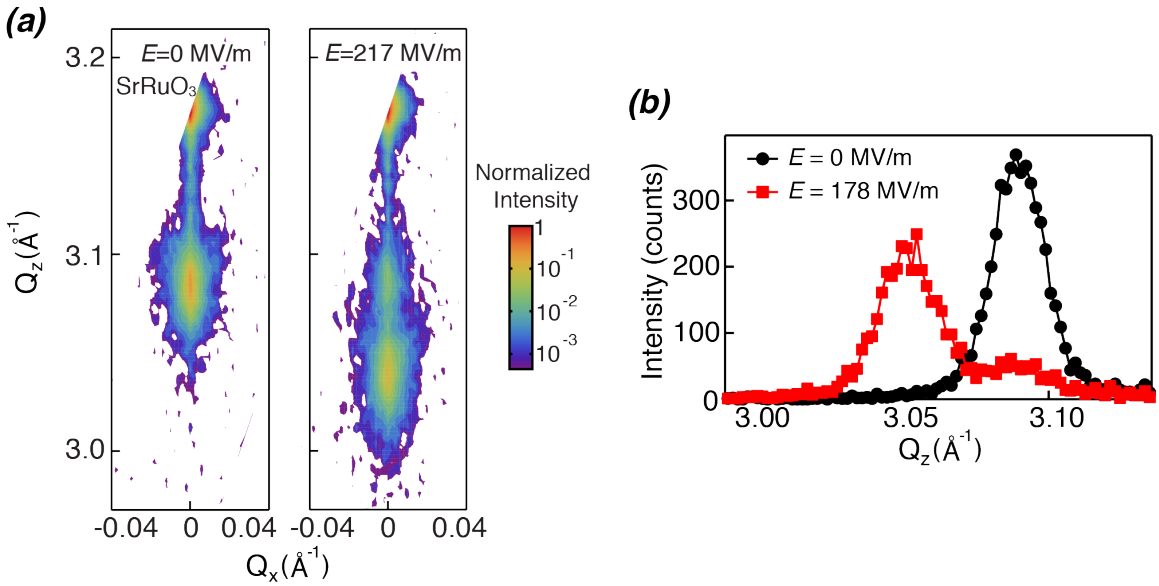

Figure 5.4 (a) Reciprocal space maps near the $BiFeO_3$ (002) Bragg reflection at zero fields (left) and at 217 MV/m (right). The $SrRuO_3$ (002) reflection is cut off as a result of the angular range of the measurement. (b) Intensity as a function of Q_z for the (002) $BiFeO_3$ Bragg reflection at zero fields (circles) and at 170 MV/m (squares).

As was observed in the time-dependent structural response shown in Fig. 5.3, the $BiFeO_3$ (002) Bragg reflection shifts in Fig. 5.4(a) from Q_z = 3.084 Å^{-1} at zero field to Q_z = 3.039 Å^{-1} in an electric field of 217 MV/m. This shift corresponds to a tensile piezoelectric strain of 1.46%. The zero-field value of Q_z is slightly different from the value estimated with millimeter-size x-ray due to the variation of the structure across the lateral extent of the thin film sample. The reciprocal space map in Fig. 5.4(a) also shows that projection of the reflection onto the Q_x axis does not change under applied electric

fields, indicating that the tilt of the $BiFeO_3$ thin film is negligible and has little contribution to the observed peak shift along Q_z.

In addition to the shift of the (002) Bragg reflection in Fig. 5.4, a less intense secondary peak artifact was also observed at the zero-field value of Q_z. This secondary reflection is apparent both in the map in Fig. 5.4(a) and in the line profile of the diffraction pattern in Fig. 5.4(b). A similar secondary peak was observed in $Pb(Zr,Ti)O_3$ thin films [17]. This secondary peak most likely arises from an area of the sample that is not subjected to the applied electric field. Diffraction from areas not exposed to the field can occur either due to partial delamination of top electrodes, or to the illumination of area outside the top electrode by the unfocused portion of the incident x-ray beam. The integrated intensity of the secondary peak dose not depends on the magnitude of applied electric fields, but varies with experimental conditions including the x-ray focusing optics.

The dependence of the piezoelectric strain on the electric field was measured using a series of scans of the intensity as a function of Q_z similar to the scan shown in Fig. 5.4(b). The piezoelectric strain was determined using the shift of the center of the Bragg reflection for each scan. The strain is plotted as a function of the magnitude of the electric field in Fig. 5.5.

The piezoelectric response of $BiFeO_3$ can be divided into two electric field regimes. In the low-field regime, below 150 MV/m, the strain is proportional to the magnitude of the electric field, with a piezoelectric coefficient of 55 pm/V. The linearity of this response and the value of the piezoelectric coefficient are consistent with previous

observations of piezoelectric coefficients of 50-60 pm/V in both bulk $BiFeO_3$ ceramics [23] and in rhombohedral thin films [1, 11]. The strain in the high-field regime higher than 150 MV/m, however, deviates from the linear piezoelectricity. At the highest field we have probed, 281 MV/m, the piezoelectric strain in the $BiFeO_3$ thin film is 2.04%, a factor of 1.3 larger than the value predicted by extrapolating the low-field piezoelectric coefficient. A linear fit to the piezoelectric strain under electric fields above 150 MV/m yields an effective high-field piezoelectric coefficient of 86 pm/V, which is 50% larger in comparison with the low-field piezoelectric coefficient.

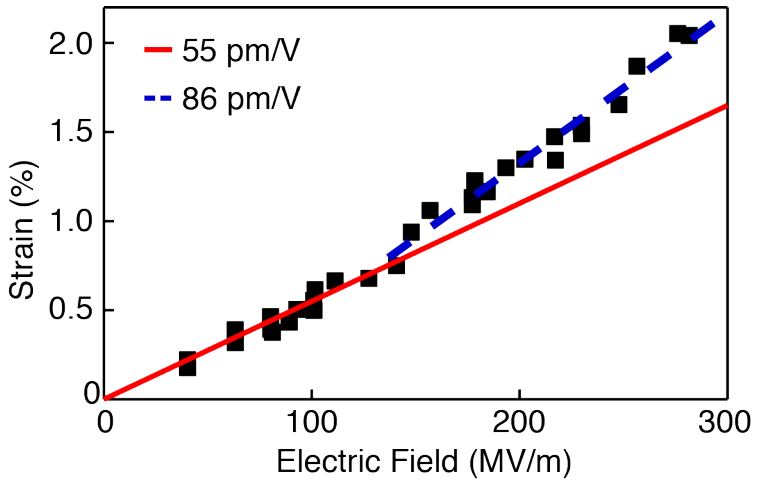

Figure 5.5 Piezoelectric strain as a function of electric field. The solid and dashed lines are linear fits for electric fields less than 150 MV/m and greater than 150 MV/m, respectively.

5.5 Increase in the Diffuse X-ray Scattering

A more detailed structural study was conducted to facilitate the understanding of the enhanced piezoelectric response in the $BiFeO_3$ thin film. In the line profile of the $BiFeO_3$ (002) Bragg reflection along Q_z, shown in Fig. 5.4(b), intensity of the shifted Bragg reflection has a lower intensity than the zero-field reflection. The peak widths in Q_z are unchanged in the electric-field regime we have probed. The in-plane width can be characterized from the rocking curves through the $BiFeO_3$ (002) Bragg reflection along

the [110] direction, as shown for diffraction patterns at zero fields and at 230 MV/m in Fig. 5.6. The angular width of the Bragg component along the in-plane direction is also not changed at high electric fields.

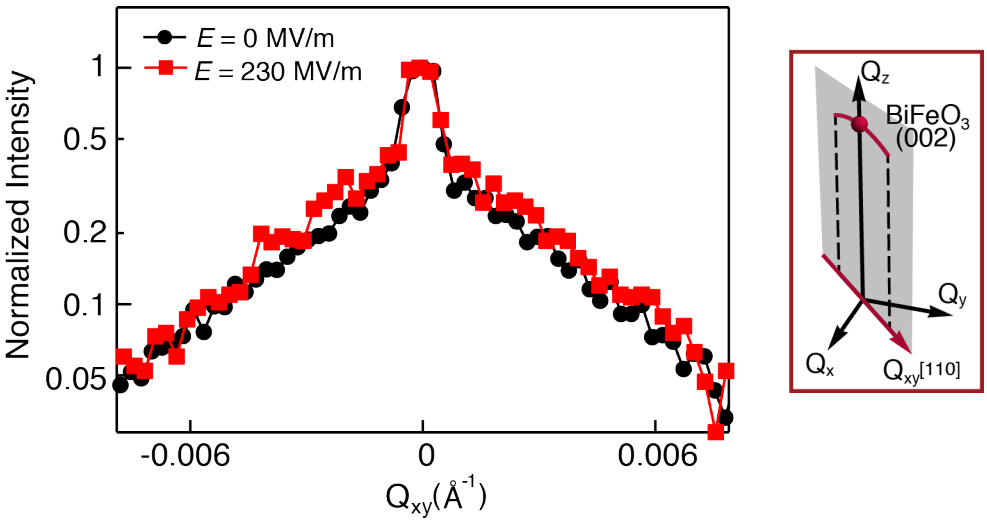

Figure 5.6 Intensity as a function of the in-plane wavevector Q_{xy} for the $BiFeO_3$ (002) Bragg reflection at zero fields (circles) and at 230 MV/m (squares). The geometry of x-ray measurement is shown in the right panel.

Because there is little change in the peak width, the evolution of the integrated intensity of the $BiFeO_3$ (002) Bragg reflection can be estimated using the peak intensity. Fig. 5.7 shows the variation of the peak intensity of the $BiFeO_3$ (002) reflection as a function of the applied electric field. Only the data acquired at Advanced Photon Source was used so that the contribution of the secondary peak to the overall intensity was constant, with approximately 25% of the intensity in the unshifted peak. The peak intensity decreases in applied electric fields. At 281 MV/m, the highest electric field we probed, the peak intensity falls by 70%, a factor of three larger the contribution of the secondary peak. We therefore expect that there is a redistribution of the x-ray intensity from the Bragg component to other regions of the reciprocal space.

We have analyzed the intensity diffuse scattering region of reciprocal space near the (002) Bragg reflection. The intensity of the diffuse x-ray scattering increases relative to the intensity of the Bragg peak as the magnitude of the applied electric field increases. In order to quantify the change in the intensity of the diffuse scattering, we partitioned reciprocal space into two regions: a Bragg region with Q_{xy} less than 2.5×10^{-4} Å^{-1}, and a diffuse region with Q_{xy} between 0.002 and 0.008 Å^{-1}. The ratio of the integrated intensities in these two regions is shown as a function of electric field in Fig. 5.7. At an electric field of 230 MV/m the diffuse scattering in this narrow one-dimensional section of reciprocal space increases by 30% relative to the Bragg peak.

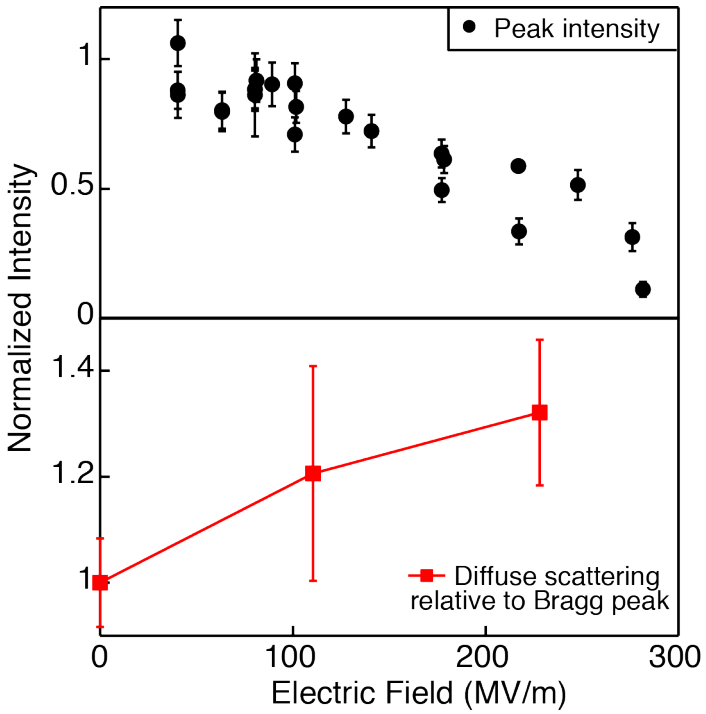

Figure 5.7 (upper panel) Peak intensity of the $BiFeO_3$ (002) Bragg reflection normalized to the zero-field intensity. (lower panel) Ratio of the diffuse scattering intensity to the intensity of the Bragg peak, integrated over the ranges specified in the text. The error bars are derived from counting statistics in the intensity integration.

Integration over the full three-dimensional volume of reciprocal space near the $BiFeO_3$ (002) Bragg reflection shows that the total scattered intensities at zero fields and

217 MV/m electric fields are equal within 6%. This conservation of the intensity indicates that the scattered intensity is redistributed from the Bragg peak into the diffuse component at applied electric fields.

5.6 Connections to Field-induced Phase Transitions

The increase in the piezoelectricity and diffuse x-ray scattering observed in the $BiFeO_3$ thin film is consistent with the softening of the photon modes as the system approaches the predicted phase transition. The softening of the phonon mode and the divergence of dielectric properties are intrinsically linked through the Lyddane–Sachs–Teller relation [24]. The divergence of the piezoelectricity and the associated dielectric and electromechanical properties have been extensively modeled in ferroelectric systems in which crystallographic structural transitions occur [9, 10]. The modification of the functional properties is accompanied by the rotation of the spontaneous polarization, which is required by the symmetry change of the structural phase transition. The piezoelectricity is enhanced near the phase boundaries, but does not retain a high value in phases on either side of the boundary.

Switching between different ferroelastic domain configurations, termed extrinsic factors in Chapter 1, cannot account for the increase in the piezoelectric strain observed in the $BiFeO_3$ thin films at high electric fields. The epitaxial $BiFeO_3$ thin film studied here has four degenerate ferroelastic domains sharing the same out-of-plane lattice parameter. Ferroelastic domain wall movement, however, is not favored by applying electric fields along [001], and therefore has little contribution to lattice deformation.

Another possible extrinsic factor is the 180° domains being reversibly poled by the applied electric field [25]. The key idea of this model is that domains with opposite polarizations show opposite piezoelectric distortion, and that the overall piezoelectricity is modified by changing the volume fraction of domains by applying electric fields.. In the present case, the domains have been preferentially poled during the thin film growth due to the $SrRuO_3$ bottom electrode, with a polarization component parallel with the applied electric fields we used [26]. As a result, no domain switching is expected. In addition, no lattice contraction is observed in the time-resolved x-ray diffraction patterns, indicating that the domains opposite to electric fields have negligible volume fraction.

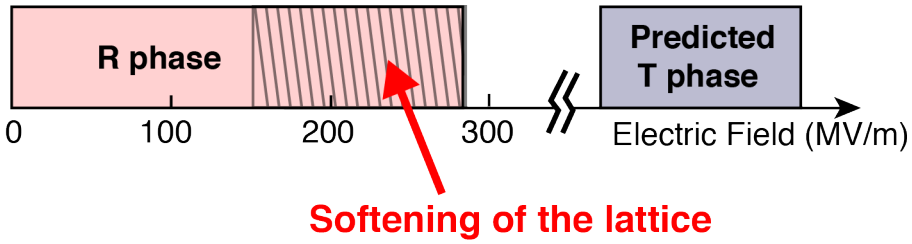

Figure 5.8 Schematic showing relationship of the observed lattice softening to the predicted field-induced phase transition.

The picture of the softened phonon modes is also supported by the x-ray diffuse scattering observations. The intensity of the diffuse scattering is inversely proportional to the frequency of the phonon mode, and consequently x-ray diffuse scattering is particularly sensitive to low-frequency phonons [27]. In the proximity of a ferroelectric phase transition, the soft mode with the lowest optical frequency is further softened and becomes a crucial contribution to the diffuse scattering. Increased x-ray diffuse scattering has been previously observed near phase transitions in $SrTiO_3$ [28] and $TiSe_2$ [29]. In the case of rhombohedral-to-tetragonal phase transition in $BiFeO_3$ thin films, unstable soft

modes are zone-center phonon modes that can be expected to contribute to the diffuse scattering in the range shown in Fig. 5.6.

We propose here that the $BiFeO_3$ thin film was driven to the boundary of the predicted phase transition where the softening of phonon modes occurs. The range of the electric fields in this model is schematically shown in Fig. 5.8. The completion of the transition to the tetragonal phase would require electric fields higher than what we have probed. In the event of a rhombohedral-to-tetragonal phase transition, a diffraction peak associated with the tetragonal phase is expected to appear.

The tetragonal phase can be alternatively stabilized in $BiFeO_3$ thin films under biaxial strain larger than 4%, where an axial ratio of 1.25 has been reported for the tetragonal phase. [15, 30]. This ratio is much larger than what is observed in bulk rhombohedral phase or in the monoclinically distorted phase in epitaxial thin films. The tetragonal phase would produce an x-ray reflection outside the diffraction patterns we have shown. We have performed a detailed reciprocal space mapping in the region of reciprocal space where the diffraction signature of the tetragonal phase is predicted to occur. No diffraction peak was found above the experimental background level at a field of 230 MV/m, and we thus conclude that the system did not reach the tetragonal phase.

In $BiFeO_3$ thin films where a mixture of tetragonal and rhombohedral structures coexist, a tetragonality of 1.07 is measured for the rhombohedral phase [15]. Expanding the $BiFeO_3$ thin film on $SrTiO_3$ to this point requires an out-of-plane strain of 2.5%. By slightly extrapolating our measurements, we predict that this 2.5% strain will be reached at an electric field of 340 MV/m. The attempts to apply higher electric fields beyond the

maximum 281 MV/m shown in Figs. 5.5 and 5.7 resulted in significant sample degradation, including visible changes in top electrodes and electrical breakdown. Based on this estimate, however, we find that the electric fields we have already reached are close to the phase transition and that the fields required for the transformation are within the range of present experimental tools.

Further evidence for the role a phase transition comes from comparing $BiFeO_3$ to other ferroelectric materials. We have previously probed the piezoelectricity of tetragonal $Pb(Zr_{0.2}Ti_{0.8})O_3$ in a similar experiment [17]. Because the rhombohedral-to-tetragonal transition was not available via a tensile expansion in this $Pb(Zr_{0.2}Ti_{0.8})O_3$ system, neither the decrease in the peak intensity of the Bragg reflection nor the large increase in piezoelectricity was observed for electric fields up to 500 MV/m.

5.7 Conclusions

The high-field structure of an epitaxial $BiFeO_3$ thin film, with a zero-field structure on the rhombohedral side of phase diagram, was studied with time-resolved x-ray microdiffraction. Increases in the piezoelectric strain and in the relative intensity of x-ray diffuse scattering in comparison with the Bragg reflection were observed at electric fields higher than 150 MV/m. These observations are consistent with the softening of phonons near the predicted rhombohedral-to-tetragonal phase transition in this system. The appearance of the tetragonal phase would require larger electric fields than what we have probed. We have demonstrated, however, high electric fields provides means to tune and test the properties of $BiFeO_3$ under a wide range of structural configuration without artifacts associated with the sample fabrications on different substrates.

5.8 References

[1] J. Wang *et al.*, "*Epitaxial $BiFeO_3$ Multiferroic Thin Film Heterostructures,*" Science **299**, 1719 (2003).

[2] R. Ramesh, and N. A. Spaldin, "*Multiferroics: Progress and Prospects in Thin Films,*" Nature Mater. **6**, 21 (2007).

[3] H. W. Jang *et al.*, "*Strain-induced Polarization Rotation in Epitaxial (001) $BiFeO_3$ Thin Films,*" Phys. Rev. Lett. **101**, 107602 (2008).

[4] D. Sando *et al.*, "*Crafting the Magnonic and Spintronic Response of $BiFeO_3$ Films by Epitaxial Strain,*" Nature Mater. **12**, 641 (2013).

[5] S. Lisenkov, D. Rahmedov, and L. Bellaiche, "*Electric-Field-Induced Paths in Multiferroic $BiFeO_3$ from Atomistic Simulations,*" Phys. Rev. Lett. **103**, 047204 (2009).

[6] J. F. Scott, "*Ferroelectric Memories*" (Springer, 2000).

[7] S. Nakashima *et al.*, "*X-ray Diffraction Study of Polycrystalline $BiFeO_3$ Thin Films under Electric Field,*" Appl. Phys. Lett. **93**, 042907 (2008).

[8] M. Ahart *et al.*, "*Origin of Morphotropic Phase Boundaries in Ferroelectrics,*" Nature **451**, 545 (2008).

[9] D. Damjanovic, "*Comments on Origins of Enhanced Piezoelectric Properties in Ferroelectrics,*" IEEE. T. Ultrason. Ferr. **56**, 1574 (2009).

[10] M. Iwata, and Y. Ishibashi, "*Phenomenological Theory of Morphotropic Phase Boundary with Monoclinic Phase in Solid-solution Systems of Perovskite-type Oxide Ferroelectrics,*" Jpn. J. Appl. Phys. 1 **44**, 3095 (2005).

[11] J. X. Zhang *et al.*, "*Large Field-induced Strains in a Lead-free Piezoelectric Material,*" Nature Nanotech. **6**, 97 (2011).

[12] S. Fujino *et al.*, "*Combinatorial Discovery of a Lead-free Morphotropic Phase Boundary in a Thin-film Piezoelectric Perovskite,*" Appl. Phys. Lett. **92**, 202904 (2008).

[13] S. E. Park, and T. R. Shrout, "*Ultrahigh Strain and Piezoelectric Behavior in Relaxor Based Ferroelectric Single Crystals,*" J. Appl. Phys. **82**, 1804 (1997).

[14] B. Noheda *et al.*, "*Electric-field-induced Phase Transitions in Rhombohedral $Pb(Zn_{1/3}Nb_{2/3})_{1-x}Ti_xO_3$,*" Phys. Rev. B **65**, 224101 (2002).

[15] R. J. Zeches *et al.*, "*A Strain-Driven Morphotropic Phase Boundary in $BiFeO_3$,*" Science **326**, 977 (2009).

[16] R. R. Das *et al.*, "*Synthesis and Ferroelectric Properties of Epitaxial $BiFeO_3$ Thin Films Grown by Sputtering,"* Appl. Phys. Lett. **88**, 242904 (2006).

[17] A. Grigoriev *et al.*, "*Nonlinear Piezoelectricity in Epitaxial Ferroelectrics at High Electric Fields,"* Phys. Rev. Lett. **100**, 027604 (2008).

[18] T. Ejdrup *et al.*, "*Picosecond Time-resolved Laser Pump/X-ray Probe Experiments Using a Gated Single-photon-counting Area Detector,"* J. Synchrot. Radiat. **16**, 387 (2009).

[19] O. Sakata *et al.*, "*Beamline for Surface and Interface Structures at SPring-8,"* Surf Rev Lett **10**, 543 (2003).

[20] D. Vanderbilt, and M. H. Cohen, "*Monoclinic and Triclinic Phases in Higher-order Devonshire Theory,"* Phys. Rev. B **6309**, 094108 (2001).

[21] R. Guo *et al.*, "*Origin of the High Piezoelectric Response in $PbZr_{1-x}Ti_xO_3$,"* Phys. Rev. Lett. **84**, 5423 (2000).

[22] H. M. Christen *et al.*, "*Stress-induced R-M_A-M_C-T Symmetry Changes in $BiFeO_3$ Films,"* Phys. Rev. B **83**, 144017 (2011).

[23] V. V. Shvartsman, W. Kleemann, R. Haumont, and J. Kreisel, "*Large Bulk Polarization and Regular Domain Structure in Ceramic $BiFeO_3$,"* Appl. Phys. Lett. **90**, 172115 (2007).

[24] R. Lyddane, R. Sachs, and E. Teller, "*On the Polar Vibrations of Alkali Halides,"* Phys. Rev. **59**, 673 (1941).

[25] S. Trolier-McKinstry, N. Bassiri Gharb, and D. Damjanovic, "*Piezoelectric Nonlinearity due to Motion of 180° Domain Walls in Ferroelectric Materials at Subcoercive Fields: A Dynamic Poling Model,"* Appl. Phys. Lett. **88**, 202901 (2006).

[26] S. H. Baek *et al.*, "*Ferroelastic Switching for Nanoscale Non-volatile Magnetoelectric Devices,"* Nature Mater. **9**, 309 (2010).

[27] S. R. Andrews, "*X-Ray-Scattering Study of the R-point Instability in $SrTiO_3$,"* J. Phy. C: Solid State Phys. **19**, 3721 (1986).

[28] M. Holt *et al.*, "*Dynamic Fluctuations and Static Speckle in Critical X-Ray Scattering from $SrTiO_3$,"* Phys. Rev. Lett. **98**, 065501 (2007).

[29] M. Holt *et al.*, "*X-ray Studies of Phonon Softening in $TiSe_2$,"* Phys. Rev. Lett. **86**, 3799 (2001).

[30] H. Bea *et al.*, "*Evidence for Room-Temperature Multiferroicity in a Compound with a Giant Axial Ratio,"* Phys. Rev. Lett. **102**, 217603 (2009).

6 Ultrafast Structural Modification in Epitaxial $BiFeO_3$ Thin Films under Femtosecond Optical Excitation

6.1 Introduction

The interplay between structural, electronic and magnetic properties of multiferroic complex oxides creates the potential to manipulate functional properties using a variety of applied fields [1, 2]. Changes in the crystallographic structure of the prototypical multiferroic $BiFeO_3$ have been studied with respect to a number of experimental variables including chemical doping [3], epitaxial stress [4], and applied electric fields [5]. The recent discovery of a bulk photovoltaic effect in $BiFeO_3$ has led to efforts to understand the effects of optical fields on the ferroelectric, magnetic, and structural degrees of freedom [6, 7]. A static lattice expansion of $BiFeO_3$, for example, has been reported under continuous optical illumination [8]. These studies of lattice deformation and symmetry transitions in illuminated $BiFeO_3$, however, have been limited to quasi-equilibrium structural properties and have lacked crystallographic information. The dynamics of the photoinduced structural modification have not yet been determined. This chapter focuses on the mechanisms of the generation and relaxation of photoinduced structural changes in $BiFeO_3$ and on the timescales of the associated physical processes.

Femtosecond optical excitation can rapidly drive a material into a state far from equilibrium and hence provides a way to excite a wide range of ultrafast structural phenomena [9]. Such photoinduced structural phenomena include optical, electronic and thermal effects, each with different characteristic timescales, as summarized in Fig. 6.1(a). For polar materials including multiferroics, the shift current is often the

dominating structural effect among other second-order optical effects including the injection current and optical rectification [10, 11]. The shift current occurs when the centers of positive and negative charges are offset along a polar direction. Above-bandgap optical excitation modifies the carrier distribution in valence and conduction bands, leading to an instantaneous change of the center of carriers [11]. This instantaneous electric field, termed as the shift current, deforms the lattice structure of ferroelectrics due to the polarization-structure coupling. The timescale of the shift current effect is approximately 5 ps, depending on the duration of optical pulses [12].

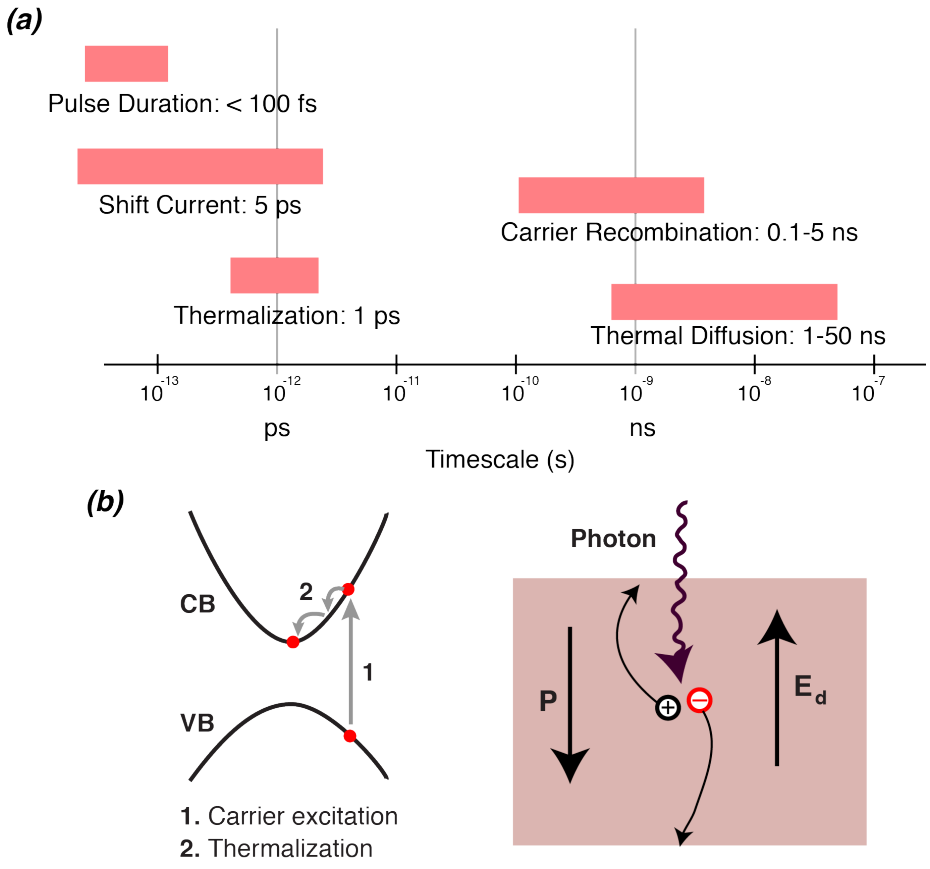

Figure 6.1 (a) Characteristic timescales of various optical, electronic and thermal effects. (b) Schematic of carrier excitation and thermalization due to carrier-phonon scattering (left panel). Effect of the depolarization field on photoinduced free carriers (right panel).

The polarization-structure coupling drives further structural effects as the photoinduced carriers are displaced by the internal electric field of ferroelectrics. One widely accepted model in ferroelectric thin films is that the strain arises due to the screening of the depolarization field by the mobile charge carriers, as schematically shown in Fig. 6.1(b) [12, 13]. This effect is particularly important in ultrathin films, where the internal field can have a magnitude on the order of 100 MV/m [14]. The process of electron-hole recombination defines the timescale of this carrier effect. The typical value is 0.1 to 5 ns.

A deformation of the lattice can also be induced by an increase in the temperature due to the energy deposited by optical pulses. After the initial carrier excitation, the excess photon energy above the bandgap is rapidly transferred from hot electrons to lattice as a result of a thermalization process involving the carrier-phonon scattering (Fig. 6.1(b)) [15]. The thermalization occurs as a timescale of approximately 1 ps. The lattice could gain additional energy as the subsequent carrier recombination occurs via non-radiative processes, including Auger process and defect-mediated recombination [16]. In thin films, the thermal energy is dissipated via thermal diffusion into the substrate. Typically the temperature increase induced by the optical pulse has decreased to less than 1 K over at time on the order of 1-50 ns, much longer than the optical and electronic effects (Fig. 6.1).

The structural changes induced by optical excitation also produce a spatially inhomogeneous strain. Experimental understanding of the optical structural modification has been so far limited to a macroscopic scale, which has not provided insight into the local variation of the magnitude of the photoexcited strain. The local structural variation

is important, however, in a series of properties. Ferroelectric polarization switching, for example, can be induced by a large strain gradient, as reported in a $BaTiO_3$ film [17]. The structural sensitivity of x-ray probe makes it possible to resolve the spatial variation of the strain developed in multiferroics in response to optical excitation.

In this chapter, the evolution of the photoinduced lattice distortion is systematically studied in a series of $BiFeO_3$ thin films using *in-situ* x-ray microdiffraction. We found that above-bandgap optical pulses lead to a large structural expansion in $BiFeO_3$ that develops over a period of time less than the 100-ps time resolution of the diffraction measurement. The magnitude of the peak strain following the optical excitation is proportional to surface-transmitted fluence, reaching 0.5% at 6.1 mJ/cm^2. The characteristic timescale for the strain relaxation is on the order of 1 ns, and increases to longer times as the film thickness increases. The fluence-dependence and the characteristic times of the lattice expansion are consistent with a model that includes both the screening of the depolarization field in the presence of photon-induced carriers and a relatively weak thermal component. We also found that at a surface-transmitted fluence higher than 4.5 mJ/cm^2, the Bragg reflection is broadened along the surface normal direction. A kinematical x-ray simulation supports a structural model in which the Bragg peak broadening arises from a large in-plane strain inhomogeneity.

6.2 Experimental Arrangement

$BiFeO_3$ thin films with thickness of 4 nm, 8 nm, 20 nm and 35 nm were prepared on 001-orientated $SrTiO_3$ substrates by reactive molecular-beam epitaxy by Prof. Darrell Schlom's group at Cornell University [18]. Control of the stoichiometry of the $BiFeO_3$ layer is achieved using an adsorption-controlled codeposition procedure, by supplying an

overpressure of bismuth and utilizing the differential vapor pressures between bismuth oxides and $BiFeO_3$. Distilled ozone was used to create a background oxidant pressure of 1×10^{-6} Torr and the substrate was maintained at a constant temperature of 610 °C. Unlike the samples used in the applied electric field discussed in previous chapters, no oxide or metal electrodes are integrated in these $BiFeO_3$ thin films, in order to minimize the thermal artifacts arising from the optical absorption at the electrodes.

Time-resolved x-ray diffraction studies were conducted at station 7ID-C of the Advanced Photon Source (APS) at Argonne National Laboratory. The 50-fs duration optical pulses were provided by a Ti:sapphire laser at a fundamental wavelength of 800 nm [19]. The repetition rate of the oscillator is 88 MHz, phase locked to a frequency-divided radio frequency signal derived from the accelerator cavities of the APS storage ring. The laser pulses were amplified via a chirp-pulsed amplifier with a maximum average power of 2.5 W at a repetition rate of 5 kHz. These pulses were subsequently frequency doubled to a wavelength of 400 nm so that the photon energy was larger than the 2.6 eV bandgap of $BiFeO_3$ [20]. The laser pulses were delivered to a 0.67×1 mm^2 FWHM spot on the $BiFeO_3$ surface at an incident angle of 15° off the surface normal.

We define the surface-transmitted fluence to be the total optical energy per unit area in each pulse that is transmitted through the $BiFeO_3$/air interface. This definition allows us to discuss samples with different thicknesses or optical reflectivities without ambiguity. The fluences given in this chapter uniformly follow this definition. The surface-transmitted fluence F_t is computed following

$$F_t = \frac{P(1-R)}{f_{rep} \cdot A}, \tag{6.1}$$

where P and f_{rep} are the average incident power and repetition rate of laser pulses, respectively. A is the optically illuminated area. R is reflectivity, found to be 0.57 for these experiments. We observe that there was negligible variation of the reflectivity as a function of the film thickness. The fluence absorbed by the $BiFeO_3$ layer F_a is related to transmitted fluence by

$$F_a = F_t(1 - \exp(-d / L)) . \tag{6.2}$$

The exponential term accounts for the optical transmission, with d and L being the thickness of the film and absorption length, respectively. The optical absorption length for $BiFeO_3$ is 32 nm at a wavelength of 400 nm [20]. As a result, the energy absorbed by thinner samples will be far less than the total transmitted fluence.

X-ray pulses with a photon energy of 12 keV were focused by Kirkpatrick-Baez mirrors to a 50 μm diameter spot at the center of the area illuminated by the laser. Diffracted x-rays were collected with a gated two-dimensional detector. In the gated mode, the detector records only the signals from x-rays with appropriate time delay with respect to the laser pulses. Each x-ray diffraction pattern is accumulated over a series of either 5000 or 10000 repetitions of laser excitation to achieve a sufficient counting statistics. The larger number of pulses was required for the thinnest 4 nm-thick samples. The time resolution of the x-ray diffraction is set by the 100-ps FWHM of the x-ray pulses.

The synchronization of x-ray pulses to laser pulses was achieved via two stages with electronically adjustable delays. The strategy was slightly different than the methods employed with electric-field excitation that were discussed in Chapter 3 and 4. With optical excitation, a generator is used to delay the radio frequency signal to which the

laser oscillator is phase locked. The delay of the phase-lock signal can vary the overall delay within a range of 11 ns, the fundamental repetition period of the laser oscillator. A second delay generator is used in synchronization with the chirp-pulsed amplifier to achieve a larger delay range. The second delay generator is used to pick an adjacent 5 kHz subset of the 88 MHz laser pulses.

The thermal expansion of the $BiFeO_3$ films was studied using a separate temperature-dependent diffraction measurement, conducted with a laboratory x-ray diffractometer. A resistive heating stage was constructed and used to heat the 35-nm-thick $BiFeO_3$ layer. The temperature was monitored using a thermocouple connected to the heater. This arrangement allowed precise variation of the sample temperature between room temperature to 450 K. The experimental high-temperature limit was set by heat transfer from the heating stage to surrounding ambient environment. X-ray reflections from the $BiFeO_3$ film and $SrTiO_3$ substrate were measured at each temperature step during the study.

6.3 Area-Averaged Photoinduced Strain and its Relaxation

The femtosecond laser pulses induce an expansion of the $BiFeO_3$ lattice along the surface normal. Fig. 6.2(a) shows the optically induced shift of the (002) Bragg reflection for the 35-nm $BiFeO_3$ thin film. The maximum shift of the Bragg peak occurs 100 ps after laser pulse. The strain averaged over the probed area is estimated from the shift of the center of mass of the Bragg reflection. The photoinduced strain is 0.42% at the maximum surface-transmitted laser fluence of 6.1 mJ/cm^2. This strain is two orders of magnitude larger than the strain reported in $BiFeO_3$ single crystals under continuous light

illumination [8]. At a later time, as for 0.5 ns shown in Fig. 6.2(a), the Bragg peak shifts back toward the laser-off position in reciprocal space.

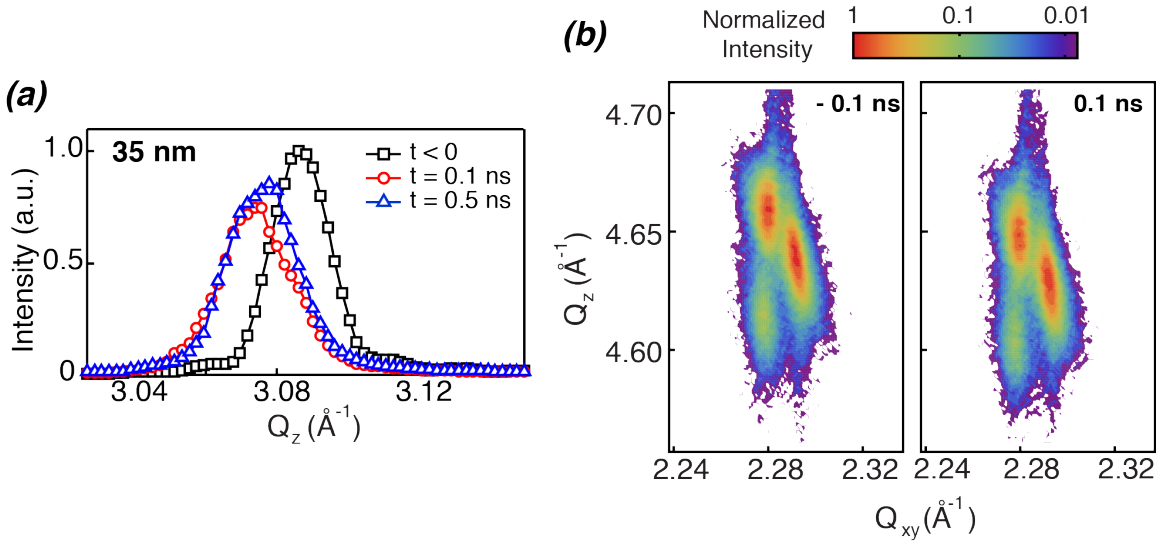

Figure 6.2 Time-resolved diffraction patterns for 35-nm $BiFeO_3$ thin film under 50-fs optical laser pulses with a wavelength of 400 nm. (a) (002) Bragg reflections at times before (square) and 0.1 ns (circle) and 0.5 ns (triangle) after laser pulses with a transmitted fluence of 6.1 mJ/cm^2. (b) Reciprocal space maps near (113) Bragg reflections at times 0.1 ns before and 0.1 ns after laser pulses, at a transmitted fluence of 3.4 mJ/cm^2.

The in-plane lattice parameter is unchanged by optical excitation. The (113) $BiFeO_3$ Bragg reflections of the 35-nm-thick $BiFeO_3$ layer were studied at times 100 ps before and 100 ps after the laser pulses, as shown in Fig 6.2(b). The (113) reflections are split along both Q_z and Q_{xy} as a result of the presence of ferroelastic domains. Each domain has a M_A-type monoclinic distortion within 110-family planes. After the optical excitation, all of the (113) peaks shift to lower Q_z, indicating an out-of-plane expansion of lattice with the same magnitude for all ferroelastic domains. The elastic constraint provided by the $SrTiO_3$ substrate, however, is sufficiently strong to clamp the in-plane lattice parameter of $BiFeO_3$, and no change of Q_{xy} is observed. We thus focus on only the out-of-plane structural changes in the following discussion.

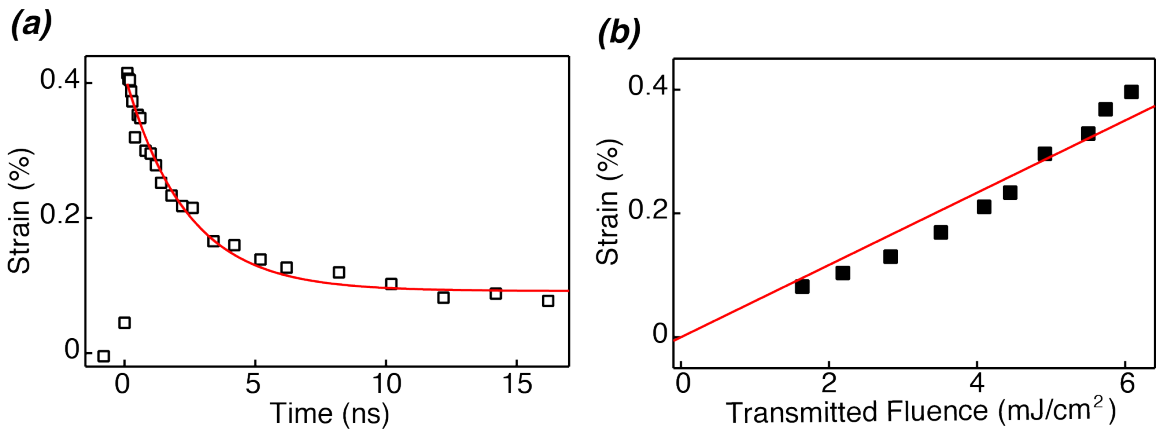

Figure 6.3 (a) The strain of the 35-nm $BiFeO_3$ thin film as a function of time after the laser excitation at a surface-transmitted fluence of 6.1 mJ/cm^2 at time 0. The line is the result of an exponential fit with a constant offset. (b) The strain of the 35-nm $BiFeO_3$ thin film as a function of transmitted fluence acquired at 100 ps after the 50-fs laser pulses. A linear fit is shown together with the data points as a solid line.

The photoinduced strain relaxes as time elapses, as is evident from the comparison of Bragg reflections at different times in Fig. 6.2(a). The detailed relaxation process is captured by the plot of the measured strain as a function of time curve in Fig. 6.3(a). During the first 5 ns after the optical excitation, the magnitude of strain drops to 0.14%, a third of the maximum value. At times longer than 5 ns, the strain relaxes at a much slower rate. We therefore adopt an empirical exponential fit with a constant offset at long times to approximate the relaxation of photoinduced strain. The characteristic time from the best fit is 2.3 ns for the initial fast relaxation process. The maximum strain is proportional to the surface-transmitted fluence in the regime we probed. The dependence of the strain on the fluence is plotted in Fig. 6.3(b).

The photoinduced strain originates from both electronic and thermal effects. Optical effects, including the shift current [11], have a timescale on the order of a few picoseconds and therefore can be neglected over the nanosecond time regime studied here. In order to study the remaining possible origins of the optically induced strain, we

first consider the contribution of the laser heating. Heat is initially deposited into the $BiFeO_3$ thin film via the carrier thermalization process, and is subsequently dissipated through thermal diffusion into $SrTiO_3$ substrate. The temperature rise ΔT of the $BiFeO_3$ thin film can be estimated by assuming that only excess photon energy above the bandgap E_g available to heat $BiFeO_3$ layer. The temperature rise is

$$\Delta T = \frac{E_p - E_g}{E_p} \cdot \frac{F_a}{d \cdot c_p \cdot \rho}, \tag{6.3}$$

where E_p is the photon energy, 3.1 eV. c_p and ρ are the specific heat and density of $BiFeO_3$, respectively, with values of 0.3 J/(g·K) and 8.34 g/cm^3 [21]. The temperature rise estimated in this way 74 K at a transmitted fluence of 6.1 mJ/cm^2.

A separate x-ray diffraction measurement was conducted to quantify the thermal expansion of $BiFeO_3$. In this experiment, the $BiFeO_3$ thin film was heated together with the $SrTiO_3$ substrate. The change in the lattice parameter was measured using the shifts of the (001) and (002) Bragg reflections as a function of temperature in the range from 300 to 430 K (Fig. 6.4). The linear thermal expansion coefficients of $BiFeO_3$ and $SrTiO_3$ determined from the linear fit to Fig. 6.4 are 1.18×10^{-5} K^{-1} and 0.64×10^{-5} K^{-1}, respectively. The value for $SrTiO_3$ single-crystal substrate is slighter smaller with 0.7-1.1 $\times 10^{-5}$ K^{-1} found in $SrTiO_3$ ceramics [22]. The linear thermal expansion coefficient of $BiFeO_3$ is within the range of values found in $BiFeO_3$ ceramics [23].

In the optical-excitation experiment, however, only the $BiFeO_3$ film was heated so the coefficients of thermal expansion derived from Fig. 6.4 must be adjusted to account for the different mechanical boundary conditions. The mechanical constraint imparted by the room-temperature $SrTiO_3$ substrate on the hot $BiFeO_3$ film leads to an additional out-

of-plane expansion following the Hooke's law under biaxial stress

$$\varepsilon_{out} = \frac{2\nu}{1-\nu}\varepsilon_{in}, \tag{6.4}$$

where ε_{out}, ε_{in} and ν are the out-of-plane strain, in-plane strain and Poisson's ratio. Using Poisson's ratio of 0.34 for $BiFeO_3$ [24], the effective thermal expansion coefficient along out-of-plane direction is 1.82×10^{-5} K^{-1}.

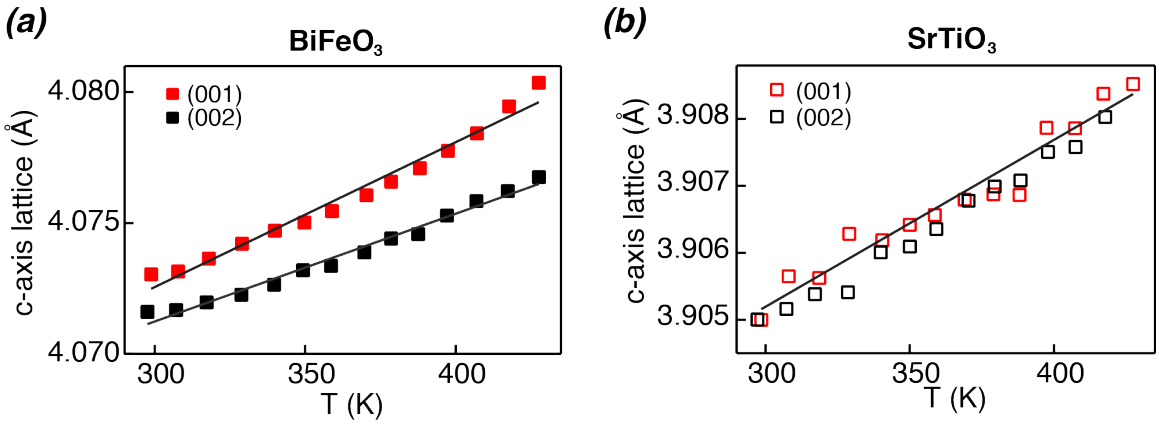

Figure 6.4 Lattice parameters along c-axis of $BiFeO_3$ (a) and $SrTiO_3$ (b) in the 35-nm $BiFeO_3$ thin film on $SrTiO_3$ substrate as a function of temperature. The lattice parameters are estimated from both (001) and (002) Bragg reflections. Results of linear fit to lattice parameter vs. temperature curves are shown as lines.

The heating due to the few-picosecond thermalization of the excited electrons leads to a temperature rise of 74 K and a corresponding thermal expansion of 0.13%. This thermal effect accounts for only one third of the peak strain of 0.42%. The thermal expansion decays from 0.13% to 0.08% by 15 ns after the laser pulse. After this timescale, electronic effect can be ignored.

Attempts to model the decay of thermal expansion considering only thermal diffusion between $BiFeO_3$ and $SrTiO_3$, however, require that the interfacial thermal conductance be varied as an adjustable fitting parameter. The values of the fit give interfacial thermal conductance that is two orders of magnitude lower than similar

interfaces. We therefore hypothesize that other processes are responsible for supplying additional heat to $BiFeO_3$ lattice, including non-radiative carrier recombination.

A major part of the peak strain under optical excitation arises from a piezoelectric effect associated with photon-induced carriers. The drift of excited carriers in the depolarization field creates a time-dependent electric field that drives the c-axis piezoelectric expansion. The magnitude of the transient electric field ΔE can be estimated using the change of the polarization as in

$$\Delta E = \frac{\Delta P}{\varepsilon_0 \varepsilon} = \frac{N \cdot q \cdot \Delta z}{\varepsilon_0 \varepsilon}, \tag{6.5}$$

where ε_0 and ε are the vacuum permittivity and relative permittivity of $BiFeO_3$, respectively. The change of the polarization ΔP is a product of carrier concentration N, electric charge of a single electron q and electron-hole displacement Δz.

Equation (6.5) has two important implications. First, the strain is proportional to overall carrier density and therefore the pump fluence, which could explain the linear fluence scaling of the strain shown in Fig. 6.3(b). Second, the timescale of the strain is expected to follow the timescale of the carrier recombination. In the plot of strain as a function of time shown in Fig. 6.3(a), the timescale of the strain relaxation is 2.3 ns for 35-nm $BiFeO_3$ thin film, consistent with the lifetime of charge carriers measured in a separate experiment using optical absorption spectroscopy [25].

Further insight into the model of carrier-mediated photoinduced strain is provided by a quantitative analysis. After subtracting the thermal component, the carrier contribution to the maximum strain of 0.42% is approximately 0.29%. Using a piezoelectric coefficient of 54 pm/V [5], we can estimate that the corresponding transient

electric field is 54 MV/m, within the range of the depolarization field found in ferroelectric thin films [14]. We can expect that at high fluence, the photoinduced strain would saturate after the depolarization field is completely screened, similar to the study in $PbTiO_3$ thin film [12]. This saturation, however, is not observed in the fluence range we have probed.

We can also estimate the electron-hole separation. Using a dielectric constant of 100 [26], the polarization due to optical excitation is approximately 5 $\mu C/cm^2$, 8% of the spontaneous polarization of 60 $\mu C/cm^2$ [27]. This carrier density is approximately 2.3×10^{21} cm^{-3} at a transmitted fluence of 6.1 mJ/cm^2 under the assumption that each photon generates an electron-hole pair in $BiFeO_3$. Substituting these parameters into Eq. 6.5, the associated separation of electrons and holes separation is found to be only 1.2 Å. The short electron-hole separation indicates that the photoinduced strain can occur at a much faster timescale beyond the temporal resolution we have in the present case.

6.4 Thickness Dependence of Strain Relaxation

More details of the carrier dynamics can be determined from a systematic study of a series of $BiFeO_3$ thin film with thickness ranging from 4 to 35 nm. Fig. 6.5 shows the time-dependence of the optically induced strain in four $BiFeO_3$ thin films for a wide range of laser fluences. For each film thickness, the maximum strain at the highest transmitted fluence is approximately 0.5%, despite that the thickness is varied by one order of magnitude. This weak thickness dependence of strain is consistent with the proportionality of strain to carrier density. The absorption length of $BiFeO_3$ under 400-nm wavelength laser is 32 nm, comparable or larger than the film thickness. As a result,

for the same transmitted fluence, the absorbed fluence is larger in thicker films. The larger absorbed photon energy, however, is offset by the larger thickness when computing the carrier density. Considering each photon generating an electron-hole pair, the upper bound for the carrier concentration is 2.3×10^{21} cm^{-3} for 35-nm film, and 50% larger in 4-nm film at the highest fluence. The photoinduced strain is therefore expected to be on the same order, as we observed.

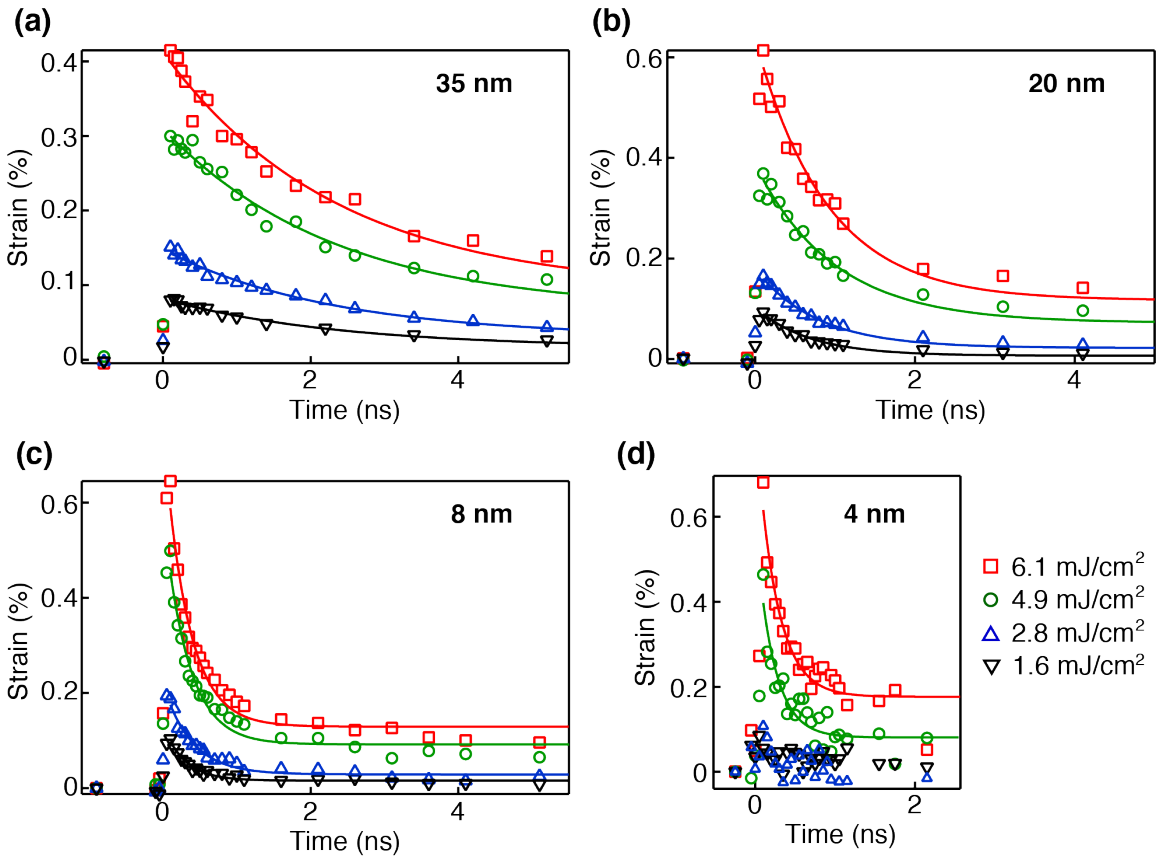

Figure 6.5 Strain vs. time curves for $BiFeO_3$ thin films with thickness of 35 nm, 20 nm, 8 nm and 4 nm. In each film, four sets of data are shown, acquired at different transmitted fluence, from 1.6 (downward triangles), 2.8 (upward triangles), 4.9 (circles) to 6.1 mJ/cm^2 (squares). Data points acquired after laser excitation are fit with exponential decay function (lines).

The timescale of the strain relaxation exhibits a strong dependence on the film thickness. Using a procedure similar to the analysis of the data shown in Fig. 6.3(a), we

have extracted the characteristic time associated with the decay strain using the strain vs. time curves shown in Fig. 6.5 using an exponential fit plus a constant offset. The characteristic time for relaxation depends weakly on the transmitted fluence for each thin film, but increases with the increase of the thickness of the $BiFeO_3$ thin film. The characteristic time for the 35-nm film was found to be 2.3 ns. In contrast, the 4-nm film has a characteristic time of 0.25 ns, one order of magnitude smaller.

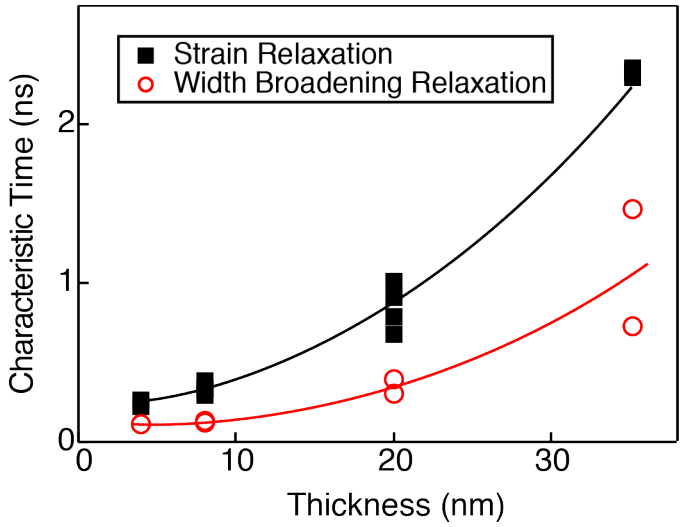

Figure 6.6 Characteristic time of the relaxation of strain (squares) and peak broadening (circles) as a function of the film thickness. Guide lines are shown together with data points.

Thermal contribution is unlikely the main source of the thickness dependence of the strain relaxation. The driving force for thermal dissipation, the thermal gradient at the film/substrate interface, is similar for all the films, since the temperature rise of $BiFeO_3$ is determined by the thermal energy per volume with weak thickness dependence. The initial thermal energy deposited into the $BiFeO_3$ film, however, is proportional to the absorbed photon power, and hence smaller for thinner film. Together we expect the thermal relaxation is more rapid in thinner film, a trend we have observed. However, the maximum thermal energy only contributes to a third of the total lattice strain as we

estimated in the early section. We therefore hypothesize that the thickness dependence of the strain relaxation has a non-thermal origin.

The thickness dependence of the strain relaxation observed here indicates that there is a thickness dependence of the carrier recombination. The relaxation of excess carriers in semiconductors is given by the solution of a diffusion equation. In practice, the decay of the details is dominated by the diffusion solution with the longest time, the principle mode [28]. Due to the large defect concentration at the surface, the surface recombination is often the major contribution to the principle mode in comparison with the bulk recombination, particular in thin films. We consider a model here in which the carrier diffusion limits the recombination process at the surfaces, the timescale is then

$$\frac{1}{\tau} = \frac{D\pi^2}{d^2}. \tag{6.6}$$

Here τ and D are the timescale of the recombination and the diffusion coefficient, respectively [29]. Fitting the characteristic time shown in Fig. 6.6 with Eq. 6.6, we can estimate the diffusion coefficient to be 6×10^{-4} cm^2/s. This value, however, is a factor of 2000 smaller than the 1 cm^2/s found in $(Pb,Sr)(Ti,Zr)O_3$ ferroelectric thin films [30], indicating that a more sophisticate model need to be considered.

The preliminary model described above ignores the effect of domain walls on carrier recombination. Electronic and optical properties at domain walls are different from than in the bulk. Among the relevant electronic phenomena at domain walls is that the oxygen vacancies accumulate near domain walls and could lower the energy band gap and lead to a local enhancement of carrier density [31]. A high carrier recombination rate is expected due to the high carrier density and high defect density at domain walls. The

domain walls, however, have a complex relationship to film thickness in the thickness regime we have probed. In addition to the change of relative volume fraction of ferroelastic domains, a tetragonal symmetry has been reported and no domains are resolved using piezoresponse force microscopy in $BiFeO_3$ thin film with a thickness of 12 nm [32]. The thickness dependence of the domain-wall-mediated carrier recombination is therefore difficult to be modeled quantitatively.

6.5 Photoinduced Peak Broadening

Femtosecond laser pulses induce structural changes of $BiFeO_3$ thin films beyond the average lattice expansion discussed in previous sections. These structural changes are apparent in the change of the distribution of diffracted intensity near the Bragg reflections. We will focus on the width change of the (002) Bragg reflection due to the intensity redistribution and discuss in detail a structural model considering the in-plane structural inhomogeneity.

Fig. 6.7 shows the FWHM of the $BiFeO_3$ (002) Bragg reflection, estimated using a Gaussian fit to the distribution of intensity, as a function of time for a series of transmitted fluence. The FWHMs before the optical pulses vary with film thickness. The laser-off FWHMs are 0.018 $Å^{-1}$ and 0.14 $Å^{-1}$ for films with thicknesses of 35 and 4 nm, respectively, as expected due to the smaller number of lattice planes in the 4-nm film. The key observation is that optical pulses induce a significant peak broadening with respect to the laser-off width at high fluence. For example, the maximum peak width increases to 0.025 $Å^{-1}$ for the 35-nm film at the highest transmitted fluence of 6.1 mJ/cm^2 used in our measurement.

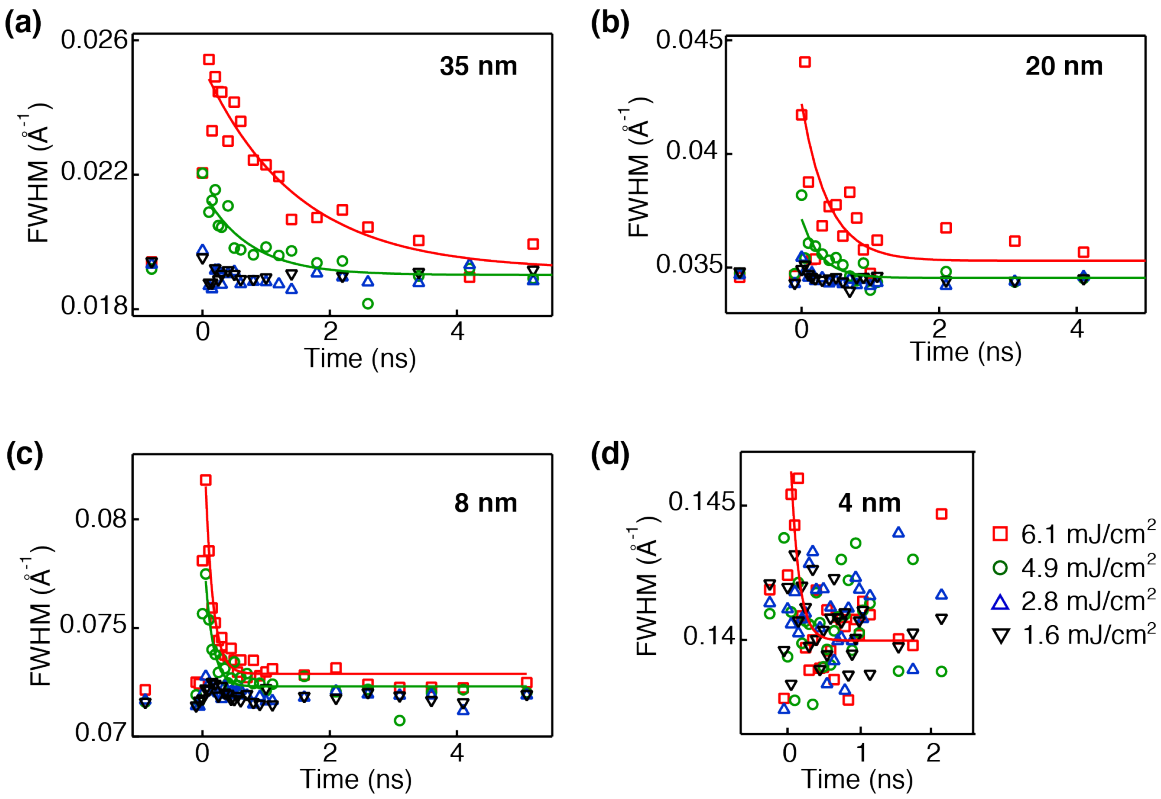

Figure 6.7 FWHM of the $BiFeO_3$ (002) Bragg peak as a function of time for films with different thicknesses. The symbols represent different magnitudes of transmitted fluence, ranging from 1.6 (downward triangles), 2.8 (upward triangles), 4.9 (circles) to 6.1 mJ/cm^2 (squares). The data points acquired at high transmitted fluence are fit with exponential decay function (lines).

Similar to photoinduced strain, the peak broadening relaxes as time elapses. We have extracted the characteristic time using an empirically exponential decay function, as shown with solid lines in Fig. 6.7 and as a function of film thickness in Fig. 6.6. The characteristic time of the relaxation of two different aspects of the structural effect induced by optical excitation share the same thickness dependence. For each film thickness, however, the characteristic time of the relaxation of peak broadening is a factor of two smaller than that for photoinduced strain.

The fluence dependence of the peak width is shown in Fig. 6.8 for $BiFeO_3$ thin films with thickness ranging from 4 to 35 nm. The diffraction patterns were acquired at

0.1 ns after the optical excitation where the maximum strain is observed. The 4-nm film has the largest laser-off width and lowest diffraction signal and no photoinduced change in peak width is resolved. For films thicker than 4 nm, the peak broadening is apparent at transmitted fluence higher than 4 mJ/cm^2, as pointed out in Fig. 6.7. This nonlinear fluence dependence of peak width explains the relatively small characteristic time of the relaxation of peak broadening in comparison with that of strain relaxation.

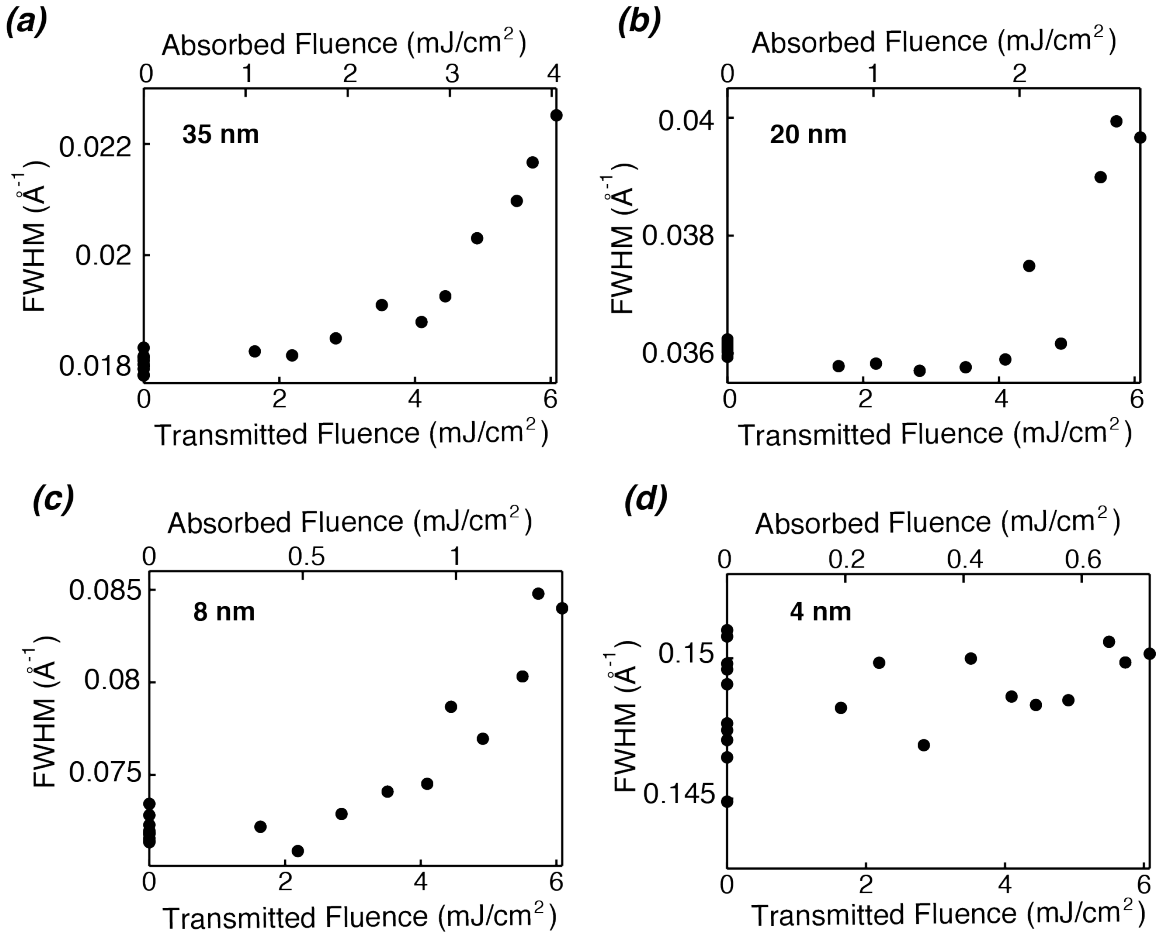

Figure 6.8 FWHM of the $BiFeO_3$ (002) Bragg peak as a function of the transmitted fluence ranging from 0 (before laser) to 6.1 mJ/cm^2 for 35- (a), 20- (b), 8- (c) and 4-nm (d) thin films. The absorbed fluence is shown as the top axis for reference.

To understand the origin of the nonlinear fluence dependence of peak width, we consider a model in which effects of extrinsic factors on peak width are described with an "extrinsic width". The effective peak width can then be expressed as in

$$w_{eff} = \sqrt{w_{in}^2 + w_{ex}^2}, \tag{6.7}$$

where w_{eff}, w_{in} and w_{ex} are the effective, intrinsic and extrinsic peak width, respectively. This quadratic relationship indicates that the extrinsic width is only important when its magnitude is comparable or larger than the intrinsic width, in our case the laser-off width, of the Bragg reflection. The key assumption of our model is that the extrinsic width associated with optical excitation is proportional to laser fluence, similar to photoinduced strain. Following the Eq. 6.7, a peak broadening can be expected at high fluence.

The experimentally observed peak broadening is related to the photoinduced local structural changes. The evolution of lattice structure can be captured with a kinematical x-ray simulation. We have built a 1D simulation super cell consisting of $BiFeO_3$ thin film and $SrTiO_3$ substrate. Bulk centrosymmetric $SrTiO_3$ lattice parameters are used for simulated $SrTiO_3$ unit cells. The in-plane $SrTiO_3$ lattice parameter is extended into $BiFeO_3$ unit cells as required by the film epitaxy. We have assumed a tetragonal symmetry for $BiFeO_3$ and ignored fractional atomic displacements resulting from the spontaneous polarization. The out-of-plane lattice parameter of $BiFeO_3$ was chosen to allow the simulation to produce Bragg reflections at angles that match the experimental values. Fig. 6.9(a) compares the diffraction patterns near the (002) Bragg peak for the 35-nm $BiFeO_3$ thin film acquired before the arrival of laser pulses with the kinematical x-ray simulation. The structural model considering a uniform strain, shown as the dotted line,

reproduces the reciprocal-space positions of the Bragg reflection and the thickness fringes, but underestimates the width of the Bragg reflection.

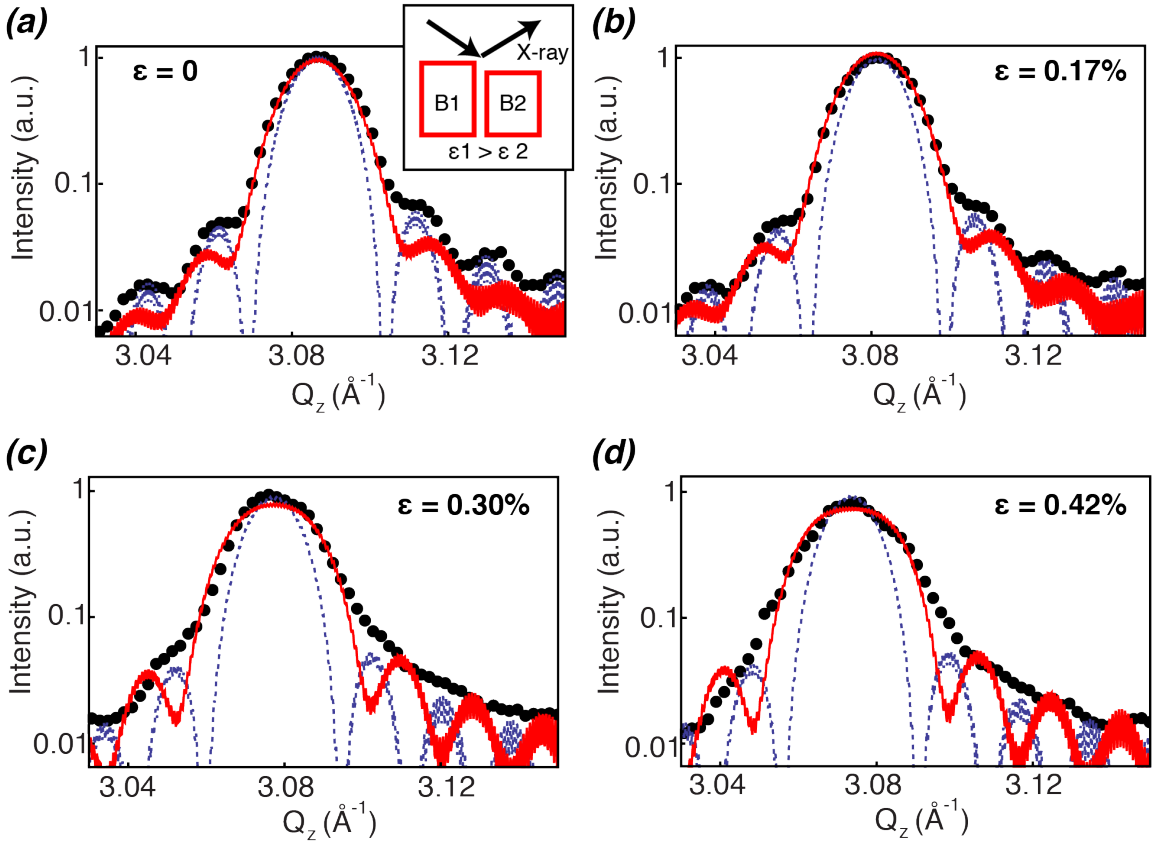

Figure 6.9 Comparison of simulated diffraction patterns with measured $BiFeO_3$ (002) Bragg peaks (circle) acquired before laser pulses with strain of 0% (a), and after laser pulses with strain of 0.17% (b), 0.30% (c) and 0.42% (d). Two structural models are considered: 1) a uniformly strained $BiFeO_3$ (dotted line) and 2) two blocks of $BiFeO_3$with different strain (solid line). The two-block model was schematically shown in the inset.

We have examined two factors that could broaden the Bragg reflection of the $BiFeO_3$ thin film: 1) an out-of-plane variation of the lattice constant and 2) an in-plane strain inhomogeneity. For the first case, we vary the out-of-plane lattice constant of the $BiFeO_3$ according an arbitrary strain gradient model. Origins of strain gradient along the film-thickness direction include a depth-dependent carrier concentration and non-uniform thermal expansion. In our simulation, the out-of-plane strain gradient affects the relative intensity among thickness fringes and the Bragg reflection, and induces an asymmetry in

the intensities of thickness fringes on opposite sides of the Bragg reflection. The reciprocal-space width of the central Bragg reflection, however, is not sensitive to out-of-plane strain gradient.

We have considered a series of arbitrary strain gradient models to reproduce a peak broadening of 25%, the experimental value we have observed. The required strain variation is 0.75% in the model considering a step distribution of strain, and as large as a few percent in other strain gradient models. This strain variation is unreasonably large because the maximum photoinduced strain is only 0.6% at the highest fluence. We therefore conclude that the out-of-plane strain gradient is not the primary source of the optically induced change in the width of the Bragg reflection.

The peak width is more sensitive to a variation of the strain along the in-plane direction. We simplified the strain inhomogeneity by computing the lattice sum of two $BiFeO_3$ blocks. Each block is assumed to have a uniform out-of-plane lattice constant and a thickness matching the experimental value. The key consideration here is that the lattice constant is different for each block. A peak broadening can be simulated as we increase the strain difference between the two blocks. For example, the two-block simulation is able to match the width of the laser-off Bragg reflection of the 35-nm $BiFeO_3$ thin film when a strain difference between the two blocks 0.29% is assumed, as shown in Fig. 6.9(a). This strain difference has taken into account artificial peak broadening due to finite measurement resolution, and therefore overestimates the experimental structural variation without the optical excitation.

We have extended the two-block model to interpret the diffraction patterns acquired after optical excitation. The measured Bragg peak width can be matched with

the two-block simulation by adjusting only one parameter, the strain difference. Examples are shown in Fig. 6.9(b)-(d) for times at which the photoinduced peak broadening is observed. Similar to the trend we observed in photoinduced peak broadening, the strain difference in the two-block model increases within the initial 0.1 ns, and relaxes to the zero-strain value over a few nanoseconds, as shown in Fig. 6.10(a). The maximum in-plane strain difference reaches 0.36% in the two-block model for 35-nm $BiFeO_3$ films. This value is smaller than the maximum photoinduced strain, and much smaller than the required strain variation in out-of-plane strain gradient model. The model considering in-plane strain inhomogeneity is therefore a more plausible structural model for photoinduced peak broadening.

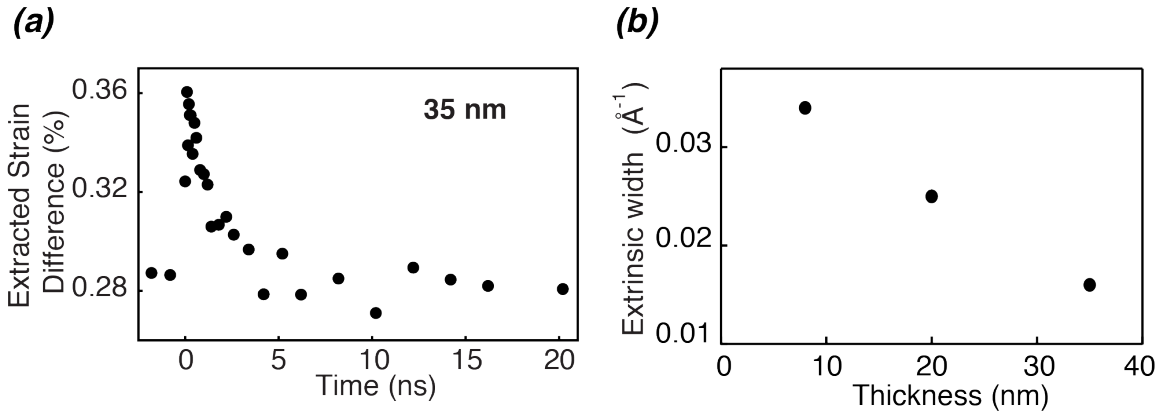

Figure 6.10 (a) The extracted difference of strain in the two-block model as a function of time. (b) The maximum extrinsic width as a function of film thickness.

We now focus on the thickness dependence of the strain inhomogeneity. The fractional increase of the peak width is smaller for thinner film, as evident and Fig. 6.8. However, due to the thickness-dependent intrinsic width, the extrinsic width causing the peak broadening is in fact increased by a factor of three while the thickness is reduced from 35 to 8 nm, as shown in Fig. 6.10(b). We have applied the two-block model to films thinner 35 nm. The maximum peak broadening in 8-nm film, for example, can be fitted

with an in-plane strain difference as large as 1%, indicating a much larger photoinduced strain inhomogeneity in 8-nm film than in 35-nm film. The large strain variation in thin films also suggests that a model more sophisticated than the two-block model is required to fully understand the photoinduced peak broadening.

The photoinduced in-plane strain inhomogeneity can arise from two factors. One is the non-uniform distribution of surface defects. The surface defect serves as a recombination site for carriers and defines the lateral distribution of carriers as the recombination process occurs. Due to the lack of defect characterization, a quantitative analysis of this effect is currently unavailable. The second factor is the optical anisotropy of ferroelastic domains that leads to an initial non-uniform distribution of carriers right after the optical excitation. The optical birefringence of $BiFeO_3$ [33], for example, can lead to a difference in reflectivity and result in 10% variation of transmitted photon energy for different domains in our setup. The difference in absorption, however, would require theoretical input for a quantitative estimation.

6.6 Conclusions

In conclusion, the photoinduced structural modification has been studied in detail in multiferroic $BiFeO_3$ epitaxial thin films. With the structural information provided by time-resolved x-ray diffraction, we have obtained insight to disentangle the relationship of photoinduced carriers, laser heating, depolarization field and lattice deformation at a sub-nanosecond timescale. The lattice expansion along surface normal arises mainly from a carrier-mediated piezoelectric effect, with a minor thermal component. The thickness-dependence of the strain relaxation suggests that the photoinduced carriers recombine at the surfaces and interfaces. We have also identified a strain inhomogeneity from the

detailed analysis of the intensity distribution of Bragg reflections. Understanding the origin of the ultrafast strain and strain inhomogeneity provides a new degree of freedom to optically tune the structure of electronic materials.

6.7 References

[1] D. Sando *et al.*, "*Crafting the Magnonic and Spintronic Response of $BiFeO_3$ Films by Epitaxial Strain,"* Nature Mater. **12**, 641 (2013).

[2] J. Zhang *et al.*, "*Microscopic Origin of the Giant Ferroelectric Polarization in Tetragonal-like $BiFeO_3$,"* Phys. Rev. Lett. **107**, 147602 (2011).

[3] D. Kan *et al.*, "*Universal Behavior and Electric-Field-Induced Structural Transition in Rare-Earth-Substituted $BiFeO_3$,"* Adv. Funct. Mater. **20**, 1108 (2010).

[4] Z. Chen *et al.*, "*Coexistence of Ferroelectric Triclinic Phases in Highly Strained $BiFeO_3$ Films,"* Phys. Rev. B **84**, 094116 (2011).

[5] P. Chen *et al.*, "*Nonlinearity in the High-electric-field Piezoelectricity of Epitaxial $BiFeO_3$ on $SrTiO_3$,"* Appl. Phys. Lett. **100**, 062906 (2012).

[6] T. Choi *et al.*, "*Switchable Ferroelectric Diode and Photovoltaic Effect in $BiFeO_3$,"* Science **324**, 63 (2009).

[7] H. T. Yi *et al.*, "*Mechanism of the Switchable Photovoltaic Effect in Ferroelectric $BiFeO_3$,"* Annu. Rev. Phys. Chem. **23**, 3403 (2011).

[8] B. Kundys, M. Viret, D. Colson, and D. O. Kundys, "*Light- Induced Size Changes in $BiFeO_3$ Crystals,"* Nature Mater. **9**, 803 (2010).

[9] S. K. Sundaram, and E. Mazur, "*Inducing and Probing Non-thermal Transitions in Semiconductors Using Femtosecond Laser Pulses,"* Nature Mater. **1**, 217 (2002).

[10] S. M. Young, F. Zheng, and A. M. Rappe, "*First-Principles Calculation of the Bulk Photovoltaic Effect in Bismuth Ferrite,"* Phys. Rev. Lett. **109**, 236601 (2012).

[11] J. Sipe, and A. Shkrebtii, "*Second-order Optical Response in Semiconductors,"* Phys. Rev. B **61**, 5337 (2000).

[12] D. Daranciang *et al.*, "*Ultrafast Photovoltaic Response in Ferroelectric Nanolayers,"* Phys. Rev. Lett. **108**, 087601 (2012).

[13] D. S. Rana *et al.*, "*Understanding the Nature of Ultrafast Polarization Dynamics of Ferroelectric Memory in the Multiferroic $BiFeO_3$,"* Adv. Mater. **21**, 2881 (2009).

[14] D. J. Kim *et al.*, "*Polarization Relaxation Induced by a Depolarization Field in Ultrathin Ferroelectric $BaTiO_3$ Capacitors,"* Phys. Rev. Lett. **95**, 237602 (2005).

[15] Y. Siegal, E. N. Glezer, L. Huang, and E. Mazur, "*Laser-Induced Phase Transitions in Semiconductors,"* Annu. Rev. Mater. Sci. **25**, 223 (1995).

[16] A. Othonos, "*Probing Ultrafast Carrier and Phonon Dynamics in Semiconductors,"* J. Appl. Phys. **83**, 1789 (1998).

[17] H. Lu *et al.*, "*Mechanical Writing of Ferroelectric Polarization,"* Science **336**, 59 (2012).

[18] J. F. Ihlefeld *et al.*, "*Optical Band Gap of $BiFeO_3$ Grown by Molecular-beam Epitaxy,"* Appl. Phys. Lett. **92**, 142908 (2008).

[19] E. M. Dufresne *et al.*, "*Time-Resolved Research at the Advanced Photon Source Beamline 7-ID,"* AIP Conf. Proc. **1234**, 181 (2010).

[20] S. R. Basu *et al.*, "*Photoconductivity in $BiFeO_3$ Thin Films,"* Appl. Phys. Lett. **92**, 091905 (2008).

[21] Y. M. Sheu *et al.*, "*Ultrafast Carrier Dynamics and Radiative Recombination in Multiferroic $BiFeO_3$,"* Appl. Phys. Lett. **100**, 242904 (2012).

[22] d. L. D, and P. Richet, "*High-temperature heat capacity and thermal expansion of $SrTiO_3$ and $SrZrO_3$ perovskites.,"* Physical review. B, Condensed matter **53**, 3013 (1996).

[23] J. D. Bucci, B. K. Robertson, and W. J. James, "*The precision determination of the lattice parameters and the coefficients of thermal expansion of $BiFeO_3$,"* J. Appl. Cryst **5**, 187 (1972).

[24] M. D. Biegalski, K. Doerr, D. H. Kim, and H. M. Christen, "*Applying Uniform Reversible Strain to Epitaxial Oxide Films,"* Appl. Phys. Lett. **96** (2010).

[25] H. Wen *et al.*, "*Electronic Origin of Ultrafast Photoinduced Strain in $BiFeO_3$,"* Phys. Rev. Lett. **110**, 037601 (2013).

[26] G. Catalan, and J. Scott, "*Physics and Applications of Bismuth Ferrite,"* Adv. Mater. **21**, 2463 (2009).

[27] J. Wang *et al.*, "*Epitaxial $BiFeO_3$ Multiferroic Thin Film Heterostructures,"* Science **299**, 1719 (2003).

[28] K. L. Luke, and L.-J. Cheng, "*Analysis of the Interaction of a Laser Pulse with a Silicon Wafer: Determination of Bulk Lifetime and Surface Recombination Velocity,"* J. Appl. Phys. **61**, 2282 (1987).

[29] A. B. Sproul, "*Dimensionless Solution of the Equation Describing the Effect of Surface Recombination on Carrier Decay in Semiconductors,"* J. Appl. Phys. **76**, 2851 (1994).

[30] Y. S. Yang *et al.*, "*Ferroelectricity and Electric Conduction Characteristics of Sr-Modified Lead Zirconate Titanate Thin Film Capacitors,"* Jpn. J. Appl. Phys. **36**, 749 (1997).

[31] W.-M. Lee *et al.*, "*Spatially Resolved Photodetection in Leaky Ferroelectric $BiFeO_3$,"* Adv. Mater. **24**, OP49 (2012).

[32] C. J. M. Daumont *et al.*, "*Tuning the Atomic and Domain Structure of Epitaxial Films of Multiferroic $BiFeO_3$,"* Phys. Rev. B **81**, 144115 (2010).

[33] S. Choi *et al.*, "*Optical Anisotropy and Charge-transfer Transition Energies in $BiFeO_3$ from 1.0 to 5.5 eV,"* Phys. Rev. B **83**, 100101 (2011).